Energie & Umwelt
Energy & Environment
271

Characterization of soil water content variability at the catchment scale using sensor network and stochastic modelling

Wei Qu

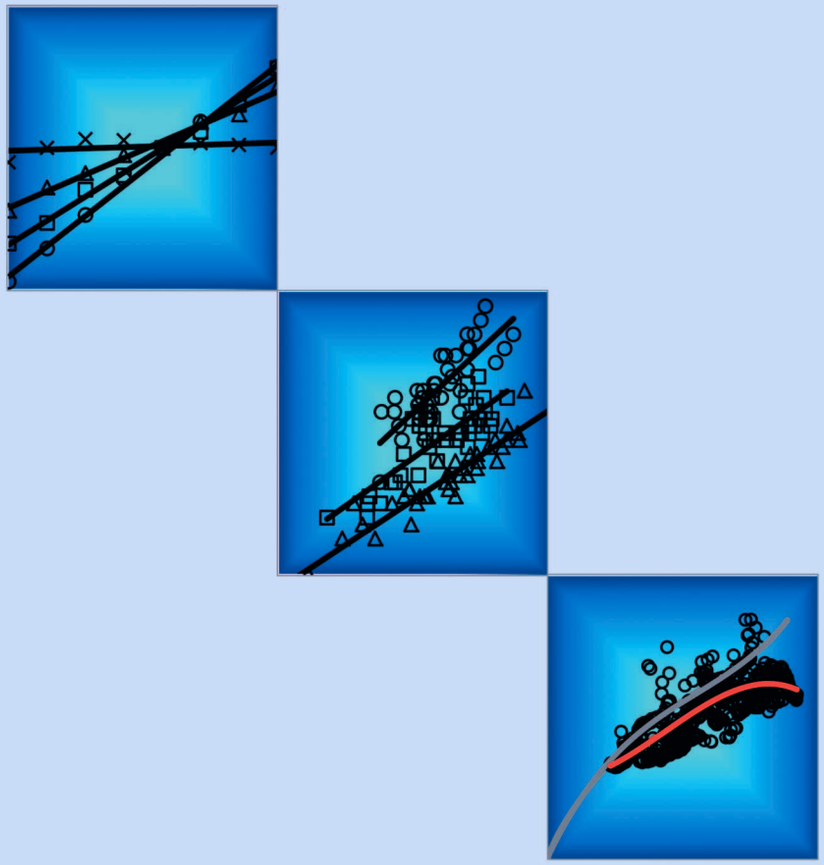

Energie & Umwelt / Energy & Environment
Band / Volume 271
ISBN 978-3-95806-067-8

JÜLICH FORSCHUNGSZENTRUM

Characterization of soil water content variability
Wei Qu

Member of the Helmholtz Association
JÜLICH FORSCHUNGSZENTRUM

Energie & Umwelt / Energy & Environment
Band / Volume 271
ISBN 978-3-95806-067-8

JÜLICH FORSCHUNGSZENTRUM

Schriften des Forschungszentrums Jülich
Reihe Energie & Umwelt / Energy & Environment Band / Volume 271

Forschungszentrum Jülich GmbH
Institute of Bio- and Geosciences
Agrosphere (IBG-3)

Characterization of soil water content variability at the catchment scale using sensor network and stochastic modelling

Wei Qu

Schriften des Forschungszentrums Jülich
Reihe Energie & Umwelt / Energy & Environment Band / Volume 271

ISSN 1866-1793 ISBN 978-3-95806-067-8

Bibliographic information published by the Deutsche Nationalbibliothek.
The Deutsche Nationalbibliothek lists this publication in the Deutsche
Nationalbibliografie; detailed bibliographic data are available in the
Internet at http://dnb.d-nb.de.

Publisher and Distributor: Forschungszentrum Jülich GmbH
Zentralbibliothek
52425 Jülich
Tel: +49 2461 61-5368
Fax: +49 2461 61-6103
Email: zb-publikation@fz-juelich.de
www.fz-juelich.de/zb

Cover Design: Grafische Medien, Forschungszentrum Jülich GmbH

Printer: Grafische Medien, Forschungszentrum Jülich GmbH

Schriften des Forschungszentrums Jülich
Reihe Energie & Umwelt / Energy & Environment, Band / Volume 271

D 5 (Diss., Bonn, Univ., 2015)

ISSN 1866-1793
ISBN 978-3-95806-067-8

The complete volume is freely available on the Internet on the Jülicher Open Access Server (JuSER)
at www.fz-juelich.de/zb/openaccess.

Abstract

Wireless sensor network technology has recently been used for high spatial and temporal resolution soil water content measurements to facilitate better understanding of hydrological processes in catchment scale. Its performance strongly depends on the quality of the sensors and the number of sensor nodes. In the first paper, the newly developed SPADE soil water content sensor was calibrated using a two-step laboratory-based procedure using dielectric reference liquids. The sensor accuracy was evaluated in terms of sensor-to-sensor variability and temperature effect. Using sensor-specific calibration significantly improved the estimation of apparent dielectric permittivity as compared to using a universal calibration function. The transferability of the temperature correction function from reference liquids to soils was successful and has been verified with undisturbed soil samples. A site-specific petrophysical model (complex refraction index model, CRIM) was used to convert apparent dielectric permittivity into soil water content using 15 soil samples from the Rollesbroich catchment, with RMSE values of 0.028, 0.025, and 0.022 cm^3cm^{-3} for 5, 20, and 50 cm, respectively.

In the second paper, a two-year time series in-situ soil water content from a wireless sensor network deployed in the Rollesbroich catchment was analyzed in terms of spatial variability using the mean relative difference (*MRD*) of the soil water content and saturation degree. The *MRDs* were also used to explore the potential controls of hydraulic properties on the spatial variability of soil water content at the catchment scale. To this end, hydraulic properties were estimated by inverse modeling using the physically-based soil water model Hydrus-1D and the global optimization algorithm SCE. Correlations between van Genuchten-Mualem (VGM) parameters were used as prior information for the parameter optimization. These hydraulic properties were derived from texture information and the Rosetta pedotransfer

function. Soil texture was determined from soil samples taken in the Rollesbroich catchment using standard laboratory procedures. The inverse Hydrus-1D model was able to reproduce the observed time series of soil water content at 41 locations and three depths with RMSE smaller than 0.08 cm^3cm^{-3} and R^2 larger than 0.75. The MRDs of soil water content and saturation degree were found to be positively correlated with the VGM parameters θ_s and n, and to be negatively correlated with the VGM parameters α and K_s.

In the third paper, a new closed-form expression of soil water variability was developed to explore the relationship between standard deviation (σ_θ) and mean of soil water content ($<\theta>$). The novel closed-form expression is based on the VGM model and uses stochastic theory of 1D unsaturated gravitational water flow in soils. A sensitivity study of the closed-form expression revealed that the n parameter has the strongest effect on the $\sigma_\theta(<\theta>)$ relationship, followed by the parameters K_s, θ_s, and α. The closed-form expression was used to estimate $\sigma_\theta(<\theta>)$ using information on percentages of sand, silt, and clay content, and bulk density from datasets of eight test sites with varying soil properties, vegetation, climate conditions and topographies. Six out of eight datasets showed good agreement between observed and predicted $\sigma_\theta(<\theta>)$ with R^2-values ranging between 0.55 and 0.84. Furthermore, The closed-form expression was successfully used to estimate the variability of hydraulic properties from observed $\sigma_\theta(<\theta>)$ data, with R^2-values ranging between 0.69 and 0.88. It is anticipated that an improved understanding of the $\sigma_\theta(<\theta>)$ pattern provides better insight for an improved upscaling of point-scale information to scales required for climate or hydrological modeling.

Kurzzusammenfassung

Funkbasierte Sensornetzwerke werden in jüngerer Zeit zur Messung des Bodenwassergehalts in hoher zeitlicher und räumlicher Auflösung verwendet, um zu einem verbesserten Verständnis von hydrologischen Prozessen auf der Einzugsgebietsskala zu gelangen. Die Effizienz von Sensornetzwerken hängt von der Qualität der verwendeten Sensoren und die Anzahl der Sensorknoten ab. In der ersten Veröffentlichung wurde der neu entwickelte SPADE Sensor mithilfe eines zweistufigen Verfahrens im Labor mittel dielektrischen Referenz-Flüssigkeiten kalibriert. Der Sensor wurde hinsichtlich der Sensor-zu-Sensor Variabilität und Temperatureffekte evaluiert. Es konnte gezeigt werden, dass eine Sensor-spezifische Kalibration erhöhte deutliche die Messgenauigkeit bei der Bestimmung der dielektrischen Permittivität im Vergleich zu einer universellen Kalibrationsfunktion. Die Übertragung der Temperaturfunktion konnte erfolgreich von den Referenzflüssigkeiten auf Bodenmaterial übertragen werden. Das petrophysikalische Modell CRIM (complex refraction index model) wurde erfolgreich eingesetzt, um mit dem SPADE Sensor gemessene dielektrischen Permittivität in volumetrischen Wassergehalt umzurechnen (15 Bodenproben aus dem Rollesbroich Einzugsgebiet mit RMSE von 0.028, 0.025 und 0.022 cm^3cm^{-3} für Bodentiefen von 5, 20 und 50cm.

In der zweiten Veröffentlichung, wurde Bodenfeuchte-Zeitreihen gemessen mit einem Sensornetzwerk installiert in dem Rollesbroich Einzugsgebiet hinsichtlich der zeitlichen Stabilität untersucht. Hierzu wurden *MRDs* (mean relative difference) der Wassergehälter und der Sättigungsgrade ermittelt. Die *MRDs* wurden weiterhin dazu verwendet, die Einflüsse von hydraulischen Eigenschaften auf die räumliche Variabilität der Bodenfeuchte auf der Einzugsgebietsskala zu untersuchen. Hierzu wurde hydraulische Eigenschaften

mittels inverser Modellierung der Bodenfeuchtezeitreihen unter Verwendung des physikalisch basierten Bodenwassermodell Hydrus-1D und dem globalen Optimierungs-Algorithmus SCE ermittelt. Die Korrelationen zwischen den Parametern des van Genuchten-Mualem (VGM) Modells wurden als Vorabinformation für die Parameterschätzung verwendet. Diese hydraulischen Eigenschaften wurden zuvor aus Texturdaten mittels der Pedotranferfunktion Rosetta berechnet. Die Texturdaten wurden von Bodenproben aus dem Rollesbroich Einzugsgebiet mit standardisierten Labormethoden ermittelt. Das inverse Hydrus-1D Modell war in der Lage, die gemessenen Bodenfeuchtezeitreihen von 41 Messstellen und drei Messtiefen mit einem RMSE kleiner als 0.08 cm^3cm^{-3} und einem R^2 größer als 0.75 zu simulieren. Die *MRDs* der Bodenfeuchte und des Sättigungsgrads mit den VGM Parametern korreliert (positive Korrelation mit θ_s und n; negative Korrelation mit α and K_s).

In der dritten Veröffentlichung wurde ein neues geschlossenes Gleichungssystem (closed-form expression of soil water variability) zur Untersuchung der Beziehung zwischen der Standardabweichung (σ_θ) und mittlerer Bodenfeuchte ($<\theta>$) entwickelt. Das geschlossene Gleichungssystem basiert auf das VGM Modell und der stochastischen Theorie of 1D ungesättigten gravitativen Wasserfluss im Boden. Eine Sensitivitätsanalyse des geschlossenen Gleichungssystems zeigte, dass der n Parameter den größten Einfluss auf die $\sigma_\theta(<\theta>)$ Beziehung hat, gefolgt von K_s, θ_s, and α. Das geschlossene Gleichungssystem wurde dann dazu benutzt, um die $\sigma_\theta(<\theta>)$ Beziehung aus Textur- und Bodendichteinformationen von acht Testgebieten mit unterschiedlichen Bodeneigenschaften, Vegetationsbedeckungen, klimatischen Bedingungen und topographischen Verhältnissen abzuschätzen. Sechs der acht Datensätze zeigten eine sehr gute Übereinstimmung mit beobachteter und vorhergesagter $\sigma_\theta(<\theta>)$ (R^2 zwischen 0.55 und 0.84). Weiterhin wurde das geschlossene Gleichungssystem

erfolgreich dazu benutzt, die Variabilität von hydraulischen Bodeneigenschaften aus beobachten $\sigma_\theta(<\theta>)$ Daten zu schätzen (R^2 zwischen 0.69 und 0.88). Es ist zu erwarten, dass dieses verbesserte Verständnis über die $\sigma_\theta(<\theta>)$ Beziehung das Heraufskalieren von Punktinformation auf Skalen, die für die Modellierung von hydrologischen Systemen und Klima benötigt werden, unterstützen wird.

Contents

List of Abbreviations

SRP	sensor response permittivity
CRIM	Complex refractive index model
TDT	time domain transmission
TDR	time domain reflectometry
EM	electromagnetic
std	standard deviation
CV	coefficient of variation
RMSE	root mean square error
ANOVA	Analysis of variance procedure
Eq.	Equation
v_p	electromagnetic waves
c	speed of light in vacuum
μ_r	magnetic permeability
ε_r	dielectric permittivity
T_{ε_r}	pulse travel time along the transmission line
t_{pd}	propagation delay of the ECL gate
t_{rf}	influence of the pulse rise and fall time
f_{osc}	oscillation frequency
i-C_3E_1	2-Isopropoxyethanol
K_a	apparent dielectric permittivity
α_i	SRP fitting parameter
β_i	SRP fitting parameter
γ_i	SRP fitting parameter
ε_{ref}	reference static permittivity
$\Delta K_{a,T}$	effect of temperature on the sensor response
η	porosity
β	shape factor
K_{solid}	permittivity of solids in soil
K_{air}	permittivity of air
K_{water}	permittivity of water
T	temperature

R^2	correlation coefficient
RD	relative difference
MRD	mean relative difference
SDRD	standard deviation of relative difference
VGM	van Genuchten-Mualem
SDMRD	Standard deviation of mean relative difference
S_e	saturation degree
θ	soil water content
θ_r	residual soil water content
θ_s	saturated soil water content
α	shape factor related to air entry value
n	shape factor related to pore size distribution
K_s	saturated hydraulic conduvtivity
ET_0	potential evapotranspiration
E	evaporation
T	transpiration
LAI	leaf area index
D	Mahalanobis distance
σ_θ	standard deviation of soil water content
$\sigma_{\theta_e}^2$	variance of soil water content
$<\theta>$	mean of soil water content
$<\theta_s>$	mean of saturated soil water content
$<\ln(K_s)>$	mean of logarithm saturated hydraulic conductivity
$<\alpha>$	mean of air entry parameter
$<n>$	mean of pore size parameter
$\sigma(\theta_s)$	standard deviation of saturation degree
$\sigma(\ln(K_s))$	standard deviation of logarithm saturated hydraulic conductivity
$\sigma(\alpha)$	standard deviation of air entry parameter
$\sigma(n)$	standard deviation of pore size distribution parameter
$\rho_{\ln(Ks)}$	correlation scale of logarithm saturated hydraulic conductivity
ρ_α	correlation scale of air entry parameter
ρ_n	correlation scale of pore size distribution

List of Tables

List of Figures

1 General Introduction

Soil water content is fundamental importance to many hydrological, biological and biogeochemical processes (Bittelli, 2011; Robinson et al., 2008). It is the key state variable in the soil, vegetation and atmosphere continuum as it directly influences the exchange of water and energy between land surface and atmosphere through evaporation and plant transpiration. Regional soil water content patterns are influencing the generation of weather and precipitation patterns (Teuling and Troch, 2005). Moreover, knowledge about soil water content dynamics is valuable to a wide range of application, e.g. for government agencies and private companies concerned with weather and climate (Seneviratne et al., 2010), runoff and flood control (Castillo et al., 2003; Smith et al., 2002; Wang and Zhu, 2003), soil erosion and slope failure (Wang and Zhu, 2003), reservoir management (Eltahir, 1998), precision agriculture (Sudduth et al., 2001; Zhang et al., 2002), geotechnical engineering (Fredlund, 2000), and water provision (Betts et al., 1996).

There existing different measurement techniques to determine soil water content across a broad range of scale, e.g. from point scale to regional scale (Robinson et al., 2008; Vereecken et al., 2014; Western et al., 2002). The most commonly used techniques to measure soil water content at point scale were using gravimetric sampling, time domain reflectometry (TDR), capacitance sensors, and neutron probes (Qu et al., 2013; Robinson et al., 1999; Robinson et al., 2003; Rosenbaum et al., 2011). However, these ground based method are too labor intensive to remain feasible with increasing space/time sampling frequency. Remote sensing enables the measurement soil water content at large scales with a single instrument on a mobile platform and eliminates errors introduced by sensor-to-sensor variability (Montzka et al., 2011; Montzka et al., 2013). However, remote sensing technology is only sensitive to the

upper few centimeters of soil because the emitting depths penetration depth is approximately 5 cm. In addition, it is more susceptible to the effects of vegetation and surface roughness (Robinson et al., 2008; Vereecken et al., 2008). Consequently, with the growing interest in watershed observations, we consider to measure spatial temporal soil water content and to describe soil water content patterns in catchment scale. Wireless sensor network technology is an ideally technique provides continuous measurements of soil water content with high spatial and temporal resolution at an intermediate scale (Bogena et al., 2010; Hübner et al., 2009; Rosenbaum et al., 2012).

Terrestrial Environmental Observation (TERENO) is the platform that establishes a structured network of hierarchically organized multi-compartments measurement and observation platforms that use state of the art observation and measurement technologies (Bogena et al., 2012; TERENO, 2012; Zacharias et al., 2011). The different spatial and temporal scales observation networks of TERENO aims at to detect and quantify both short and long term effects and impacts on the terrestrial systems. The intensive observation wireless sensor network allows us the real-time soil water content and temperature monitoring with a high spatial and temporal resolution for the observing hydrological processes in the catchment.

The wireless sensor network technology uses the low-cost ZigBee radio network for communication and a hybrid topology with a mixture of underground end devices each wired to several soil sensors and aboveground router devices (Bogena et al., 2010; Bogena et al., 2009; Bogena et al., 2007). It consists hundreds of soil water content sensors that transmit information to a main server with wireless communication technology (Bogena et al., 2010;

Hübner et al., 2009). The performance of a wireless soil water content sensor network strongly depends on the quality of the sensors in terms of measurement accuracy, the sensitivity of the sensor output to changes in temperature and the sensor-to-sensor variability of the empirical relationship between sensor output and soil water content (Robinson et al., 2008; Robinson et al., 2003). In order to maximize the number of sensor nodes, the soil water content sensors should be as inexpensive as possible without compromising sensor accuracy too strongly.

There are different kinds of electromagnetic probes available for the wireless sensor network (Hübner et al., 2009; Kelleners et al., 2005; Kizito et al., 2008; Qu et al., 2013; Robinson et al., 2005b; Ryu and Famiglietti, 2005). Time domain reflectometry (TDR) probe is one of the most well know soil water content sensors and has the advantage of being in-situ, real-time, and more accurate. In addition, TDR allows connecting with a multiplexer and simultaneously collect the soil water content in a number of locations (Blonquist et al., 2005b; Noborio, 2001; Robinson et al., 2003). Despite all of its advantages, the cost of TDR and the level of ability required by the operator often place it beyond the means of growth. Capacitance and impedance probes have tended to fill the lower price market. These instruments tend to be limited to operating frequencies less than 150 MHz which is undesirable if the soil has dielectric dispersion in this frequency range (Kelleners et al., 2005; Kizito et al., 2008; Robinson et al., 2005b; Ryu and Famiglietti, 2005). Most of these instruments do not permit the measurement of bulk soil electrical conductivity, which can be useful for management purposes. However, many of the capacitance sensors are sensitive to interference from bulk soil electrical conductivity and while many will continue to operate, but the prediction of water content can be very poor. The design concept of a stand-alone

sensor should be of low cost, small size, high accuracy, and precision in the determination of permittivity that covers a representative sampling volume. Therefore, the new developed SPADE TDT sensors are currently considered to be one of the most appropriate probes for wireless soil water content sensor network (Hübner et al., 2009; Qu et al., 2013). The SPADE probe is based on a ring oscillator and the frequency of the oscillator is a function of the dielectric permittivity of the surrounding medium, which is strongly depended on the water content of the soil because of the high permittivity of water, i.e. 78.5 at 25°C (Weast, 1986), as compared to mineral soil solids range from 2 to 9 (Robinson and Friedman, 2003), and air is 1.

There are two main ways to calibrate the electromagnetic sensor, i.e. the directly calibration or the two-step calibration procedure. Considering the number of sensors used for the wireless sensor network, directly calibration is time consuming and labor insensitive. The two-step calibration procedure in the laboratory experiments is more welcomed. In the first step, the sensor reading is related to permittivity using the standard sensor calibration methodology proposed by Jones et al. (2005). The electromagnetic measurement is sensitive to dielectric relaxation, electrical conductivity, and temperature (Pepin et al., 1995; Topp et al., 2000). To avoid unwanted noise due to these secondary factors as well as contact problems between medium and sensor in the calibration. The non-relaxing and non-conducting liquids of 2-Isopropoxyethanol (i-C_3E_1) and 1,4-Dioxane (D) were used for this calibration suggested by Jones et al. (Jones et al., 2005) and Bogena et al. (2007). Several studies have carried out to test the plausibility of this methodology. Such as Bogena et al. (2007) have calibrated the EC-5 sensor with the reference liquids of Dioxane/water and 2-isopropoxyethanol/water mixtures with a permittivity range from 2.2 to 41.3. Their results

showed that the standard method of the characterization of electromagnetic sensor is reproducible. The same method was successfully applied to calibrate the ECH_2O, TE, and 5TE sensors by Rosenbaum et al. (2010). In addition, Qu et al. (2013) also calibrated the newly developed SPADE TDT sensors using the standard reference liquids. In the second step, a site-specific calibration can be carried out to relate the permittivity with soil water content by using empirical models or semi-theoretical models, e.g. Topp model (Topp et al., 1980), complex refraction index model (Birchak et al., 1974), and the two point-mixing model (Sakaki et al., 2008; Yu et al., 1997). An advantage of the two-step calibration method is that, assuming that the apparent permittivity and soil water content relationship in the second step is valid for the soils of interest, recalibration for all the sensors is not required when the sensors are installed in deferent soils. Otherwise, a recalibration for all the sensors would be needed in the direct approach.

The Rollesbroich grassland catchment has been equipped with a wireless soil water content sensor network (SoilNet, 2012). The SPADE TDT soil water content probes (sceme.de GmbH i.G., Horn-Bad Meinberg, Germany) were calibrated using the two-step calibration procedure and were installed at different soil depth along a vertical profile. In order to increase the measurement volume and enable the examination of inconsistencies, two sensors were installed in each depth. The quality of long time series soil water content data observed by wireless sensor network can be checked with the method proposed by Dorigo et al. (2013). First to flag the extremely spikes beyond the physical plausibility range of soil water content. Then, they checked the suspicious observations based on the continuity of the time series data sequence. The unexpected soil water content caused by the failure of the measurement was flagged. Furthermore, they characterized each time step of soil water content with respect to a

local neighborhood of prior and subsequent observations. The soil water content was flagged if it exceeded the criterial values. Many other statistical filtering methods are available, such as the Savitzky-Golay filter, Relational Sequence filter, non-linear FIR filters (Pearson, 2011).

The high spatial and temporal soil water content data observed by wireless sensor network can be used to characterize and analyze spatial temporal variability of soil water content patterns. Different quantitative methods are available to analyze spatial temporal dynamics and patterns using statistical approaches, e.g. temporal stability analysis (Vachaud et al., 1985; Vanderlinden et al., 2012) or the empirical orthogonal functions (Korres et al., 2010; Yoo and Kim, 2004). The empirical orthogonal function (EOF) analysis or principal component analysis (PCA) is a widely applied statistical method for analyzing large multidimensional datasets and for searching the dominant factors for the spatial temporal structure of soil water content, and how the dominancy is changed from one factor to another with time (Perry and Niemann, 2007; Yoo and Kim, 2004). EOF analysis partitions the observed variation into a series of time-invariant spatial patterns (in terms of EOFs) that can be multiplied by temporal varying (but spatially constant) coefficients and summed to reconstruct observed soil water content patterns. In addition, EOFs can be mapped and these maps can be compared with maps of various soil, landscape, and land use properties in search of similarities patterns in them(Jawson and Niemann, 2007; Korres et al., 2010; Perry and Niemann, 2007).

Yet another most widely used method is the temporal stability analysis (Vachaud et al., 1985; Vanderlinden et al., 2012). Temporal stability has also been termed as rank stability temporal

persistence, or time-stable in describing the persistence of spatial patterns and characteristic behavior of soil water content (Pachepsky et al., 2005). Vachaud et al. (1985) first proposed the concept of temporal stability to determine representative locations within a field, thus improving sampling efficiency while maintaining accuracy to represent the mean of soil water content in the catchment. In addition, the temporal stability can be used to characterize the spatial pattern of soil water content with the mean relative difference (*MRD*). And studies have shown that the spatial pattern of soil water content does not change with time in a certain probability, this phenomenon was named as time stability, which was expressed as the standard deviation of the relative difference (*SDRD*) in the temporal stability analysis.

Although a large number of publications on spatial variability of soil water content already exist (Jacobs et al., 2004; Martinez et al., 2014; Martinez et al., 2013; Mohanty and Skaggs, 2001; Wang, 2014), the controlling factors are still not well understood. Previous studies have shown that multiple factors, such as climate (Martinez et al., 2014), topography (Biswas and Si, 2011; Hu et al., 2010a), soil properties (Martinez et al., 2013; Williams et al., 2009), and vegetation (Gomez-Plaza et al., 2001; Mohanty and Skaggs, 2001) affect the *MRD* of soil water content, and that these factors tend to interact (Baroni et al., 2013; Vanderlinden et al., 2012). For instance, Jacobs et al. found that (2004) the sampling locations with relatively high sand content consistently have a low *MRD* of soil water content while those locations with relatively high clay content consistently have a high *MRD* of soil water content. Furthermore, with the numerical simulation study of the Hydrus 1D modeling, Martinez et al. (2013) quantified the impact of soil saturated hydraulic conductivity (K_s) on *MRD* of soil water content with the consideration of root water uptake, they found a negative linear relationship between the *MRD* of soil water content and logarithm of K_s. Continues to this

study, they also studied the impact of K_s on *MRD* of soil water content under different climate conditions (Martinez et al., 2014). The correlation between the *MRD* of soil water content and logarithm of K_s was similar with the previous study. For both studies, only a log-normal transformed K_s was considered for the spatial variability of hydraulic properties. However, the more complex covariance structures between K_s and other VGM parameters are ignored. The more recently simulation study of Wang (2014) has analyzed the relationship between the VGM parameters and the *MRD* of soil water content by considering the covariance structure between the VGM parameters in a semi-arid climate. He found that the residual soil water content (θ_r) was the primary control of *MRD* of soil water content; and they are strongly positively correlated with each other. Moreover, by fixing θ_r, a strong negative relationship was found between the VGM parameter of n and the *MRD* of soil water content. Moreover, Mohanty and Skaggs (2001) reported that the *MRD* of soil water content are negative correlated with the slope, the soil sampled located in the smaller slope always have a larger *MRD* of soil water content, however, the steep locations always have a smaller *MRD* of soil water content. However, all these studies are either only based on the short term campaign or based on synthetic modeling studies that difficult to transferred them into the field conditions.

In order to evaluate correlations between soil hydraulic properties and *MRD* of soil water content with the continuous time series observations from the wireless sensor network, hydraulic parameters need to be determined at each location where soil water content is measured using either direct or indirect methods. There are different methods to evaluate the hydraulic properties (Angulo-Jaramillo et al., 2000; Mermoud and Xu, 2006; Wessolek et al., 1994). One common way is directly fitting the water retention curve and hydraulic

conductivity to experimental data obtained from soil cores in the laboratory (Mermoud and Xu, 2006; Ratliff et al., 1983). However, the use of such direct method in involves considerable uncertainty caused in part by the absence of collocation between measurements of soil hydraulic properties and soil water content. Alternatively, soil hydraulic properties can be estimated indirectly from basic soil information such as the sand, silt and clay fractions, bulk density and/or organic matter content using pedotransfer functions (Pachepsky et al., 2006; Schaap and Leij, 1998; Schaap et al., 2001; Vereecken et al., 2010; Wosten et al., 2001). Pedotransfer functions are often used to generate soil hydraulic properties in situations where measurements are too expensive, too cumbersome, or too difficult to carry out. However, there are many different types of pedotransfer functions in terms of input data, the predicted properties, mathematical structure and accuracy and it is often not clear which pedotransfer function is best selected for a particular case. To overcome these problems, a rapid, reliable, and cost-effective approach of inverse modeling can be used to estimate soil hydraulic parameters indirectly in case information on in-situ state variables (e.g. soil water content, matrix potential) is available (Duan et al., 1992; Mertens et al., 2004; Vandam et al., 1994; Vrugt et al., 2004; Vrugt et al., 2008). This procedure has the advantage that the results are based on field observations under natural flow conditions. In addition, the parameter estimated from inverse modeling accommodates more flexible experimental conditions than typically utilized in laboratory experiments and facilitates estimating values of the hydraulic properties that pertain to the scale of interest (Vrugt et al., 2008).

It is important to explore the potential correlations between soil hydraulic properties and its relation with *MRD* of soil water content with long time series observations from the field. The knowledge of such correlation can provide information for the design of wireless sensor

networks, e.g. using the pedotransfer function (Schaap et al., 2001; Vereecken et al., 2010; Wosten et al., 2001) to estimate the hydraulic properties with the basic soil information which can be easily get from the soil map, and find the representative locations using the correlation between hydraulic properties and *MRD* of soil water content. Furthermore, it will improve the performance of hydrologic models by considering the variability of soil hydraulic properties from the *MRD* of soil water content in the catchment.

In order to further explore the limitations and potentials between the *MRD* of soil water content and soil hydraulic properties, a wide range of soil textural classes and climate conditions should be considered. Furthermore, the *MRD* of soil water content is known to be determined by a number of physiographic factors that affect the vertical and lateral redistribution of soil water. Although factors that influence vertical redistribution are understood relatively well, the factors that cause lateral redistribution are not yet well quantified. In future studies, the effect of topography on the *MRD* of soil water content and saturation degree should be considered in addition to the heterogeneity of soil hydraulic properties.

Another important characteristic of the variability of soil water content expressed in terms of standard deviation of soil water content plays an essential role on the magnitude of land-surface energy fluxes (Bonan et al., 1993; Hu and Islam, 1998; Ronda et al., 2002) and hydrologic fluxes such as runoff (Arora, 2001; Gedney and Cox, 2003). By combining the relationship between the standard deviation (σ_θ) and mean of soil water content ($<\theta>$) with the integrating knowledge of remote sensing and hydrology models may finally lead to a better understanding and a more fundamental interpretation of the role of soil water content

variability in land surface processes across (Crow et al., 2005; Zijl, 1999). In addition, it is useful for improve the prediction accuracy of large-scale hydrologic, weather, and climate models (Teuling et al., 2007). Furthermore, it may also be useful for validation of large-scale remote sensing soil water content measurements (Famiglietti et al., 2008).

Several field studies have been carried out to identify the relationship between standard deviation and mean of soil water content; however the results are not consistency. For example, several investigators found positive relationship between the standard deviation and mean of soil water content (Famiglietti et al., 1998; Oldak et al., 2002; Takagi and Lin, 2011). In contrast to their studies, Famiglieittie et al. (1999), Hupet and Vanclooster (2002) and Western et al. (2004) observed negative correlations between the standard deviation and mean of soil water content. A more common saying is that there was a convex curve between the standard deviation and mean of soil water content, the standard peaked at the middle range of soil water content, and decreased in both wet and dry hand (Choi and Jacobs, 2007; Garcia-Estringana et al., 2013; Rosenbaum et al., 2012).

The $\sigma_\theta(<\theta>)$ relationship can be non-unique, with many control factors including spatial and temporal heterogeneous fluxes and the sink terms such as infiltration, evaporation, transpiration, and surface runoff (Albertson and Montaldo, 2003; Teuling and Troch, 2005). These terms depend on soil properties, vegetation, meteorological factors, groundwater, and topography (Famiglietti et al., 1998). It was reported that soil properties including soil texture and structure have (Hu and Islam, 1998; Vereecken et al., 2007) strongly affect the soil water variability by direct influence on the soil hydraulic. Under wet condition, the heterogeneity of soil porosity can lead a great impact on water movement, and thus soil water content

variability. When soil start to drain, the increasing variability of hydraulic properties lead to an increasing standard deviation of soil water content. After the soil water content decreases to a threshold soil water state (between wilting point and field capacity) the dominant flux switches from drainage to evapotranspiration, the impact of vegetation on the variability soil water content is considered to be major at this moment, and therefore the standard deviation of soil water content becomes less affected by the hydraulic properties. With further drying, the standard deviation of soil water content diminishes by evapotranspiration, which is only related to residual soil water content.

The existing methods to investigate the control of the $\sigma_\theta(<\theta>)$ pattern include numerical simulation of the soil water balance (Montaldo and Albertson, 2003; Roth, 1995) and first order stochastic analysis of unsaturated flow (Vereecken et al., 2007; Zhang et al., 1998). Albertson and Montaldo (2003) presented a theoretical framework to evaluate the variance of soil water content as a function of the variances of infiltration, drainage, evapotranspiration, and horizontal redistribution and their covariances. They found that according to the sign of the correlation between the flux and the state of soil water condition, covariances between soil water and land surface fluxes act to generate or destroy the variance of soil water content through time. Zhang et al. (1998) provided an analytic stochastic method to obtain the variance of effective soil water content for 1D vertical flow using the Brooks-Corey model and Gardner-Russo model. Based on the work of Zhang et al. (1998), Vereecken et al. (2007) predicted the $\sigma_\theta(<\theta>)$ relationship with the stochastic results of the unsaturated Brooks-Corey modal, and they found that the hydraulic parameters of Brooks-Corey and their spatial variances determine to a large extent of the $\sigma_\theta(<\theta>)$ shape, especially the parameter described as pore size distribution controls the maximum value of the standard deviation of soil water

content. These stochastic studies are based on the Brooks-Corey model due to its mathematical tractability. However, it is generally accepted that the more complex van Genuchten-Mualem (VGM) model may perform better in expressing experimental data than Brooks-Corey model.

The stochastic approach of Zhang et al. (1998) to describe 1D unsaturated gravitational flow in a heterogeneous flow domain was used to derive a closed-form expression that describes $\sigma_\theta(<\theta>)$ using the VGM model. The encouraging exploration presented in this thesis can be served for future large scale model applications. Because the basic assumptions underlying the stochastic theory are rarely in the real field conditions, the closed-form expression should be tested across a wide range of climatic conditions and soil texture classed. Future model developments are intended to consider meteorological forcing variability, and the topographic effects on the spatial distribution of soil water content.

The present thesis is structured into three main parts. The objective of first part is the calibration of the newly developed SPADE soil water content sensor for wireless sensor network applications. To this end, a series of laboratory experiments were performed in order to explore sensor-to-sensor variability and temperature effects on dielectric permittivity measurements with both standard reference liquid and soil samples. In addition, a site specific calibration between the permittivity and soil water content was derived with the undisturbed soil samples took from the Rollesbroich catchment. The objective of the second part is to investigate the correlation between hydraulic properties and spatial variability of soil water content in catchment scale using a two-year time series soil water content data observed with wireless sensor network and an inverse modeling approach. Finally, the third

part derived a closed-form expression to describe the variability of soil water content using stochastic analysis of 1D unsaturated gravitational flow based on the van Genuchten-Mualem (VGM) model. A sensitivity analysis was applied to check how the hydraulic properties affect the relationship between the standard deviation and mean of soil water content. Furthermore, the closed-form expression was verified using eight datasets span a wide range of soil texture classes and climate conditions. The results of this thesis are presented in three chapters which correspond to published or submitted publications in international peer-reviewed journals.

Chapter 2 Calibration of a novel low-cost soil water content sensor based on a ring oscillator.

Chapter 3 Effects of soil hydraulic properties on the spatial variability of soil water content: evidence from sensor network data and inverse modeling.

Chapter 4 Predicting sub-grid variability of soil water content from basic soil information.

These chapters feature their own objectives, introductions, methods and materials since the different issues highlight aspects of the overall research question in a different manner. The results are concluded and a brief outlook for further research is given in Chapter 5.

2 Calibration of a novel low-cost soil water content sensor based on a ring oscillator

This chapter has been published as: W. Qu, H. R. Bogena, J. A. Huisman, H. Vereecken. Calibration of a novel low-cost time domain transmission soil water content sensor. Vadose Zone Journal, 2013, 12(2). doi:10.2136/vzj2012.0139.

2.1 Objectives

In this chapter, we focus on the calibration of sensor response to soil water content using a two-step calibration procedure. First step is to relate sensor response to apparent dielectric permittivity by using an empirical sensor response permittivity (SRP) model. The sensor accuracy is evaluated by the sensor-to-sensor variability and temperature effect with the reference standard liquids. In the second step, a site specific calibration between the apparent dielectric permittivity and soil water content using the petrophysical model of complex refraction index model (CRIM) is derived for Rollesbroich catchment (See Appendix A).

2.2 Introduction

Soil water content is a key variable in the soil, vegetation and atmosphere continuum. It plays an important role in weather and climate predictions because it directly influences the exchange of water and energy at soil surface. In addition, it also impacts crop growth and the fate of agricultural chemicals applied to soils. Multi-scale measurements of soil water content are required to improve understanding and modeling of soil hydrology. There is a wide range of methods for soil water content estimation (Robinson et al., 2008). The gravimetric method is the standard method and is typically used as a reference. However, the effort associated with soil sampling prohibits monitoring with a high temporal and spatial resolution. Electromagnetic soil water content sensors that measure the dielectric permittivity of the soil are now widely accepted for soil water content determination because these sensors allow continuous, fast, stable and non-destructive sensing of the spatial temporal dynamics of soil water content at the field scale (Robinson et al., 2003; Vereecken et al., 2008).

Wireless sensor network technology has recently been used for catchment scale measurements of soil water content with high spatial and temporal resolution to facilitate better understanding of hydrological processes (Bogena et al., 2010; Rosenbaum et al., 2012). Such large scale but highly resolved soil water content information is important for the calibration and validation of remote sensing data (Montzka et al., 2011; Montzka et al., 2013). In the framework of the TERENO project (TERENO, 2012; Zacharias et al., 2011), the test site Rollesbroich in the Rur/Lower Rhine Valley Observatory has been equipped with a wireless soil water content sensor network. The performance of a wireless soil water content sensor network depends strongly on the quality of the sensors in terms of measurement accuracy, the sensitivity of the sensor output to changes in temperature and the sensor-to-sensor variability of the empirical relationship between sensor output and soil water content (Kaatze and Huebner, 2010).

In previous wireless soil water content sensing networks, we have relied on the use of capacitance sensors, such as the EC-5 and ECH$_2$O-TE sensor (Bogena et al., 2007; Rosenbaum et al., 2010). These capacitance sensors operate at a relatively low measurement frequency of 70 MHz, and the sensor output therefore depends to some extents on the electrical conductivity and imaginary dielectric permittivity of the soil (Kelleners et al., 2005; Kizito et al., 2008; Robinson et al., 2005b). Kizito et al. (2008) reported that the sensitivity to electrical conductivity decreased considerably using a higher operating frequency of 150 MHz. Experimental results of Campbell (1990) suggested that the frequency should be higher than 50 MHz to avoid low frequency dielectric relaxation effects. However, Kelleners et al. (2005) found that the frequency must be above 500 MHz to obtain the most reliable estimates of the real part of the dielectric permittivity in conductive soils.

An alternative electromagnetic sensor design amendable to wireless sensing applications is the family of so-called time domain transmission (TDT) sensors. The general operating principle of these sensors is similar to that of the well-established time domain reflectometry (TDR) method, which estimates dielectric permittivity from the propagation velocity of an electromagnetic wave. It is important to realize that there are different approaches to determine this propagation velocity within the family of TDT sensors. Blonquist et al.(2005b) reported on the Acclima TDT, which employs a waveform interpretation process similar to those used by conventional TDR systems to find the propagation velocity. Most other available sensors in this family use the oscillation frequency of a ring oscillator to approximate propagation velocity (e.g. Gro-Point by ESI; SMRT-Y by Rain Bird; TDT Aquaflex by ADCON). A common feature of all these sensors is that all electronics are integrated in the head of the probe, which removes the need for long cables and multiplexers as with the TDR method. This makes these sensors suitable for wireless sensing applications. In addition, these sensors operate at higher frequencies than capacitance methods and are, therefore, expected to provide a higher measurement quality.

Blonquist et al. (2005b) evaluated the Acclima TDT sensor (McCready et al., 2009) and reported that this sensor and reference TDR measurements operated within ±3 permittivity units of each other within a permittivity range of 9 to 80. Unfortunately, the current design of the Acclima TDT sensor as well as of the other aforementioned sensors using ring oscillators do not allow direct insertion in natural soils and their use is currently restricted to applications where the probe can be buried (mainly irrigation management in agricultural soils and turfgrass).

Recently, the SPADE sensor (sceme.de GmbH i.G., Horn-Bad Meinberg, Germany) has become available (Hübner et al., 2009). This sensor also relies on a ring oscillator, but it allows direct insertion into natural soils. An additional benefit of the SPADE sensor within the context of wireless sensor networks is the very low power input (~ 50 mA). Since wireless sensor networks typically rely on batteries, very low power consumption is needed to keep the network operational for several years. A disadvantage of the SPADE probe design is that probe calibration is required to relate the sensor output to soil water content because the sensor waveguides are contained within an epoxy molding material for probe rigidity.

There are two main strategies to calibrate sensor output to soil water content. The first strategy is to directly calibrate each sensor against soil water content. However, considering the high number of sensors normally used in wireless sensor networks, such a direct calibration is often too labor intensive and time consuming. Instead, we propose to use the two-step calibration procedure of Jones et al. (2005). The first step of this calibration procedure relies on measurements in reference liquids with a known apparent dielectric permittivity, which are used to obtain an empirical model that relates sensor output and apparent dielectric permittivity. Such an empirical model can either be derived for each individual sensor (i.e. a sensor-specific calibration), or a single 'universal' empirical model can be derived from a selection of sensors. In the second step, the apparent dielectric permittivity is related to soil water content using an empirical (Topp et al., 1980) or semi-theoretical model (Birchak et al., 1974). An additional advantage of this method is that there is no need to recalibrate the sensors when they are installed in a different soil.

Recent studies have shown that all electromagnetic soil water content sensors are sensitive to temperature in some extent (Blonquist et al., 2005a; Pepin et al., 1995). Four types of temperature effects on dielectric permittivity measurements are important to consider. First, the influence of temperature on the apparent dielectric permittivity of water (ε_{water}) needs to be considered, i.e. ε_{water} approximately decreases with 0.7 % per °C (Weast, 1986). This decrease of ε_{water} with increasing temperature explains why the bulk dielectric permittivity of sandy soils decreases with increasing temperature (Blonquist et al., 2005a; Pepin et al., 1995). Or and Wraith (1999) investigated how temperature affects the bulk dielectric permittivity of a range of soils and reported that the bulk dielectric permittivity can also increase with increasing temperature, in particular for wet soils with a high specific surface area. This increase of the dielectric permittivity with increasing temperature was attributed to the release of low-permittivity bound water from the electrical double layer that is formed near negatively charged solid surfaces. A third effect of temperature on the dielectric permittivity is through the temperature dependence of soil bulk electrical conductivity. The degree to which bulk electrical conductivity affects the measured permittivity depends of the frequency of the electromagnetic wave used to interrogate the soil. At higher frequencies (> 500 MHz), the effect on permittivity is much reduced (Schwartz et al., 2009). Finally, the sensor output from electromagnetic soil water content sensors is also directly influenced by temperature (Blonquist et al., 2005a; Rosenbaum et al., 2011). These competing effects explain why a wide range of temperature sensitivities have been observed for soil dielectric permittivity measurements.

2.3 Materials and Methods

2.3.1 The SPADE sensor

The propagation velocity (v_p) of electromagnetic waves in soils is given by:

$$v_p = \frac{c}{\sqrt{\mu_r \varepsilon_r}} \qquad \text{Eq. 2. 1}$$

where c is the speed of light in vacuum (3×10^8 ms^{-1}), μ_r and ε_r are the magnetic permeability and the dielectric permittivity of the medium relative to vacuum, respectively. As most soils are non-magnetic (Van Dam et al., 2002), μ_r is typically equal to 1 and the propagation velocity depends only on ε_r. Because of the large permittivity contrast between water (~ 80) and other soil constituents (air: 1; solid phase: 2-9), the soil bulk permittivity is well suited to sense soil water content (Topp et al., 1980).

The SPADE sensor is a ring oscillator (Hübner et al., 2009). A line driver of an ECL logic family emits a steep pulse (< 300ps pulse rise and fall time). The pulse travels along an unshielded transmission line buried in soil, where the propagation velocity depends on the soil dielectric permittivity (Eq. 2. 1). The pulse is inverted before it is fed back to the input of the line driver. This results in an oscillation frequency, f_{osc}, which depends on the following components:

$$f_{osc} = \frac{1}{T_{\varepsilon_r} + t_{pd} + t_{rf}} * \frac{1}{2} \qquad \text{Eq. 2. 2}$$

where T_{ε_r} is the pulse travel time along the unshielded transmission line that depends on the soil dielectric permittivity, t_{pd} is the propagation delay of the ECL gate (typically 250 ps), and t_{rf} expresses the influence of the pulse rise and fall time and the switching of the differential

input amplifier (e.g. the switching mechanism and thresholds). The factor $\frac{1}{2}$ indicates that a logical 1 followed by a logical 0 (two travelling signal edges) make a full signal period. The oscillation frequency is approximately 150 MHz in water and 340 MHz in air.

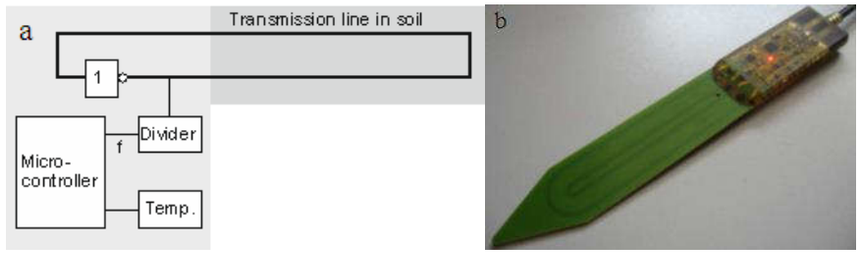

Figure 2. 1. (a) Block diagram and (b) the printed circuit board of the SPADE sensor, size: 20 cm×3 cm×0.2 cm (Hübner et al., 2009).

The design of the SPADE sensor is illustrated in Figure 2. 1. The transmission line consists of two copper strips embedded in a 4 layer epoxy printed circuit board (PCB). The PCB is 3 cm wide and the part forming the ring oscillator is 12 cm. The sensor head that contains the sensor is 8 cm long. The power requirement of the SPADE sensor is very low with about 50 mA during the measurement time of about 50 ms. The SPADE sensor also determines temperature using a sensor with an accuracy of ±0.5 °C from -10 °C to 85 °C, which increases the total measurement time to ~1 cc. The sensor provides two analog output channels (0-2.8 V) or a digital interface (RS485). In this study, we used the analog output channels.

2.3.2 Reference liquids

While assessing the sensor characteristics, it is important to realize that in addition to the dielectric permittivity, EM measurements are sensitive to dielectric relaxation, electrical conductivity, and temperature (Pepin et al., 1995; Topp et al., 2000). To avoid unwanted noise due to these secondary factors as well as contact problems between medium and sensor, liquids with known dielectric properties are used instead of soil for the calibration. As suggested by Jones et al. (Jones et al., 2005) and Bogena et al. (2007), we used 2-Isopropoxyethanol (i-C_3E_1) and 1,4-Dioxane (D), which have been described in detail elsewhere (Kaatze et al., 1996; Schwank et al., 2006). Five reference liquids (pure Dioxane and four i-C_3E_1/water mixtures with a defined volume fraction of i-C_3E_1; denoted as M_1 to M_5) were selected from the reference liquids described by Bogena et al. (2007). These five reference liquids evenly cover the permittivity range from 2.2 to 34.8, which includes most of the dielectric permittivity values obtained in natural soils. The frequency-dependent complex dielectric permittivity of the four i-C_3E_1/water mixtures (M_2 to M_5) at 25 °C was measured in a frequency range from 0.5 to 10 GHz using a dielectric probe kit with a slim probe (Agilent 85070E, Agilent Technologies) and a network analyzer (HP 8720A, Agilent Technologies) by Rosenbaum et al. (2010). The properties of M_1 (pure Dioxane) were not measured because they are well documented (Schwank et al., 2006). The volume fractions and the reference dielectric permittivity of all five reference liquids are listed in Table 2. 1.

Table 2. 1. Dielectric permittivity of the reference liquids at 25 °C. Data were obtained by Rosenbaum et al. (2011).

Reference liquid	Medium	Volume fraction		ε_{ref}
		Dioxane / i-C_3E_1* [-]	Deionized Water [-]	[-]
M_1	Dioxane	1	0	2.2
M_2	Dioxane	0.9	0.1	6.65
M_3	i-C_3E_1*	0.92	0.08	18.14
M_4	i-C_3E_1*	0.8	0.2	26.26
M_5	i-C_3E_1*	0.68	0.32	34.82

* 2-Isopropoxyethanol

2.3.3 Measurement set-up and sensor output determination

The laboratory measurements made with the SPADE sensor use a stable 5 Voltage DC power supply (Agilent, E3646A, 60W dual output power supply), and a high precision digital multimeter (Escort 99 TRUE TMS, accuracy: 0.025 %) to determine the sensor output voltage (V). Several precautions were taken during the measurements. First, the liquids were thoroughly mixed using a magnetic stirrer. No effects of the stirring magnet on the sensor output were found. Second, the SPADE sensors were completely and centrally immersed in the large 5 liter cuboid bottle (length: 28 cm, diameter: 15.2 cm) to ensure that the sampling volume was contained within the bottle. Third, the 1.5 m long sensor cable was fixated with a Polyvinylchloride bar to reduce effects of cable movement and positioning on the measurements. Finally, possible degrading effects of reference liquids on the sensor epoxy resin body were minimized by carefully cleaning the sensor after each measurement and minimizing the contact time. This measurement set-up was used for all measurements in reference liquids described below.

2.3.4 Sensor-to-sensor variability

To assess the sensor-to-sensor variability, we used five SPADE sensors in a replication experiment. In this experiment, we made five measurements with five SPADE sensors in reference liquid M_5 with a dielectric permittivity of 34.82 at 25 °C (see Table 2. 1). For each measurement, the sensor was disconnected and the cable position was changed.

2.3.5 Relating sensor output to dielectric permittivity

The SPADE sensor internally converts the measured oscillation frequency into a voltage output, which has to be converted to an apparent dielectric permittivity, K_a, using an appropriate empirical function. We determined the sensor output of 60 SPADE sensors in all five reference liquids. We considered two empirical functions (Bogena et al., 2007; Jones et al., 2005):

$$K_a = \gamma_i + \frac{1}{\alpha_i + {\beta_i}/{v}} \quad \text{Eq. 2. 3}$$

$$K_a = (\alpha_i * v^{\beta_i} + \gamma_i)^2 \quad \text{Eq. 2. 4}$$

where v is the sensor output (voltage), and α_i, β_i, and γ_i are the fitting parameters. The root mean square error (RMSE) between the predicted K_a and the known reference permittivity (Table 2. 1) was used to quantify the accuracy of the empirical functions.

2.3.6 Derivation of the temperature correction function

In order to estimate how temperature directly affects the sensor output of the SPADE sensor, we determined the sensor output of six SPADE sensors in four reference liquids (M_2 to M_5;

M_1 was excluded as the melting point is 11.8 °C). The temperature of these reference liquids was varied within a temperature range from 5 °C to 40 °C in steps of 5 °C using a circulating water bath controlled by a thermostat. A sensor-specific model was used to relate sensor output and dielectric permittivity for each sensor. The difference between the measured apparent dielectric permittivity ($K_{a,T}$) and the reference static permittivity (ε_{ref}) is used to quantify the effect of temperature on the measured apparent dielectric permittivity:

$$\Delta K_{a,T} = K_{a,T} - \varepsilon_{ref} \quad \text{Eq. 2. 5}$$

A positive value of $\Delta K_{a,T}$ indicates an overestimation of the reference permittivity, while a negative value of $\Delta K_{a,T}$ implies an underestimation of the reference permittivity. Following Rosenbaum et al. (2011), an empirical polynomial function was used to obtain a function that describes $\Delta K_{a,T}$ as a function of T and K_a:

$$\Delta K_{a,T} = a * K_a^2 + b * T^2 + c * K_a + d * T + e * K_a T + f \quad \text{Eq. 2. 6}$$

where a to f are fitting parameters that were determined using a stepwise regression method in MATLAB (The MathWorks, Natick, MA). This fitted function was used to correct for temperature effects on the sensor output of the SPADE sensor. As outlined in the introduction, additional effects of temperature on soil dielectric permittivity are present in soil and these should also be accounted for in addition to the effect of temperature on the sensor output.

2.3.7 Testing of the temperature correction function

To illustrate the plausibility of the apparent dielectric permittivity obtained with the SPADE sensor after temperature correction, we determined how the corrected apparent dielectric permittivity of two soil samples (length: 27 cm, diameter: 15 cm) varied with temperature. The first soil sample was a packed coarse sand with a mean grain size of 0.024 cm (F36,

Quarzwerke Frechen, Germany), which was saturated with deionized water. The second soil sample was an undisturbed silt loam sample took from the Rollesbroich test site, Germany (Korres et al., 2010). In both samples, we installed two SPADE sensors and the entire sensor including the probe head was contained in the sample. A wireless sensor network unit was used to obtain the sensor output of the two SPADE sensors, which was converted to apparent dielectric permittivity using a sensor-specific calibration equation. We additionally installed a 7.5 cm long CS 640-L 3-rod TDR probe attached to a TDR 100 cable tester (Campbell Scientific, Logan, UT). Temperature was varied from 5 °C to 40 °C in 5 °C temperature steps using a circulating water bath controlled by a thermostat (Figure 2. 2). The sides of the columns were isolated to avoid temperature gradients. In order to assess variability in sensor output, we repeated each experiment three times.

To evaluate the experimental results for these soil samples, the change in the apparent dielectric permittivity with rising temperature was modeled using the CRIM model (Birchak et al., 1974):

$$K_a{}^{\beta} = (1 - \eta) * K_{solid}^{\beta} + (\eta - \theta) * K_{air}^{\beta} + \theta * K_{water}^{\beta} \qquad \text{Eq. 2. 7}$$

where η is the porosity of the soil, 1-η is the solid fraction, η-θ is the air fraction, β is a shape factor which is assumed to be 0.5 (Birchak et al., 1974), K_a is the apparent dielectric permittivity measured by the sensors, and K_{water}, K_{solid}, and K_{air} are the permittivity of water, solids, and air, respectively. The dielectric permittivity of air (K_{air}) is 1, and that of water (K_{water}) is a function of temperature, and can be calculated by (Weast, 1986):

$$\mathrm{K_{water}} = 78.5 * [1 - 4.579 * 10^{-3}(\mathrm{T} - 25) + 1.19 * 10^{-5}(\mathrm{T} - 25)^2 - 2.8 * 10^{-8}(\mathrm{T} - 25)^2\,] \qquad \text{Eq. 2. 8}$$

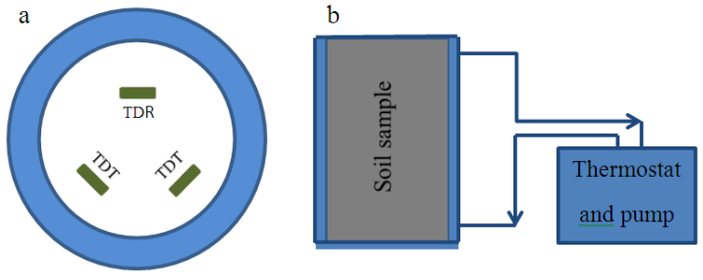

Figure 2. 2. (a) Vertical view of the soil container; the SPADE sensors and the TDR sensor were completely inserted in the soil; (b) schematic view of experimental setup using the saturated coarse sand and the undisturbed soil sample from the Rollesbroich test site.

The permittivity of K_{solid} was fitted. The porosity and soil water content of the samples were derived using the gravimetric method (oven drying at 105 °C, 24 hours). It is important to note here that this modeling approach assumes that the change in permittivity with changing temperature is solely related to the temperature sensitivity of the dielectric permittivity of water after correction for temperature effects on the sensor output. Although this is a reasonable approximation for the sand and soil sample used in this study, more complex modeling approaches such as those presented by Schwartz et al. (2009) and Wagner et al. (2011) should be considered for soils with a high surface area because bound water relaxation and bulk electrical conductivity effects on the dielectric permittivity are expected to be more important for such soils.

2.4 Results and Discussion

2.4.1 Sensor-to-sensor variability

The results of the replication experiment in M_5 show that the repeat measurements with each of the five sensors were very close together (Figure 2. 3), which indicated that instrument noise was low and that the experimental procedure was repeatable. To test whether the sensor output was significantly different, an ANOVA was conducted. In this statistical analysis, the total variance is divided into two parts: the variance between sensors (sensor-to-sensor variability), which is due to the sensor production process; and the variance between replication measurements (noise), which is caused by the repeatability of the experimental procedure. The results of this ANOVA indicated that at least one of the SPADE sensors provided significantly different sensor output (F value of 83.1,Table 2. 2). The observed variability was slightly lower than observed for the EC-5 capacitance soil water content sensor (F value of 87.5), which was evaluated by (Rosenbaum et al., 2010) for sensor-to-sensor variability analyze.

Table 2. 2. ANOVA results of measurement in reference liquid M_5 with five SPADE sensors and five replication measurements per sensor.

Source of Variation	SS	df	MS	F	P-value	F critical
Sensor to sensor variability	0.00331	4	0.00083	83.1	3.61E-12	2.87
Noise	0.000199	20	9.94E-06			
Total	0.00350	24				

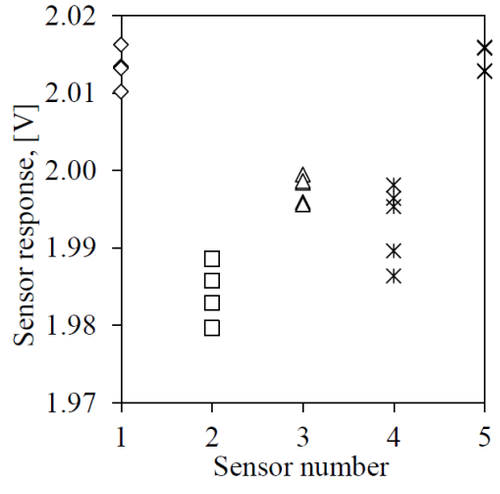

Figure 2. 3. Replication experiments consisting of five replicate measurements with five SPADE sensors in reference liquid M_5.

2.4.2 Relating sensor output to dielectric permittivity

The sensor output for all 60 SPADE sensors for each of the five reference liquids is presented in Figure 2. 4. With increasing permittivity, the sensor output voltages increased in a non-linear way. It is also observed that the variation in measured sensor output increased with increasing permittivity, which is also confirmed by the standard deviation of the measurements which increases from 0.0074 to 0.0166 (Table 2. 3). The two empirical functions fitted to all of these measurements are also presented in Figure 2. 4. The best fitting parameters are presented in Table 2. 4. The RMSE of the sensor output for the first empirical function (Eq. 2. 3) was 0.0188, which was less than the RMSE of 0.0772 that was obtained for the second empirical function (Eq. 2. 4). Therefore, Eq. 2. 3 was selected to calibrate the SPADE sensors. Table 2. 5 provides the RMSE between measured and predicted K_a for each reference liquid for this 'universal' calibration. Clearly, the quality of the fit was lower for

higher permittivity, which was expected because of the observed sensor-to-sensor variability in reference liquid M_5. The RMSE of K_a value was 0.75 for this 'universal' calibration was considerably lower than the RMSE obtained for the calibration of the EC-5 capacitance probe in Rosenbaum et al. (2010) because the sensor-to-sensor variability of the SPADE sensor was smaller.

Table 2. 3. Statistical summary of the sensor output of 60 SPADE sensors in five reference liquids.

	Mean [V], [-]	STD [V], [-]	CV* [%]
M1	0.6494	0.0074	1.14
M2	1.2598	0.0100	0.79
M3	1.7680	0.0124	0.70
M4	1.9150	0.0139	0.72
M5	1.9978	0.0166	0.83

*CV is the coefficient of variation

Table 2. 4. Fitting parameters of the 'universal' calibration curve of SPADE sensors and the RMSE between measured and predicted reference dielectric permittivity.

	α	β	γ	RMSE
Eq.3	-0.1502	0.3612	-0.5199	0.0188
Eq.4	-0.3589	3.5190	-1.5777	0.0772

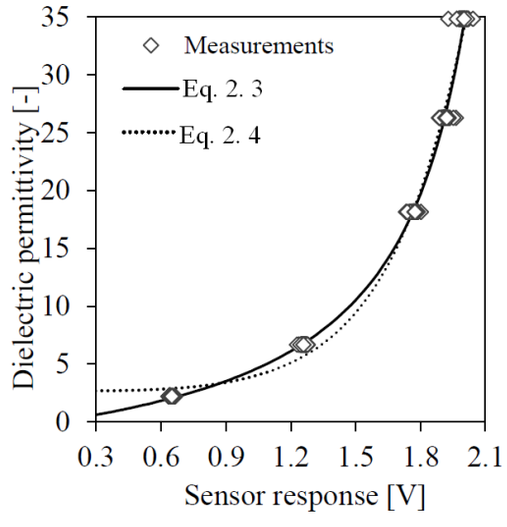

Figure 2. 4. Sensor output of 60 SPADE sensors in five reference liquids. The two fitted 'universal' calibration relationships are also presented.

Table 2. 5. The RMSE between apparent dielectric permittivity *Ka* (determined using sensor-specific and universal calibration) and the reference permittivity ε_{ref} as well as the corresponding (equivalent) soil water content, θ, for measurements with 60 SPADE sensors in five reference liquids (M_1-M_5) at 25°C.

Standard liquids	Sensor-specific calibration		Universal calibration	
	RMSE *Ka* [-]	RMSE θ* [$cm^3 \cdot cm^{-3}$]	RMSE *Ka* [-]	RMSE θ* [$cm^3 \cdot cm^{-3}$]
M1	0.199	0.00535	0.543	0.00695
M2	0.280	0.00624	0.804	0.00777
M3	0.156	0.00210	0.581	0.00628
M4	0.312	0.00290	0.893	0.00755
M5	0.127	0.00830	1.156	0.00873
all	0.226	0.00403	0.753	0.00750

* Equivalent soil water content θ estimated by the polynomial empirical permittivity-soil water content relationship of Topp (1980).

To evaluate to what extent a sensor-specific calibration can remove the sensor-to-sensor variability, we compared the RMSE obtained with a sensor-specific and a single 'universal' calibration in each reference liquid (Table 2. 5). Clearly, the RMSE decreased with the use of a sensor-specific calibration for each reference liquid, which indicates that a sensor-specific calibration can further improve the accuracy of soil water content measurements with the SPADE sensor. Expressed in equivalent soil water content, the overall quality of the calibration between sensor output and apparent dielectric permittivity improved from 0.008 cm^3cm^{-3} to 0.004 cm^3cm^{-3} using the sensor-specific calibration.

2.4.3 Temperature correction function for sensor output

The results from the temperature experiment are presented in Figure 2. 5. With increasing temperature, the reference permittivity ε_{ref} decreased as already discussed by Rosenbaum et al. (2011). The temperature dependence of the dielectric permittivity of the reference liquids increased with increasing permittivity of the liquids because of the increasing volume fraction of water. Figure 2. 5 also shows that the mean temperature dependence of the apparent dielectric permittivity for the six SPADE sensors (error bars indicate the standard error of the mean). The apparent dielectric permittivity measured by the SPADE sensors showed the same tendency as the reference permittivity with respect to temperature. However, for temperature lower than 25°C the SPADE sensor underestimates the reference dielectric permittivity, while it overestimates the reference dielectric permittivity at higher temperature (> 25 °C). In addition, the deviations between measured apparent dielectric permittivity and reference permittivity increased with increasing permittivity (Figure 2. 5).

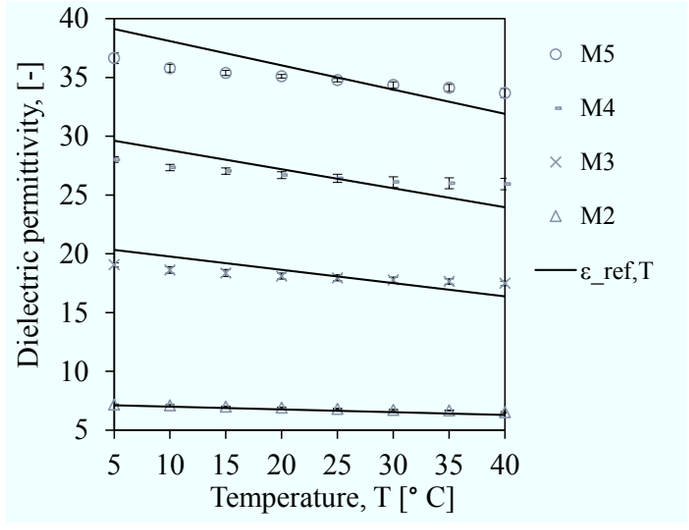

Figure 2. 5. The reference permittivity (solid line) and the apparent dielectric permittivity $K_{a,T}$ for the SPADE sensors as a function of temperature. The temperature dependence of the reference permittivity for M_2 to M_5 was obtained from Rosenbaum et al. (2011). The error bars are the standard error of the mean estimated from six sensors.

Figure 2. 5 exhibits the mean temperature effect ($\Delta K_{a,T}$) calculated according to Eq. 2. 5 for all reference liquids and temperatures. We observed that the $\Delta K_{a,T}$ was close to but not equal to zero at 25 °C (also see Figure 2. 5). This is related to the accuracy of the sensor-specific calibrations used to convert sensor output to dielectric permittivity. Therefore, all data measured in each reference liquid were shifted to make $\Delta K_{a,T}$ equal to zero at 25 °C. The largest deviations between measured and reference dielectric permittivity were found in M_5 at 5 °C ($\Delta K_{a,T}$ = -2.85, equivalent to 0.031 cm^3cm^{-3}) and 40 °C ($\Delta K_{a,T}$ = 1.73, equivalent to 0.014 cm^3cm^{-3}). The observed deviations for the SPADE sensor were similar to those observed for the EC-5 capacitance probe evaluated by Rosenbaum et al. (2011).

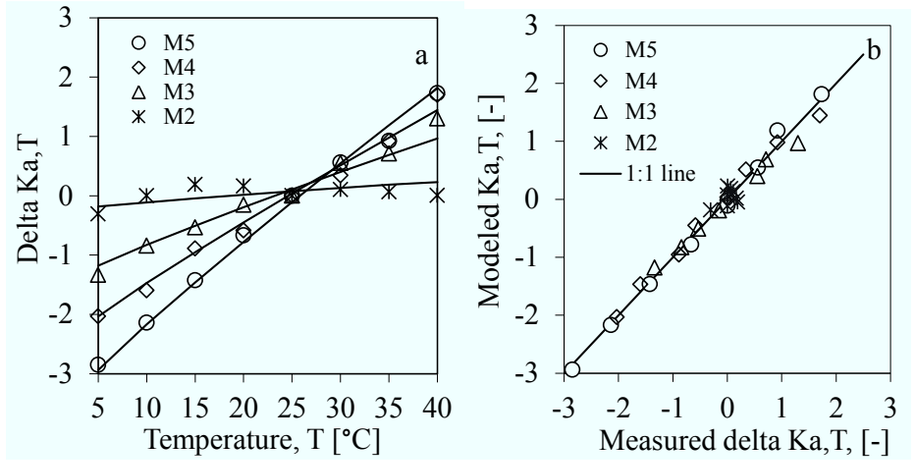

Figure 2. 6. (a) Measured mean temperature effect $\Delta K_{a,T}$ (marker) and predicted temperature effect using Eq. 2. 6 as a function of temperature; and (b) the modeled and measured mean temperature effect of $\Delta K_{a,T}$.

Table 2. 6. Parameters of the empirical polynomial function describing the temperature effect on the SPADE sensor output determined by stepwise regression. The RMSE and R^2 of the fit are also reported.

a	*b**	*c*	*d*	*e*	*f*	RMSE	R^2
-0.00055	0	0.0043	-0.0906	-0.0176	0.4298	0.1489	0.9831

The second order polynomial function relating $\Delta K_{a,T}$ to T and K_a (Eq. 2. 6) fitted the measurements well (R^2 = 0.9831, RMSE = 0.1489) (Figure 2. 6). The fitting parameters are provided in Table 2. 6. Only one regression parameter '*b*' was removed in the stepwise regression procedure because it was insignificantly different from zero at a 95% confidence level. The good agreement is also evident from Figure 2. 6, where the measured and the modeled $\Delta K_{a,T}$ were plotted against each other.

2.4.4 Testing the temperature correction function

Figure 2. 7 shows the apparent dielectric permittivity measured with the SPADE sensor and TDR as a function of temperature for the coarse sand sample. The soil water content of this sample was 0.4114 cm^3cm^{-3} and the porosity was 0.4129 cm^3cm^{-3}. It can be seen that the uncorrected apparent dielectric permittivity did not significantly change with temperature. However, the reference TDR measurements did show a decrease in apparent dielectric permittivity, which is not surprising because in coarse sand the permittivity of free water by far is the greatest influence on apparent permittivity and the permittivity of free water declines as temperature increases. In addition, it is well established that TDR measurements are less affected by temperature (Assouline et al., 2010; Blonquist et al., 2005b; Robinson et al., 2005a). We modeled the decrease of permittivity with increasing temperature assuming that the permittivity of water is the only contributing factor to the temperature dependency of the dielectric permittivity. After fitting the K_{solid} of the CRIM model to the TDR measurements, the modeled temperature dependence fitted well with the TDR measurements with a RMSE of 0.1694. The fitted value of K_{solid} was 5.75, which corresponds well to K_{solid} values reported for quartz and other soil minerals (Robinson, 2004; Rosenbaum et al., 2011). After the application of the temperature correction function (Eq. 2. 6) to the SPADE measurements, the corrected apparent dielectric permittivity of the coarse sand decreased with increasing temperature. The corrected apparent dielectric permittivity fitted well with the reference TDR measurements. We also fitted the CRIM model to the temperature-corrected SPADE measurements. This resulted in a RMSE of 0.1983, which was only slightly higher than the RMSE obtained for TDR. The fitted K_{solid} was 5.81 for the corrected SPADE

sensor measurements, which was very close to the value obtained for TDR. These results indicated that our temperature correction function works well for saturated coarse sand.

The same experiment was performed for an undisturbed soil sample took from the Rollesbroich test site (Figure 2. 7). The soil water content of this sample was 0.4225 cm^3cm^{-3} and the porosity of this sample was 0.4942 cm^3cm^{-3}. Again, the uncorrected apparent dielectric permittivity measurements with the SPADE sensor hardly decreased with temperature. In addition, the standard deviation of the three measurements for each temperature was higher as compared to the TDR and SPADE sensor measurements in the saturated coarse sand. As the permittivity of these two samples was similar, we can exclude that this is related to the increasing measurements noise that was observed with increasing permittivity. Instead, we attribute the larger standard deviation to limited soil water redistribution during the experiment because the silt loam sample was not saturated and not as homogeneous as the saturated coarse sand.

After the application of the temperature correction function, the corrected apparent dielectric permittivity of the SPADE sensor matched well with the reference TDR measurements. The fitted K_{solid} of 5.97 for the TDR measurements was again close to the K_{solid} of 5.92 obtained for the corrected SPADE measurements, and the quality of the fitting was also very similar (an RMSE of 0.1446 for TDR and 0.1623 for SPADE sensor measurements). This good correspondence between measurements and modeling is an indication that bound water effects on the temperature sensitivity of the soil dielectric permittivity do not need to be considered at the Rollesbroich test site, despite the relatively fine silt loam texture.

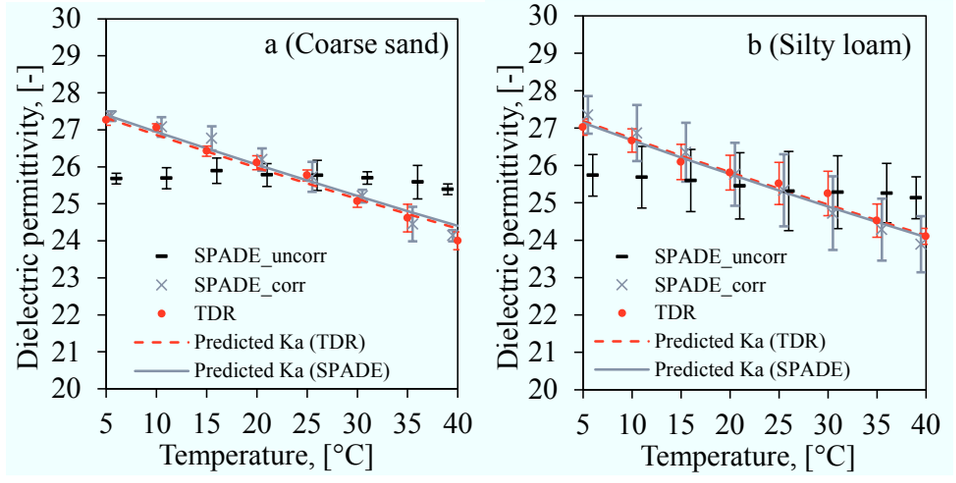

Figure 2. 7. Temperature dependence of the apparent dielectric permittivity measured with TDR and SPADE sensors for (a) a packed saturated coarse sand and (b) an undisturbed silt loam. The black rectangles are the uncorrected apparent dielectric permittivity (K_a) obtained with the SPADE sensors, the gray crosses are temperature-corrected SPADE measurements, and the red dots are the reference TDR measurements. The black and red lines are modeling results for the CRIM model. The error bars indicate the standard deviation of three experiments. The temperature values of the uncorrected K_a and the temperature-corrected K_a are shifted by 1 and 0.5°C from the actual temperature to improve visibility.

2.5 Conclusions

In this paper, we evaluated the SPADE sensor with respect to sensor-to-sensor variability, accuracy of calibration between sensor output and dielectric permittivity, and the effect of temperature on the sensor output. A replication experiment shows that sensor-to-sensor variability was significant, and much larger than the measurement noise introduced by the instrumentation and our experimental procedures. We calibrated the sensor output of 60

SPADE sensors to permittivity using a standard procedure based on a reference liquids with a known dielectric permittivity ($2.2 < \varepsilon_{ref} < 34.8$). Our results show that a sensor-specific calibration improved the accuracy of the calibration, although a single 'universal' calibration also provided a high accuracy. Sensor-specific calibration is associated with additional effort and the results presented here can be used to decide whether sensor-specific calibration is required given the accuracy requirements of a particular application.

Temperature has a significant influence on the sensor output of the SPADE sensor. The results show that the effect of temperature effect on the sensor output depends on the dielectric permittivity of the medium. The largest effect of temperature was found for high apparent dielectric permittivity, which means that the effect of temperature on the sensor output is larger in wet soil than in dry soil. A temperature correction function was derived and tested using two different soil samples. Both samples were exposed to temperature variations and the corrected apparent dielectric permittivity showed good agreement with reference TDR measurements and predicted changes in dielectric permittivity as a function of temperature that were obtained from the CRIM model.

A site specific calibration between the permittivity and soil water content was derived using the CRIM model for different depths. Although by considering the spatial variability of soil properties at each sensor unit and soil depth will improve the model accuracy of soil water content predictions. The large effort required to obtain this additional soil information is too large considering the modest increase in accuracy of the soil water content measurements. We did not consider the CRIM model with spatial distributed porosity for the wireless sensor network.

In future, the accuracy of the SPADE sensor will be further tested in the field. Since we have already installed a wireless sensor network consisting of SPADE sensors at the Rollesbroich test site, the temperature correction function will be tested with continuous field measurements under natural conditions. The improved soil water content measurements at the catchment scale will be ultimately used to improve hydrological understanding of this small headwater catchment and to validate high resolution remote sensing soil water content products.

3 Effects of soil hydraulic properties on the spatial variability of soil water content: evidence from sensor network data and inverse modeling

This chapter has been published as: W. Qu, H. R. Bogena, J. A. Huisman, G. Martinez, Y. A. Pachepsky, H. Vereecken. Effects of soil hydraulic properties on the spatial variability of soil water content: Evidence from sensor network data and inverse modeling. Vadose Zone Journal, 2014, 13(12). doi: 10.2136/vzj2014.07.0099.

3.1 Objectives

The objective of this study was to analyze an extensive soil water content data set acquired with a wireless sensor network in the Rollesbroich catchment (Germany) in order to investigate whether spatial variability of soil water content is related to spatial variation in soil hydraulic properties. The soil hydraulic parameters were inversely estimated from measured soil water content time series using information on the distribution and correlation of hydraulic parameters derived from the Rosetta program. The spatial variation in inversely estimated hydraulic parameters was then compared to the spatial variation of soil water content and saturation degree as expressed by the *MRD*.

3.2 Introduction

Understanding spatial variation of soil water content is important in a multitude of hydrological and engineering applications (Bogena et al., 2010; Vereecken et al., 2007). However, characterizing the spatial variation of soil water content is challenging because it is affected by the heterogeneity of soil, atmospheric forcing, vegetation, and topography (Vanderlinden et al., 2012; Vereecken et al., 2008; Vereecken et al., 2014; Zhao et al., 2013). Nevertheless, accurate characterization of spatial behavior of soil water content is important, for data assimilation method in hydrological models (Heathman et al., 2003; Pan et al., 2012), calibration and validation of large scale remote sensing retrievals of soil water content (Choi and Jacobs, 2007; Famiglietti et al., 1999; Montzka et al., 2011), estimating uncertainty in hydrological predictions (Heuvelink and Webster, 2001), designing sensor networks and optimizing the number of sensors (Heathman et al., 2009; Mohanty and Skaggs, 2001), and upscaling and downscaling of soil water content information (Cosh et al., 2004; Cosh et al., 2006; Jacobs et al., 2004).

One of the most widely used methods to investigate spatial behavior of soil water content is the statistical analysis of the *MRD* to characterize spatial variability in combination with the analysis of standard deviation of the relative differences (*SDRD*) to describe rank stability. This type of statistical analysis is commonly referred to as temporal stability analysis. The concept of temporal stability was first proposed by Vachaud et al. (1985) to determine representative locations within a field in order to improve sampling efficiency while maintaining accuracy. More recently, it has also been used to describe the persistence of spatial patterns and to characterize the behavior of soil water content variability (Pachepsky et al., 2005; Vanderlinden et al., 2012).

The majority of studies dealing with the spatial variability of soil water content rely on few snapshots of soil water content variation in time that ideally include both wet and dry conditions (Avila et al., 2010; Brocca et al., 2009; Grayson and Western, 1998; Schneider et al., 2008b; Starks et al., 2006). Soil water content observations with high measurement frequency and over a large range of saturation conditions enable more comprehensive investigations of spatial behavior of soil water content (Cosh et al., 2008; Cosh et al., 2006; Mittelbach and Seneviratne, 2012). Wireless sensor network technology is ideally suited to provide such continuous measurements of soil water content at the catchment scale (Bogena et al., 2010; Qu et al., 2013).

Although a large number of publications on spatial variability of soil water content already exist, the controlling factors are still not well understood. Previous studies have shown that multiple factors, such as climate (Martinez et al., 2014), topography (Biswas and Si, 2011;

Hu et al., 2010a), soil properties (Martinez et al., 2013; Williams et al., 2009), and vegetation (Gomez-Plaza et al., 2001; Mohanty and Skaggs, 2001) affect the *MRD* of soil water content, and that these factors tend to interact (Baroni et al., 2013; Vanderlinden et al., 2012). Vachaud et al. (1985) were the first to suggest that soil texture affects the temporal stability and this was confirmed by Hu et al. (2010a). Gomez-Plaza et al. (2001) also found that soil texture together with slope were the main factors controlling *MRD* of soil water content in a semi-arid catchment with sparse vegetation. Cosh et al. (2008) reported that dry bulk density, clay content and sand content explained nearly 50% of the temporal stability, and that topographical effects were less important in defining representativeness and stability. Since it is well established that soil texture is correlated with soil hydraulic properties (Schaap et al., 2001; Vereecken et al., 2010; Wosten et al., 1999), it can also be expected that soil hydraulic properties affect spatial behavior of soil water content.

Spatially distributed simulations have been used to investigate to what extent soil hydraulic properties affect the *MRD* of soil water content. For instance, Kim and Stricker (1996) used independent soil columns with spatially random fields of vertically uniform hydraulic characteristics and showed that the heterogeneity of soil hydraulic properties has a strong effect on the mean annual water budget. More recently, Martinez et al. (2013) presented a simulation study where a linear relationship between saturated soil hydraulic conductivity and the *MRD* of soil water content was found. However, this study relied on a simplified modeling approach based on a lognormal distribution of K_s, without considering relationships between K_s and other hydraulic parameters. Therefore, it remains unclear whether such correlations between *MRD* and soil hydraulic properties can also be expected for real-world conditions.

In order to explore potential correlations between soil hydraulic properties and the spatial variability of soil water content in the field, hydraulic parameters need to be determined at locations where soil water content is measured using either direct or indirect methods. In case of direct methods, the hydraulic parameters are estimated by fitting the water retention and unsaturated hydraulic conductivity curve to experimental data obtained from soil cores in the laboratory. However, such direct methods are labor intensive and time consuming. If measured time series of soil water content at several depths are available, inverse modeling may be an appropriate alternative to obtain in-situ soil hydraulic parameter estimates (Bauer et al., 2012; Ritter et al., 2003; Vrugt et al., 2003; Zhang et al., 2003). Previous inverse modeling studies that have attempted to estimate soil hydraulic parameters from measured time series of soil water content have shown that the consideration of information on correlations between soil hydraulic parameters was useful to retrieve realistic parameter combinations (Carsel and Parrish, 1988; Mertens et al., 2004; Scharnagl et al., 2011). Such information can be estimated from basic soil information such as the sand, silt and clay fractions, bulk density and/or organic matter content by using pedotransfer functions (Pachepsky et al., 2006; Vereecken et al., 2010; Wosten et al., 2001).

3.3. Materials and Methods

3.3.1 Site description

The Rollesbroich catchment (50°37'27"N, 6°18'17"E) is located in the Eifel and covers an area of 27 ha with altitudes ranging from 474 to 518 m.a.s.l. Mean annual air temperature and precipitation are 7.7 °C and 103.3 cm, respectively. The dominant soils are Cambisols in the southern part and Stagnosols in the northern part of the catchment. The grassland vegetation is dominated by perennial ryegrass (Lolium perenne) and smooth meadow grass (Poa

pratensis). Our study was focused on the southern part of the catchment with relatively flat slopes (Figure 3. 1). The average slope of our test site is 1.63° (min.: 0.35°, max.: 3.12°). Therefore, we expect that lateral soil water redistribution is of minor importance.

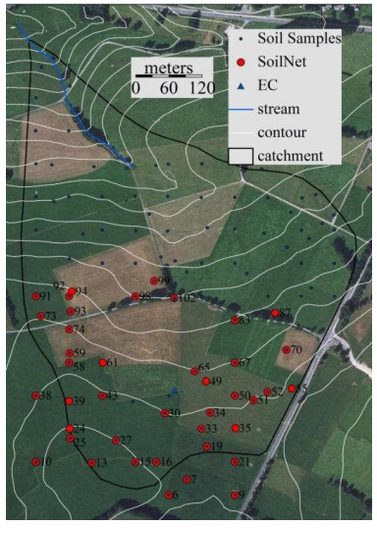

Figure 3. 1. The Rollesbroich catchment and the soil net locations (red dots), the soil sample locations (blue dots), the isolines of elevation at 2.5 m intervals (grey lines) and the climate station (blue triangular).

3.3.2 Soil water content determination

In the framework of the TERENO project (Bogena et al., 2012; Zacharias et al., 2011), the Rollesbroich catchment has been equipped with a wireless soil water content sensor network (SoilNet, 2012). The SPADE soil water content probes (sceme.de GmbH i.G., Horn-Bad Meinberg, Germany; (Hübner et al., 2009)) were installed at 5 cm, 20 cm and 50 cm depth along a vertical profile. In order to increase the measurement volume and enable the examination of inconsistencies (e.g. imperfect contact of sensors with the soil matrix), two

sensors were installed in each depth with a separation of ~8 cm. Sensor deployment followed careful installation procedures to reduce subsequent measurement errors (e.g. no sensors were inserted in direct proximity to worm holes, root holes, cracks, and stones). The SPADE probe is a ring oscillator and the frequency of the oscillator is a function of the dielectric permittivity of the surrounding medium, which is strongly depended on the water content of the soil because of the high permittivity of water ($\varepsilon_w \approx 80$) as compared to mineral soil solids ($\varepsilon_s \approx 2\text{-}9$), and air ($\varepsilon_a \approx 1$). The SPADE probe was calibrated using a two-step calibration procedure proposed by Jones et al. (2005). In a first step, an empirical model was developed using laboratory measurements to relate the sensor response to the apparent dielectric permittivity (Qu et al., 2013). In the next step, the CRIM model proposed by Birchak et al. (1974) was used to relate apparent dielectric permittivity to soil water content. To adjust the CRIM model to the soils of the test site, fifteen undisturbed soil samples (length 7.7 cm, diameter 5.0 cm) were taken from three different depths, ranging from approximately 5 to 13 cm, 20 to 28 cm, and 45 to 55 cm. The volumetric soil water content was determined gravimetrically and the apparent dielectric permittivity of each sample was determined from measurements with a CS 640-L 3-rod TDR probe attached to a TDR 100 device (Campbell Scientific, Logan, UT). The root mean square error (RMSE) associated with soil water content estimation with the SPADE probe was 0.026 cm^3cm^{-3} after the calibration.

After the deployment of the sensor network at the test site, we found that the sensor output showed pronounced diurnal variations related to temperature. Large differences between the two closely-spaced measurements at a single measuring point were also observed. After investigating this in detail, it was established that this behavior was related to the SPADE data acquisition where the first sensor reading was still affected by a charging capacitor

within the sensor. If multiple sensor readings were made sequentially without turning off the sensor, the stability of the measurement considerably improved and the temperature dependence of the measurements disappeared. To correct these temperature-dependent oscillations in sensor reading, two readings were sequentially made at each measurement time for a limited time period. We found that the difference between the first and second sensor reading was highly correlated with temperature and could be fitted with a sensor-specific second-order polynomial function. After deriving these correction functions for all the sensors, we corrected the first measurement of the sensors to obtain consistent time series of soil water content for all locations. After correction, the measurements from the closely-spaced sensors at a single measurement location agreed well with each other (see Appendix B).

In this study, we used the time series of soil water content and soil temperature measured from 1st May 2011 to 1st March 2013. Soil samples were taken at the locations where the soil sensors are installed using COBRA cores (length: 100 cm, diameter 8 cm; Carl Hamm GmbH, Essen, Germany). In total, 273 soil samples were taken from three horizons of the soil profile. The textural composition, organic carbon content, and bulk density were determined using standard laboratory procedures (Table 3. 1).

Table 3. 1. Descriptive of statistics of soil properties for the 273 soil samples in Rollesbroich catchment.

		Clay %	Sand %	Silt %	Bulk density (gcm^{-3})	Carbon content (gkg^{-1})	Porosity (cm^3cm^{-3})
5 cm	mean	18.99	19.90	61.10	0.94	54.47	0.65
	std	2.00	3.82	3.79	0.12	15.82	0.05
20 cm	mean	18.03	20.76	61.20	1.28	34.08	0.52
	std	1.99	4.03	3.46	0.15	16.84	0.05
50 cm	mean	16.50	22.00	61.50	1.52	11.22	0.43
	std	2.40	5.68	4.53	0.16	6.01	0.06

3.3.3 Temporal stability analysis

Temporal stability analysis uses the mean and standard deviation of relative differences (*RDs*) expressed as *MRD* and *SDRD* of soil water content (Vachaud et al., 1985) to describe the spatial pattern of soil water content in the catchment. The *RD* of soil water content are computed from individual measurements of soil water content in location *i* at time *j* ($\theta_{i,j}$) and the areal mean soil water content at a given time ($\overline{\theta}_j$). In particular, the relative difference for location *i* at time *j* is calculated by:

$$RD_{i,j} = \frac{\theta_{i,j} - \overline{\theta}_j}{\overline{\theta}_j} \quad \text{Eq. 3. 1}$$

where $\overline{\theta}_j = \frac{1}{N}\sum_{i=1}^{N} \theta_{i,j}$, and *N* is the number of the measurement locations. The *MRD* for location *i* is calculated by:

$$MRD_i = \frac{1}{T}\sum_{j=1}^{T} RD_{i,j} \quad \text{Eq. 3. 2}$$

where *T* is the total number of measurements at each location. The *SDRD* for location *i* is calculated using:

$$SDRD_i = \sqrt{\sum_{j=1}^{T} \frac{\left(RD_{i,j} - MRD_i\right)^2}{T-1}} \quad \text{Eq. 3. 3}$$

The value of *SDRD* serves as a measure of the robustness of the temporal stability analysis. A measurement location with a *MRD* close to zero provides a good direct estimate of the areal average of soil water content throughout time, whereas a small *SDRD* indicates that the *MRD* was relatively constant in time. Cosh et al (2006) proposed that a location can be defined as temporally stable when it shows a *SDRD* less than 30 %.

Spatial variation in soil water content pattern can be characterized by the standard deviation of the *MRDs* (*SDMRD*):

$$SDMRD = \sqrt{\sum_{i=1}^{N} \frac{\left(MRD_i - \frac{1}{N}\sum_{i=1}^{N} MRD_i\right)^2}{(N-1)}} \quad \text{Eq. 3. 4}$$

where $\frac{1}{N}\sum_{i=1}^{N} MRD_i$ is the mean *MRD*.

Using the methods outlined above, we also applied the temporal stability analysis to the saturation degree of soil water content. The saturation degree (*SD*) is defined in Eq. 3. 5:

$$SD = \frac{\theta}{\theta_s} \quad \text{Eq. 3. 5}$$

We assume that the highest measured soil water content at each location corresponds to the saturated water content (θ_s). This is reasonable given the long measurement time and the wet winter seasons in Rollesbroich catchment characterized by high precipitation and low evapotranspiration rates (see Figure 3. 2).

3.3.4 Hydrus-1D simulation

We used a numerical solution of the one-dimensional Richards equation as implemented in the HYDRUS 1-D software (Simunek and van Genuchten, 2008; Simunek et al., 2008b) to simulate soil water dynamics for a 1D flow domain with a vertical length of 100 cm:

$$\frac{\partial \theta}{\partial t} = \frac{\partial}{\partial z}(K(h)(\frac{\partial h}{\partial z} + 1)) \quad \text{Eq. 3. 6}$$

where K (cm day^{-1}) is the soil hydraulic conductivity, h (cm) is the pressure head, t (day) is time, and z (cm) is the vertical coordinate. The soil hydraulic conductivity is described by the van Genuchten-Mualem (VGM) model (van Genuchten, 1980):

$$K(h) = K_s S_e{}^{0.5}\left[1 - \left(1 - S_e{}^{1/m}\right)^m\right]^2 \quad \text{Eq. 3. 7}$$

$$\mathrm{S}_e(\mathrm{h}) = \begin{cases} \frac{\theta - \theta_r}{\theta_s - \theta_r} = (1 + |\alpha h|^n)^{-m}, & \text{for h} \le 0 \\ 1 \quad , & \text{for h} > 0 \end{cases} \quad \text{Eq. 3. 8}$$

where K_s is the saturated soil hydraulic conductivity (cm day^{-1}), $S_e(h)$ is the effective saturation, θ_r and θ_s (cm^{3}cm^{-3}) are the residual and saturated soil water content, α (cm^{-1}), n and m=1-1/n (dimensionless) are empirical shape parameters for fitting the soil water retention function.

The simulation period was from 1st January 2011 to 1st March 2013. Since soil water content is generally high during the winter season in the Rollesbroich catchment, the initial soil profile for HYDRUS 1D was set to be saturated. We tested different spin-up periods and found that a 4-month period with actual meteorological data was sufficient long to prevent the model results being affected by the initial conditions. The reference potential evapotranspiration (ET_0) was computed by the Penman-Monteith equation using global radiation, wind speed, relative humidity and air temperature (Jensen et al., 1997). These

variables were obtained from a nearby micrometeorological station. Potential evaporation (E) and transpiration (T) were separated based on the leaf area index (LAI) (Simunek et al., 2008a):

$$T = ET_0(1 - e^{-k*LAI}) \quad \text{Eq. 3. 9}$$

$$E = ET_0 e^{-k*LAI} \quad \text{Eq. 3. 10}$$

where k is a parameter (-) that governs the radiation extinction of the canopy, which depends on the sun angle, the distribution of plants, and the arrangement of leaves. Here, we use k = 0.49 as a representative value for grassland (Simunek et al., 2008a). Time series of LAI were derived from RapidEye images using the $NDVI$ approach (Myneni et al., 1997), detailed information about the procedure can be found in Ali et al (2013). The agricultural management of the different fields in the Rollesbroich catchment is very similar. Heterogeneity of the grass cover is mainly caused by different mowing times, which typically vary only by a few days. Therefore, we assume that the grass cover is homogeneous on the long-term in our catchment.

Daily data on precipitation, evaporation, and transpiration were used to set the upper boundary condition for the HYDRUS-1D simulation. The lower boundary was set to be a seepage face since the relatively thin soil layer overlays a fractured solid bedrock containing water conducting fissures. The root density was set to decrease linearly from a maximum value at the soil surface to zero at 50 cm depth, and root water uptake was computed by the Feddes approach (Feddes et al., 1976) implemented in HYDRUS-1D.

3.3.5 Estimation of soil hydraulic parameters using inverse modeling

Inverse modeling was used to estimate the effective VGM parameters from measured time series of soil water content at 5, 20, and 50 cm depth. For this, we coupled the SCE-UA algorithm of Duan et al. (1992) to HYDRUS-1D. The objective function that was minimized by the SCE-UA algorithm was computed as following:

$$OF = \sum_{j=1}^{T} (\tilde{y}_j - y_j(x))^2 \qquad \text{Eq. 11}$$

where the vector $\tilde{\mathbf{y}} = [\tilde{\mathbf{y}}_{\mathbf{5cm}}, \tilde{\mathbf{y}}_{\mathbf{20cm}}, \tilde{\mathbf{y}}_{\mathbf{50}\boldsymbol{cm}}]$ contains daily observations of soil water content, and the vector $\mathbf{y} = [\mathbf{y}_{\mathbf{5cm}}, \mathbf{y}_{\mathbf{20cm}}, \mathbf{y}_{\mathbf{50}\boldsymbol{cm}}]$ contains daily HYDRUS-1D predictions of soil water content, $\boldsymbol{x}=(\theta_r, \alpha, n, K_s)$ is the vector containing the VGM parameters, j is the measurement time and T is the total number of measurements. θ_s is not part of vector $\boldsymbol{x}$ since it was estimated from the highest measured water content. This inverse modeling approach was used to estimate hydraulic parameters for each of the 41 SoilNet locations show in Figure 3. 1.

The parameter searching space of SCE-UA was constrained using a multivariate normal distribution of the VGM parameters that was derived using Rosetta (Schaap et al., 2001) from measured sand, silt, clay content, and dry bulk density for 273 soil samples taken in three depths (0-10 cm, 10-20 cm, and 20-40 cm) in the Rollesbroich catchment (Figure 3. 1). The mean, standard deviation, and correlation matrix that summarize this multivariate normal distribution of VGM parameters are shown in Table 3. 2. In order to consider this multivariate normal distribution in the inverse modeling, the SCE-UA algorithm was modified in two steps. First, the initial set of random parameters was drawn from the multivariate normal distribution summarized in Table 3. 2. Second, it was evaluated whether the intermediate parameter sets proposed by SCE-UA fall within the multivariate normal

distribution. This was achieved by using the Mahalanobis distance (Farber and Kadmon, 2003):

$$D = \sqrt{(Y-\mu)' S^{-1} (Y-\mu)} \quad \text{Eq. 12}$$

where D is the Mahalanobis distance, Y is a vector with the proposed parameter set, μ is a vector with the mean of the multivariate normal distribution (Table 3. 2), and S is the associated covariance matrix. Farber and Kadmon (2003) have shown that the Mahalanobis distance (D) of random draws from a multivariate normal distribution follows a χ^2 distribution with x-1 degrees of freedom (x is the number of variables). In our case, this means that parameter sets with Mahalanobis distances larger than 13.28 are unlikely to be associated with a draw from the multivariate normal distribution (p=0.01). Therefore, intermediate parameter sets with a Mahalanobis distances larger than 13.28 were discarded in SCE-UA and replaced with a new parameter set that was randomly drawn from the multivariate normal distribution summarized in Table 3. 2. It is important to realize that SCE works with a population of parameter sets and many different proposal points are generated. Therefore, the overall convergence of SCE is not jeopardized by our treatment of proposal points outside of the specified multivariate normal distribution.

Table 3. 2. Mean values, standard deviations, and correlation coefficients of soil hydraulic parameters predicted by Rosetta using soil texture and bulk density from Rollesbroich catchment.

				Correlation coefficients			
parameter	unit	mean	std	$\log_{10}(K_s)$	θ_r	$\log_{10}(\alpha)$	n
$\log_{10}(K_s)$	cm day^{-1}	1.60	0.52	1			
θ_r	cm^3 cm^{-3}	0.07	0.01	0.89	1		
$\log_{10}(\alpha)$	cm^{-1}	-2.26	0.11	-0.63	-0.63	1	
n	-	1.65	0.08	0.62	0.60	-0.98	1

3.4. Results and discussion

3.4.1 Time series data of weather conditions and soil water content

Time series of precipitation, evapotranspiration, mean and standard deviation of soil water content are presented in Figure 3. 2. During the observation period from 1st May 2011 to 1st March 2013, total precipitation and potential evapotranspiration were 228.2 cm and 121.8 cm, respectively. Overall, soil water content at 5 cm and 20 cm depth depended strongly on precipitation events. Especially in the top soil, a steep rise of soil water content can be observed after rainfall events, which was followed by a slow recession during periods without precipitation. For all depths, the lowest soil water contents were observed during May 2011, because precipitation was low (2.9 cm) and evapotranspiration was relatively high (9.5 cm). The soil water content was lowest near the surface in this time period, most likely because root water uptake is generally larger in topsoil than in subsoil, especially in the case of grassland which typically shows a very high root density near the surface. In December 2011, precipitation was relatively high (20.7 cm) and evapotranspiration was low (0.5 cm) leading to nearly saturated soils. Since electromagnetic sensors cannot determine soil water content in partly frozen soils, we excluded the period from 10th January 2012 until 26th February 2012 from our analysis.

Figure 3. 2. Daily time series of precipitation, potential evapotranspiration (1st January 2011 - 1st March 2013), spatial mean and standard deviation (std) of soil water content (SWC) at 5, 20 and 50 cm depths (1st May 2011 - 1st March 2013), respectively.

Spatial variability of measured soil water content was higher at 50 cm depth compared to 5 cm and 20 cm depths as indicated by the temporal dynamics of the standard deviation of soil water content presented in Figure 3. 2 (bottom panel). We attribute this to the pedological situation (shallow soil above consolidated bedrock) in which the highly variable stone content

in the subsoil leads to considerable spatial variability of soil water content at 50 cm depth. A similar increase in standard deviation with depth has also been observed in the nearby forest test site in Wüstebach with a similar pedological situation (Rosenbaum et al., 2012). In contrast, the standard deviations at 5 cm and 20 cm depth are much smaller in Rollesbroich than those observed in the Wüstebach test site. One reason for the lower spatial soil water content variability at the Rollesbroich test site is the fact that the topsoil has become more homogeneous through former agricultural land use. In addition, the homogenous grass cover and the relatively flat slopes of the Rollesbroich site also lead to lower spatial variability in soil water content as compared to the Wüstebach site with its locally variable vegetation coverage and steeper slopes. Yet another reason is that the spatial variability of infiltration was larger in the Wüstebach test site because canopy interception and associated leaf drip lead to heterogeneous throughfall patterns in forests.

3.4.2 Observed *MRD* and *SDRD*

Figure 3. 3 shows the ranked *MRDs* and their variability for the 41 SoilNet locations. Similarly, the *MRDs* and their variability for saturation degree are shown in Figure 3. 4. All *SDRDs* values were smaller than 30 %, indicating temporal stability for all locations (Cosh et al., 2006). The *SDRDs* were lower at 20 and 50 cm than at 5 cm, indicating that the subsoil was more temporally stable than the topsoil. This result corresponds well with previous studies (Guber et al., 2008; Hu et al., 2010b; Starks et al., 2006). This decreasing *SDRD* with increasing soil depth was attributed to the decreasing impact of root water uptake of crops with depth, whereas pedogenetically derived variations in the deeper layers preserved a rather stable pattern of spatial variation through time. The range of *MRDs* of soil water content increased with depth, i.e. 0.65, 0.54 and 0.84 at depths of 5, 20, and 50 cm, respectively.

These results are consistent with the standard deviation of soil water content (Figure 3. 2), which already showed that the top soil is more homogeneous than the subsoil. In the Rollesbroich catchment, spatially variable soil layering probably leads to pronounced differences in soil water content at the same depth in different locations. An increase of *SDMRD* (i.e. 0.12, 0.12, and 0.22 at 5, 20, and 50 cm, respectively) with depth was observed in our study. Similarly, other studies found that the temporal stability of soil water storage was less pronounced in shallow soil layers (Cassel et al., 2000; Gao and Shao, 2012; Kamgar et al., 1993; Martinez et al., 2010).

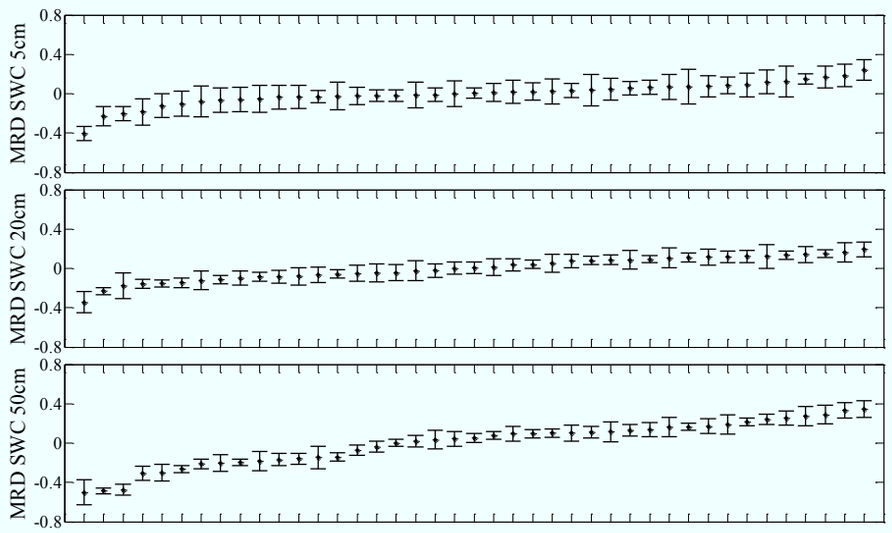

Figure 3. 3. Ranked *MRDs* (dots) and *SDRDs* (vertical bars) of soil water contents in Rollesbroich at 5, 20 and 50 cm depths, respectively.

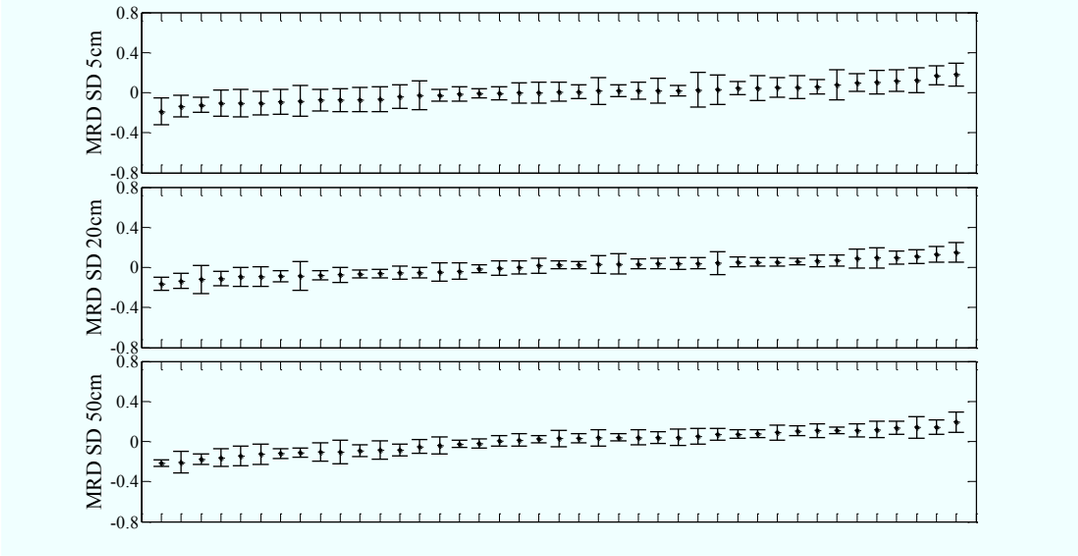

Figure 3. 4. Ranked *MRDs* (dots) and *SDRDs* (vertical bars) of saturation degrees in Rollesbroich at 5, 20 and 50 cm depths, respectively.

The *MRDs* of saturation degree showed the same tendency as the *MRDs* of soil water content, but the ranges of *MRDs* of saturation degree were less variable for different depths (0.31, 0.37 and 0.41 at 5, 20, and 50 cm, respectively). The corresponding *SDMRD* of saturation degree were 0.08, 0.08 and 0.11 at 5, 20, and 50 cm, respectively. This indicates that the variability of saturation degree was lower in general and as a function of depth than that of soil water content. Moderate correlations were observed between the ranked *MRDs* of soil water content and saturation degree at 5, 20, and 50 cm depth with correlation coefficients of 0.81, 0.66, and 0.72, respectively.

3.4.3 Evaluation of estimated hydraulic parameters

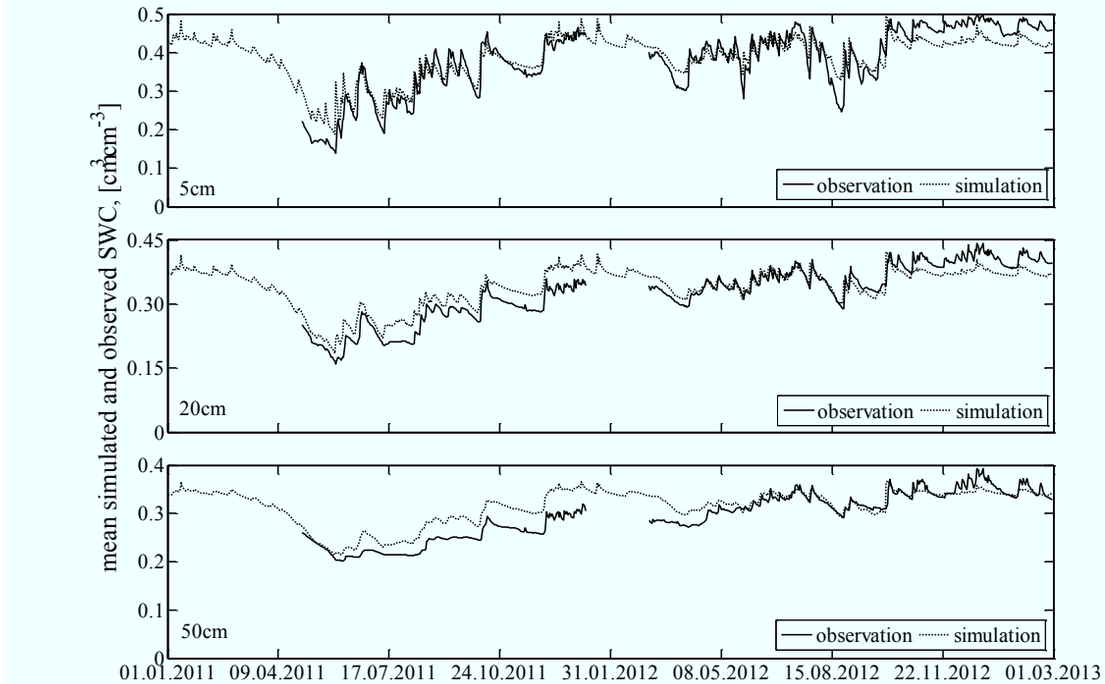

Figure 3. 5. Observed mean time series soil water contents of the 41 locations (solid lines); mean of inverse simulated soil water content (dashed lines) at 5, 20 and 50 cm depths, respectively.

Modelled soil water content obtained using inversely estimated hydraulic parameters were in good agreement with the observed dynamics of soil water content. The mean simulated soil water content matched well with the mean observed soil water content (Figure 3. 5) as indicated by the RMSE of 0.037, 0.029, and 0.027 cm^3cm^{-3} and the R^2 of 0.922, 0.921, and 0.894 for 5, 20, and 50 cm, respectively. When considering simulated and measured soil water content at all 41 locations, the RMSE was never higher than 0.08 cm^3cm^{-3} and often

much better, and the R^2 was always larger than 0.75 (Figure 3. 6). The pairwise scatter plots of inversely estimated VGM parameters are shown in Figure 3. 7. The ellipses represent the multivariate normal distribution used to constrain the parameter search. The Mahalanobis distance of all inversely estimated VGM parameter sets was smaller than 13.28 as prescribed.

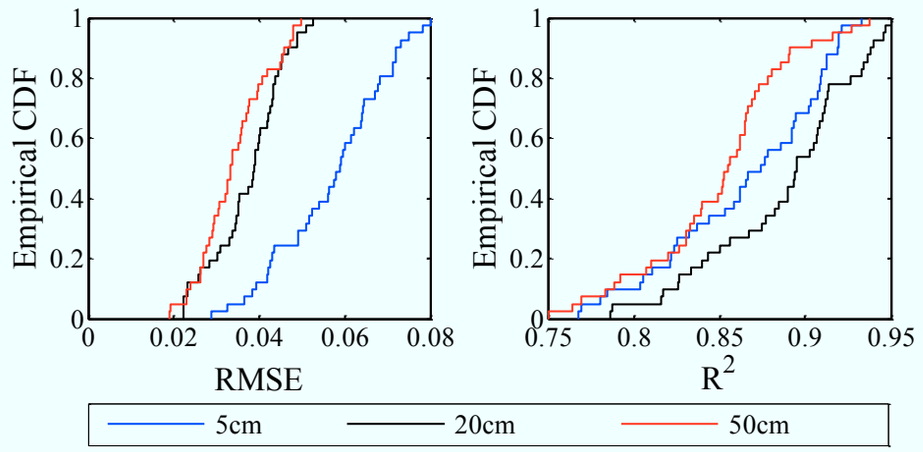

Figure 3. 6. Empirical cumulative probability distributions of RMSE and R^2 of inverse simulated and observed soil water content for three soil depths.

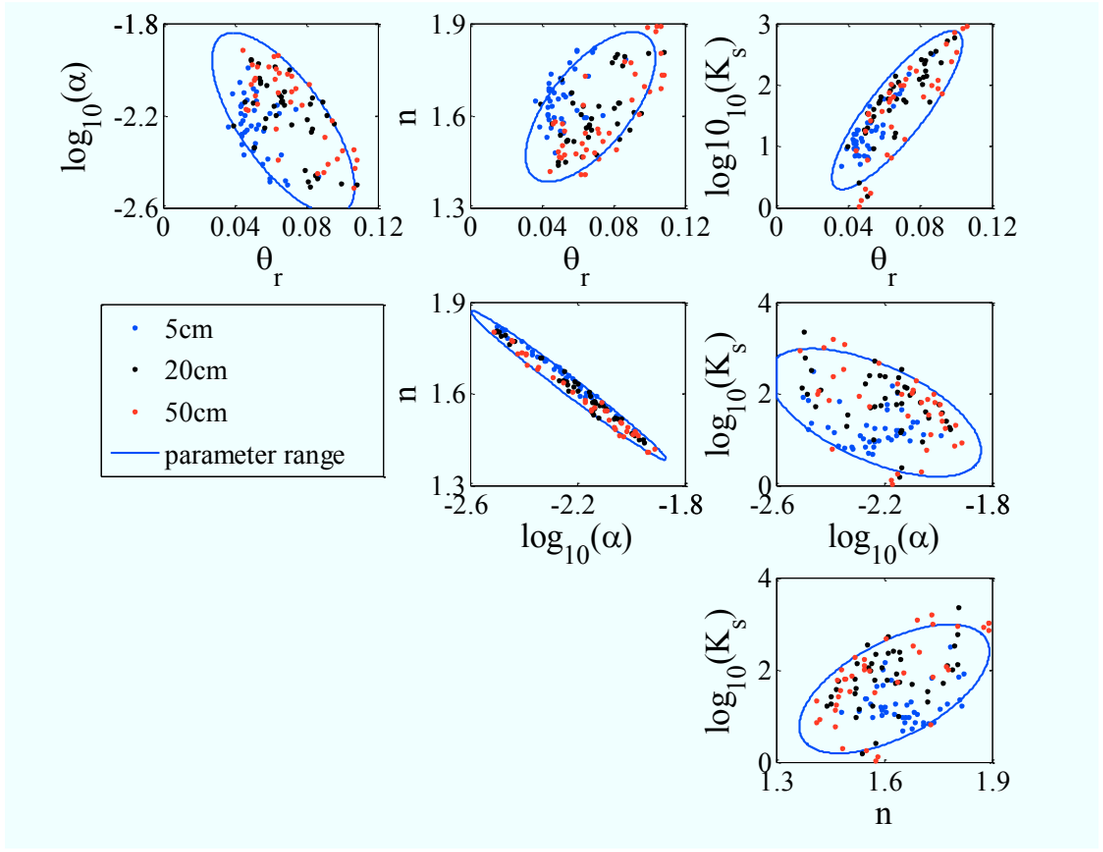

Figure 3. 7. Pairwise scatter plots of soil hydraulic parameters estimated by inverse. The blue ellipses approximately indicate parameter range of the multivariate distributions derived from the 273 soil samples (Figure 3. 1) from our field. The colored dots represent the estimated soil hydraulic parameters at 5 cm (blue), 20 cm (black), and 50 cm (red) depths for our 41 SoilNet locations.

3.4.4 Relationships between soil hydraulic properties and *MRDs*

The *MRDs* of soil water content showed a strong positive correlation with θ_s for all depths, indicating that locations with a high θ_s are associated with higher soil water contents and

locations with low θ_s associated with lower soil water contents (Table 3. 3 and Figure 3. 8). Obviously, this reflects the direct link between θ_s and soil water storage capacity. Moreover, the *MRDs* of soil water content were positively correlated with the α parameter, and negatively correlated with the n parameter. That is because larger α parameters and smaller n parameters typically are associated with poorly draining soils, which consequently have higher soil water content. In agreement with Martinez et al. (2013), we also found a negative correlation between *MRDs* of soil water content and K_s. However, our correlation is much weaker. Correlations between *MRDs* of saturation degree and soil VGM parameters are presented in Table 3. 3 and Figure 3. 9. The obtained correlations between *MRDs* of saturation degree and VGM parameters were similar to the correlations obtained for soil water content (Figure 3. 8). However, the relationship between *MRDs* of saturation degree and θ_s was less pronounced, whereas the *MRDs* of saturation degree was correlated more strongly with the α and n parameters that determine the shape of the VGM model.

Table 3. 3. Correlation coefficients between the *MRDs* of soil water content and saturation degree and VGM parameters obtained using inverse modeling.

	5cm	20cm	50cm		5cm	20cm	50cm
MRD(θ)- θ_r	0.03	0.42*	0.52*	*MRD(SD)- θ_r*	0.06	0.20	0.47*
MRD(θ)- θ_s	0.71*	0.76*	0.93*	*MRD(SD)- θ_s*	0.16	0.14	0.69*
MRD(θ)- α	-0.45*	-0.34*	-0.56*	*MRD(SD)- α*	-0.47*	-0.43*	-0.61*
MRD(θ)- n	0.46*	0.26*	0.51*	*MRD(SD)- n*	0.47*	0.34*	0.56*
MRD(θ)- K_s	-0.24	-0.18	-0.17	*MRD(SD)- K_s*	-0.16	-0.10	-0.13

*Significant at $p<0.05$.

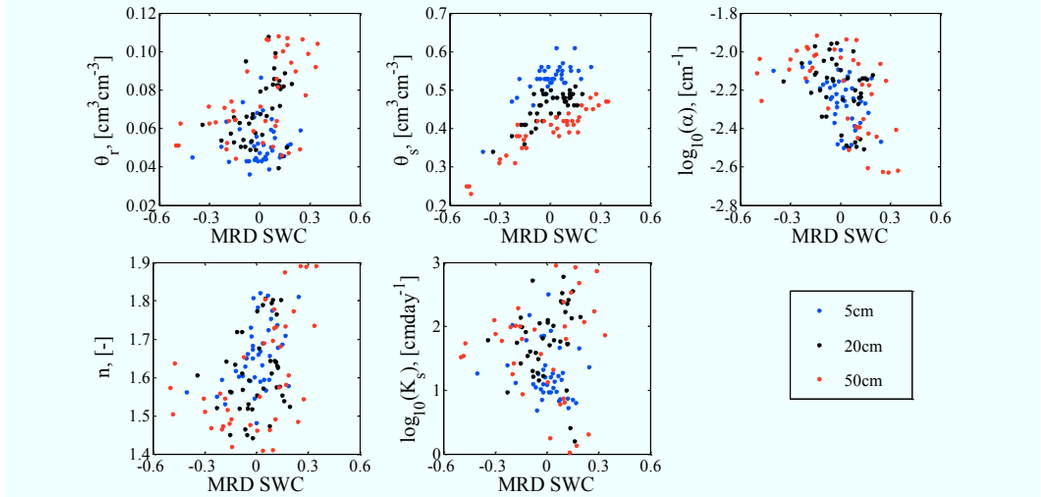

Figure 3. 8. Correlation between *MRDs* of soil water content and soil hydraulic parameters (θ_r, θ_s, $\log_{10}(\alpha)$, n, and $\log_{10}(K_s)$) at 5, 20 and 50 cm depths, respectively.

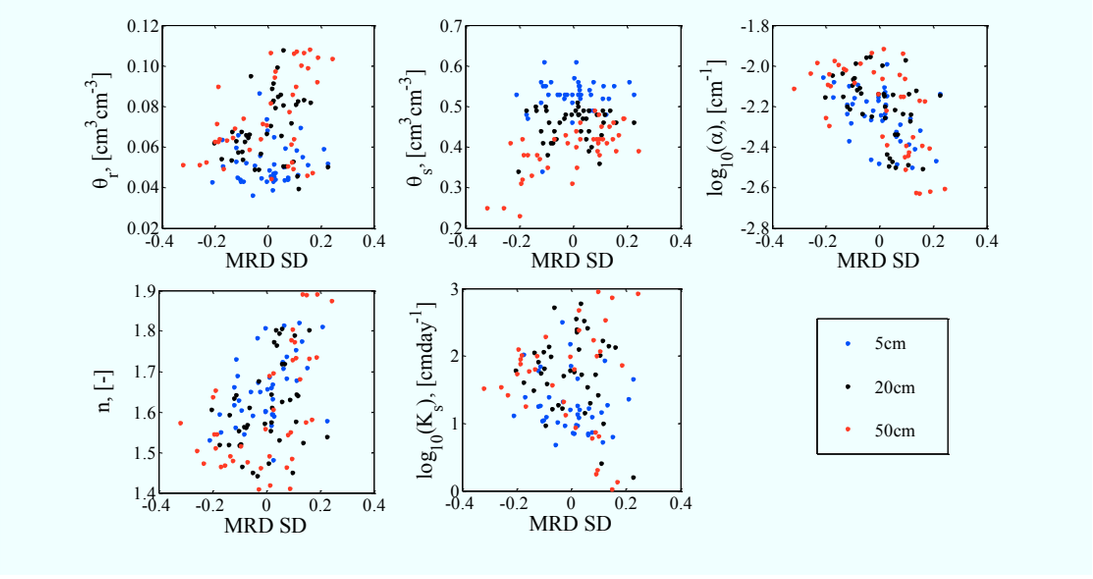

Figure 3. 9. Correlation between *MRDs* of saturation degree and soil hydraulic parameters parameters (θ_r, θ_s, $\log_{10}(\alpha)$, n, and $\log_{10}(K_s)$) at 5, 20 and 50 cm depths, respectively.

The analysis presented here was inspired by Martinez et al. (2013) who found that *MRDs* of soil water content and $\log_{10}(K_s)$ were strongly negatively related in a study using numerical simulations. In another synthetic study of Wang (2014), it was found that the *MRDs* of soil water content correlates with θ_r and with n for fixed θ_r under semi-arid climate conditions. However, our findings based on experimental data suggest that the results from synthetic studies cannot be transferred directly to real world conditions. In contrast, we found that also other VGM parameters are more or less correlated with the *MRDs* of soil water content and saturation degree. Our results indicate that θ_s and the parameters describing the shape of the water retention and hydraulic conductivity functions are more important than the value of K_s. This finding is also supported by the study of Vereecken et al. (2007), who demonstrated that the pore size distribution parameter n has the strongest effect on the spatial variability of soil water content. However, it should be kept in mind that this study is restricted to the silt loam textural class, and that other texture classes might lead to different relationships between *MRD* and soil hydraulic properties.

3.5. Conclusions

We analyzed the temporal stability of in-situ soil water content observed by a wireless sensor network at three depths at the TERENO test site Rollesbroich. Temporally stable characteristics were found both in soil water content and saturation degree. We suggest that both soil water content and saturation degree should be considered in future temporal stability studies when the porosity is known to vary considerably, as it is one of the most important factors that affect water storage and infiltration characteristics in soil.

Our inversely estimated VGM parameters were constrained by a multivariate normal distribution derived using pedotransfer functions from measured sand, silt, and clay content in addition to bulk density. Modelled soil water content agreed well with the observed soil water content dynamics in all soil depths. The corresponding RMSE was always smaller than 0.08 cm^3cm^{-3} and the R^2 was always larger than 0.75 for the 41 SoilNet locations.

The spatial variability of soil water content as expressed by the *MRDs* of soil water content and saturation degree were correlated with the spatial variation in hydraulic parameters in our catchment. We found strong positive correlations between *MRDs* of soil water content and the θ_s and n parameters of the VGM model for all three soil depths. Moreover, we found negative correlations between *MRDs* of soil water content and the soil hydraulic properties α and K_s. In addition, the *MRDs* of saturation are only strongly correlated with the soil hydraulic properties α and n parameter that determine the shape of the VGM model.

In this study, we only analyzed soil water content dynamics and soil hydraulic parameters of silt loam soils. Future studies should extent our analysis to other soil textural classes and climate conditions in order to further explore the limitations and potentials of this approach. Furthermore, the *MRD* of soil water content and saturation degree is known to be determined by a number of physiographic factors that affect the vertical and lateral redistribution of soil water. Although factors that influence vertical redistribution are understood relatively well, the factors that cause lateral redistribution are not yet well quantified. In future studies, the effect of topography on the *MRD* of soil water content and saturation degree should be considered in addition to the heterogeneity of soil hydraulic properties.

4 Predicting sub-grid variability of soil water content from basic soil information

This chapter has been published as: W. Qu, H. R. Bogena, J. A. Huisman, J. Vanderborght, M. Schuh, E. Priesack, H. Vereecken. Predicting subgrid variability of soil water content from basic soil information. Geophysical Research Letters, 2015, 42 (3). dio: 10.1002/2014GL062496

4.1 Objectives

In this chapter, we first derive a closed-form expression for the $\sigma_\theta(<\theta>)$ relationship using stochastic analysis of 1D unsaturated gravitational flow based on the VGM model. A sensitivity analysis is presented to identify the effect of VGM parameters on the $\sigma_\theta(<\theta>)$ relationship. Next, the predictions of the novel closed-form expression for $\sigma_\theta(<\theta>)$ are evaluated using eight datasets of observed $\sigma_\theta(<\theta>)$ relationships obtained at test sites with a wide range of using VGM parameters as determined from pedotransfer functions that rely on available basic soil data. Finally, we inversely estimate the variability of hydraulic properties from observed $\sigma_\theta(<\theta>)$ data.

4.2 Introduction

Sub-grid variability of soil water content is known to be an important control on the magnitude of land-surface energy fluxes (Bonan et al., 1993; Hu and Islam, 1998; Ronda et al., 2002) and hydrologic fluxes such as runoff (Arora, 2001; Gedney and Cox, 2003). An adequate representation of small-scale soil water content variability in large-scale hydrologic, weather, and climate models requires information on the relationship between sub-grid soil water content variability as expressed by the standard deviation (σ_θ) and mean soil water content ($<\theta>$) (Teuling and Troch, 2005). Improved ability to predict this relationship from basic soil information may contribute to a more efficient representation of soil water content variability in large-scale models, and consequently in more accurate predictions of land surface processes (Vereecken et al., 2008).

Reynolds (1970) was the first to derive relationships between measured σ_θ and $<\theta>$ as well as other controlling factors, i.e. insolation and rainfall. Since then, numerous field studies have been carried out to identify factors that control the $\sigma_\theta(<\theta>)$ relationship. Several studies found that σ_θ increased with increasing $<\theta>$ (Famiglietti et al., 1998; Oldak et al., 2002; Takagi and Lin, 2011), whereas Famiglietti et al. (1999), Hupet and Vanclooster (2002) and Western et al. (2004) observed the opposite behavior. Moreover, a convex parabolic shape of the $\sigma_\theta(<\theta>)$ curve with a distinct maximum in the medium range of $<\theta>$ has been observed (Choi and Jacobs, 2007; Garcia-Estringana et al., 2013; Rosenbaum et al., 2012).

Widely used methods to investigate the controls on the $\sigma_\theta(<\theta>)$ relationship include virtual simulation experiments (Albertson and Montaldo, 2003) and stochastic analysis (Zhang et al., 1998). Virtual experiments by Albertson and Montaldo (2003) and Teuling and Troch (2005) showed that the covariances between the soil water state and land surface fluxes (i.e. infiltration, drainage, evapotranspiration, and horizontal redistribution) act to generate or destroy spatial variability of soil water content through time. Zhang et al. (1998) used stochastic analysis to derive an analytical expression that describes the $\sigma_\theta(<\theta>)$ relationship for 1D unsaturated gravitational flow using the Brooks-Corey and the Gardner-Russo models for water retention and hydraulic conductivity. Following Zhang et al. (1998), Vereecken et al. (2007) demonstrated that the shape of $\sigma_\theta(<\theta>)$ can be explained to a large extent by the spatial variance of soil hydraulic properties, although a direct evaluation using measured $\sigma_\theta(<\theta>)$ data and information on the spatial variation of hydraulic properties has not been presented yet. These previous stochastic studies relied on the use of Brooks-Corey or Gardner-Russo model because of their mathematical tractability. However, it is generally

accepted that the van Genuchten-Mualem (VGM) model (van Genuchten, 1980) is better suited to describe experimental soil water retention data.

4.3 Model development

The stochastic approach of *Zhang et al.* (1998) to describe 1D unsaturated gravitational flow in a heterogeneous flow domain was used to derive a closed-form expression that describes $\sigma_\theta(<\theta>)$ as a function of the mean and standard deviation of the soil hydraulic parameters of the VGM model. The starting point of this derivation is the steady-state simplification of the Richards equation:

$$\frac{\partial}{\partial x}\left[K(h)\left(\frac{\partial h}{\partial x}+1\right)\right]=0 \qquad \text{Eq. 4. 1}$$

where K(h) (cm d^{-1}) is the unsaturated soil hydraulic conductivity, h (cm) is the pressure head, and x (cm) is the vertical coordinate. The VGM model to describe the soil water retention and hydraulic conductivity curves is given by:

$$S_e(h)=\frac{\theta-\theta_r}{\theta_s-\theta_r}=\frac{1}{(1+(\alpha|h|)^n)^m}, \qquad h<0$$
$$m=1-\frac{1}{n} \qquad \text{Eq. 4. 2}$$

$$K(S_e)=K_s {S_e}^{0.5}\left[1-\left(1-{S_e}^{1/m}\right)^m\right]^2, \qquad h<0 \qquad \text{Eq. 4. 3}$$

For mathematical convenience, the log-transformed saturated hydraulic conductivity ($\ln(K_s)$) is used in our study. In our analysis, residual soil water content (θ_r) is assumed to be constant. All other variables and parameters, i.e. pressure head (h), soil water content (θ), hydraulic conductivity (K), effective saturation degree (S_e), saturated soil water content (θ_s), saturated hydraulic conductivity (K_s), and the fitting parameters α and n of the VGM model are considered to be realizations of a second-order stationary stochastic process, which can be decomposed into their mean and perturbations. Following the stochastic analysis of *Zhang et*

al. (1998), we derived the expression of the mean and covariance of soil water content for 1D unsaturated gravitational flow in an infinitely long vertical profile using first-order Taylor expansions. In particular, we related the covariance of soil water content and pressure head to the variance and covariance of VGM parameters (K_s, θ_s, α, and n) using Eq. 4. (1) to (3). For a detailed derivation we refer to the Supplementary Information. The closed-form expression for $\sigma_\theta(<h>)$ is:

$$\sigma_\theta^2 = {b_0}^2\left\{{b_1}^2\sigma_\alpha^2 + {b_2}^2\left[\frac{\sigma_f^2\rho_f}{(1+a_2\rho_f)a_2} + \frac{a_1\sigma_\alpha^2\rho_\alpha}{(1+a_2\rho_\alpha)a_2} + \frac{a_3\sigma_n^2\rho_n}{(1+a_2\rho_n)a_2}\right] + {b_3}^2\sigma_n^2 + {b_4}^2\sigma_{\theta_s}^2 + 2b_1b_2\left(-\frac{a_1\sigma_\alpha^2\rho_\alpha}{1+a_2\rho_\alpha}\right) + 2b_2b_3\left(-\frac{a_3\sigma_n^2\rho_n}{1+a_2\rho_n}\right)\right\} \quad \text{Eq. 4. 4}$$

where $b_0 = (\langle\theta_s\rangle - \theta_r)\left(\frac{\langle\alpha\rangle\langle h\rangle}{[1+(\langle\alpha\rangle\langle h\rangle)^{\langle n\rangle}](\langle\alpha\rangle\langle h\rangle)^{\langle n\rangle}\langle n\rangle}\right)$;

$b_1 = \frac{\langle n\rangle(\langle\alpha\rangle\langle h\rangle)^{\langle n\rangle}+1-\langle n\rangle}{\langle\alpha\rangle} - \frac{[\langle n\rangle(\langle\alpha\rangle\langle h\rangle)^{\langle n\rangle}+1](\langle\alpha\rangle\langle h\rangle)^{\langle n\rangle}}{1+(\langle\alpha\rangle\langle h\rangle)^{\langle n\rangle}}\frac{\langle n\rangle}{\langle\alpha\rangle}$;

$b_2 = \frac{\langle n\rangle(\langle\alpha\rangle\langle h\rangle)^{\langle n\rangle}+1-\langle n\rangle}{\langle h\rangle} - \frac{[\langle n\rangle(\langle\alpha\rangle\langle h\rangle)^{\langle n\rangle}+1](\langle\alpha\rangle\langle h\rangle)^{\langle n\rangle}}{1+(\langle\alpha\rangle\langle h\rangle)^{\langle n\rangle}}\frac{\langle n\rangle}{\langle h\rangle}$;

$b_3 = -\frac{1}{\langle n\rangle} - ln(\langle\alpha\rangle\langle h\rangle) - \frac{[\langle n\rangle(\langle\alpha\rangle\langle h\rangle)^{\langle n\rangle}+1](\langle\alpha\rangle\langle h\rangle)^{\langle n\rangle}}{1+(\langle\alpha\rangle\langle h\rangle)^{\langle n\rangle}}ln(\langle\alpha\rangle\langle h\rangle)$;

$b_4 = \langle n\rangle(\langle\alpha\rangle\langle h\rangle)^{\langle n\rangle} + 1$;

$a_1 = \frac{(\frac{5}{2}-\frac{1}{2\langle n\rangle})(\langle\alpha\rangle\langle h\rangle)^{\langle n\rangle}}{1+(\langle\alpha\rangle\langle h\rangle)^{\langle n\rangle}}\frac{\langle n\rangle}{\langle\alpha\rangle}$;

$a_2 = \frac{(\frac{5}{2}-\frac{1}{2\langle n\rangle})(\langle\alpha\rangle\langle h\rangle)^{\langle n\rangle}}{1+(\langle\alpha\rangle\langle h\rangle)^{\langle n\rangle}}\frac{\langle n\rangle}{\langle h\rangle}$;

$a_3 = \frac{(\frac{5}{2}-\frac{1}{2\langle n\rangle})(\langle\alpha\rangle\langle h\rangle)^{\langle n\rangle}}{1+(\langle\alpha\rangle\langle h\rangle)^{\langle n\rangle}}ln(\langle\alpha\rangle\langle h\rangle) + \frac{ln[1+(\langle\alpha\rangle\langle h\rangle)^{\langle n\rangle}]}{2\langle n\rangle^2} - \frac{2}{\langle n\rangle^2-\langle n\rangle}$;

$f = ln(K_s)$.

This novel closed-form expression describes $\sigma_\theta(<h>)$ as a function of the mean (i.e. $<\theta_s>$, $<\ln(K_s)>$, $<\alpha>$, and $<n>$), the standard deviation (i.e. $\sigma(\theta_s)$, $\sigma(\ln(K_s))$, $\sigma(\alpha)$, and $\sigma(n)$), and the vertical correlation length (i.e. $\rho_{\ln(Ks)}$, ρ_α, and ρ_n) of the VGM model parameters. Using the following equation, <h> can be transformed into <θ>:

$$\langle\theta\rangle = (\langle\theta_s\rangle - \theta_r)\left(\frac{\langle\alpha\rangle\langle h\rangle}{1+(\langle\alpha\rangle\langle h\rangle)^{\langle n\rangle}}\right)\left(\frac{\langle n\rangle(\langle\alpha\rangle\langle h\rangle)^{\langle n\rangle}+1}{\langle n\rangle(\langle\alpha\rangle\langle h\rangle)^{\langle n\rangle}}\right)+\theta_r \qquad \text{Eq. 4. 5}$$

In order to assess the importance of the pressure head fluctuations that result from flow in the heterogeneous soil profiles, we also calculated $\sigma_\theta(<\theta>)$ for h'=0 (i.e. assuming that the system has the same pressure head everywhere) in the Supplementary Information. It is important to realize that the obtained σ_θ represents variability along a deep vertical profile. Since soil water content is assumed to be an ergodic second-order stationary stochastic variable, σ_θ in vertical direction corresponds with σ_θ at a certain depth (i.e. spatial variability) if sampling points are sufficiently far from each other (i.e. sampling points are independent when separation is more than the horizontal correlation length of the soil properties). It should also be noted that the vertical water flux is assumed to be identical at every location so that the effect of lateral water redistribution and variability in surface fluxes is not considered.

4.4 Materials and Methods

4.4.1 Site descriptions

We used eight different datasets from five test sites to evaluate the ability of the closed-form expression (Eq. 4. 4) to describe observed $\sigma_\theta(<\theta>)$ data. Detailed information about the test sites are given in Table 4. 1. Three datasets were obtained using wireless sensor networks deployed at the TERENO test sites Rollesbroich, Wüstebach, and Scheyern (TERENO, 2012). For these three sites, hourly aggregated soil water content data measured at three

depths (5, 20, 50 cm for Rollesbroch and Wüstebach, and 10, 30, 50 cm for Scheyern) were used. In addition, we used datasets that originated from the Inner Mongolia Grassland Ecosystem Research Station (IMGERS, 1979). Here, water content of the top soil (0-6 cm) was measured in four experimental plots subjected to different grazing intensity, i.e. ungrazed since 1999 (ug99), ungrazed since 1979 (ug79), continuous grazing (cg), and heavy grazing (hg) (Schneider et al., 2008; Schneider et al., 2011). Finally, we used soil water content measurements (0-30 cm) from the Tarrawarra grassland test site (Australia) that were presented in detail by *Western and Grayson* (1998).

Table 4. 1. Characteristics of TERENO (Rollesbroich, Wüstebach, and Scheyern), IMGERS (ug 99, ug 79, cg, and hg), and Tarrawarra test sites.

	Rollesbroich	Wüstebach	Scheyern	IMGERS				Tarawarra
Latitude	50°37' N	50°30' N	45°30' N	43°38' N				37°39' S
Longitude	6°18' E	6° 19' E	11°45' E	116°42' E				145°26' E
Altitude (m a.s.l.)	515	605	470	1100				76
Average slope	1.6	3.6	5.7	1.9				1.1
Maximum slope	3.1	10.4	13.5	2.2				5.8
Land use	grassland	forest	grassland	grassland				grassland
Area (ha)	13.5	27.0	5.3	1.8				10.8
P_{AV} (cm)	103	111	83	35				82
T_{AV} (°C)	7.7	7.0	7.4	2.3				12.0
Start time	01.05 2011	01.07 2009	01.10 2012	2004				1995
End time	01.05 2012	01.07 2012	01.10 2013	2006				1996
Interval	15 min	15 min	15 min	6 days*				~monthly
Number of soil samples	273	34	54	ug99	ug79	cg	hg	34
				50	55	88	98	

* It was irregularly measured from June to September during the vegetation period.

*T_{AV}: annual average temperature, P_{AV}: annual cumulative precipitation.

4.4.2 Soil hydraulic parameter prediction

We used Rosetta (Schaap et al., 2001) to estimate the mean and standard deviation of VGM parameters (Table 4. 2) from measured sand, silt, clay content, and bulk density obtained from in-situ samples taken at all test sites (Figure 4. 1). Although these soil samples were not always taken at the exact position where soil water content was measured, we assume that the ensemble mean and standard deviation adequately represent each test site. As $\sigma_\theta(<\theta>)$ is typically not sensitive to the correlation length of $\ln(K_s)$, α, and n (Vereecken et al., 2007), we assumed a fixed correlation length of 10 cm in our study.

Table 4. 2. Mean and standard deviations of VGM parameters predicted by Rosetta for the TERENO, IMGERS, and Tarrawarra test sites.

		$<\theta_r>$	$<\theta_s>$	$<\alpha>$	$<n>$	$<\ln(K_s)>$	$\sigma(\theta_s)$	$\sigma(\alpha)$	$\sigma(n)$	$\sigma(\ln(K_s))$
		cm^3cm^{-3}		cm^{-1}	-	cmd^{-1}				
Rollesbroich	5 cm	0.06	0.54	0.006	1.65	3.70	0.05	0.002	0.08	1.21
	20 cm	0.06	0.44	0.005	1.67	3.50	0.04	0.001	0.04	0.70
	50 cm	0.05	0.38	0.007	1.58	2.52	0.04	0.003	0.10	0.70
Wüstebach	5 cm	0.12	0.77	0.010	1.40	4.14	0.08	0.003	0.16	0.70
	20 cm	0.10	0.70	0.010	1.40	4.17	0.10	0.003	0.16	0.70
	50 cm	0.10	0.66	0.010	1.40	4.14	0.20	0.003	0.16	0.70
Scheyern	5 cm	0.04	0.52	0.029	1.46	4.68	0.06	0.005	0.14	0.59
	20 cm	0.05	0.44	0.028	1.48	3.69	0.04	0.006	0.16	0.67
	50 cm	0.05	0.42	0.028	1.55	3.34	0.04	0.009	0.42	1.25
IMGERS	ug99	0.00	0.48	0.010	1.53	4.50	0.04	0.003	0.04	0.40
	ug79	0.00	0.52	0.010	1.51	5.06	0.04	0.003	0.04	0.35
	cg	0.00	0.45	0.010	1.50	3.96	0.02	0.003	0.03	0.19
	hg	0.00	0.44	0.013	1.50	4.00	0.04	0.003	0.03	0.20
Tarrawarra	30 cm	0.10	0.50	0.010	1.48	2.51	0.02	0.004	0.13	0.31

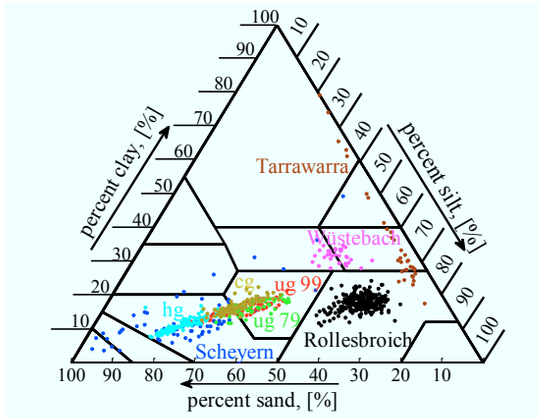

Figure 4. 1. USDA soil texture triangle displaying and soil texture distribution of samples taken from the three TERENO test sites (Rollesbroich, Wüstebach and Scheyern), the four IMGERS experimental test sites (ug99, ug79, cg, hg) and the Tarrawarra test site.

4.5 Results and Discussion

4.5.1 Sensitivity analysis of soil hydraulic parameters on $\sigma_\theta(<\theta>)$ relationship

Figure 4. 2 presents the sensitivity of the $\sigma_\theta(<\theta>)$ relationship to changes in the variability of $ln(K_s)$, θ_s, α, and n as expressed by the coefficient of variation (CV). The mean VGM parameters were taken from the Rollesbroich test site at 5 cm depth (Table 4. 2). This sensitivity analysis suggests that $\sigma_\theta(<\theta>)$ is most sensitive to the n parameter, followed by $ln(K_s)$, θ_s, and α, respectively. The results of the sensitivity analysis were similar for other soil textures, although the difference in sensitivity between the VGM parameters decreased with increasing sand content (results not shown). This finding is in good agreement with the results of Vereecken et al. (2007). They found that $\sigma_\theta(<\theta>)$ was most sensitive to the λ parameter of the Brooks-Corey model, which is related to pore size distribution just as the n parameter of the VGM model. It has to be noted that the derived curves for different levels of variability in the

n parameter show a second increase of σ_θ for $<\theta>$ larger than 0.5, which becomes more distinctive with increasing *CV*. Such an increase is typically not observed in actual $\sigma_\theta(<\theta>)$ data (e.g. Figure 4. 3). We attribute this model behavior to the first-order Taylor expansion approximation which was used to derive Eq. 4. . Consequently, the model results will be less reliable for high values of $<\theta>$, especially in the case that the *n* parameter is highly variable.

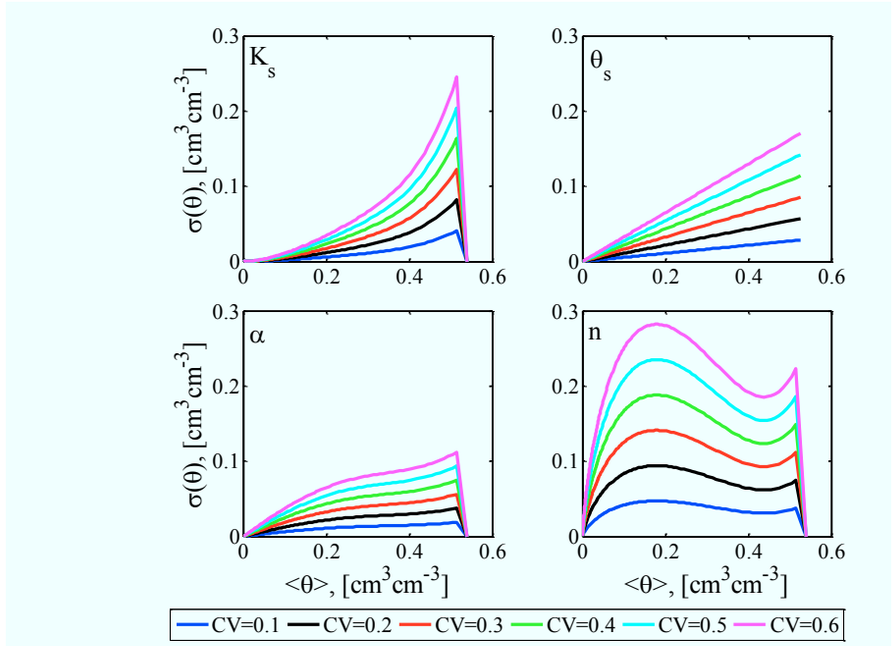

Figure 4. 2. The effect of variability of VGM parameters ($ln(K_s)$, θ_s, α, and n) on $\sigma_\theta(<\theta>)$ curve for silt loam soil using six different degrees of variability expressed as coefficient of variation.

4.5.2 Prediction of the $\sigma_\theta(<\theta>)$ relationship from soil texture data

Figure 4. 3 shows the measured and predicted $\sigma_\theta(<\theta>)$ relationships obtained using Eq. 4. 4 with the mean and standard deviation of the VGM parameters estimated from Rosetta (Table

4. 2). Although the test sites span a wide range of climatic conditions and soil textures, the general behavior of $\sigma_\theta(<\theta>)$ was well captured by the closed-form expression despite obvious simplifications in the model derivation. Predicted $\sigma_\theta(<\theta>)$ at the Wüstebach test site was generally high because of the high values for $<\theta_s>$ and $\sigma(n)$ (see Table 4. 2). A continuous increase of $\sigma_\theta(<\theta>)$ without an obvious maximum at intermediate soil water content was observed at the Rollesbroich test site (5 cm), and this behavior was also predicted by our closed form-expression. This is related to the high predicted value of $\sigma(\ln(K_s))$ (Table 4. 2) for this site. At the Scheyern test site, an abrupt increase in soil water content variability was observed at 50 cm depth as compared to the shallower soil depth, and this is also nicely captured by the closed-form expression. Table 4. 2 shows that this increase is caused by the high value of σ_n at this depth.

In order to assess the effect of the pressure head fluctuations on the predicted $\sigma_\theta(<\theta>)$, we also calculated $\sigma_\theta(<\theta>)$ neglecting variations in pressure head ($h'=0$). We found that $\sigma_\theta(<\theta>)$ did not depend strongly on pressure head fluctuations in dry conditions (Figure 4. 4). This implies that variability in soil hydraulic properties dominates σ_θ in this soil water content range, and also explains the good fit to the observed data despite the fact that gravitational downward water flow is not likely to occur in the dry water content range. Pressure head fluctuations were more important in wet conditions, especially in soils with high sand content (Figure 4. 4).

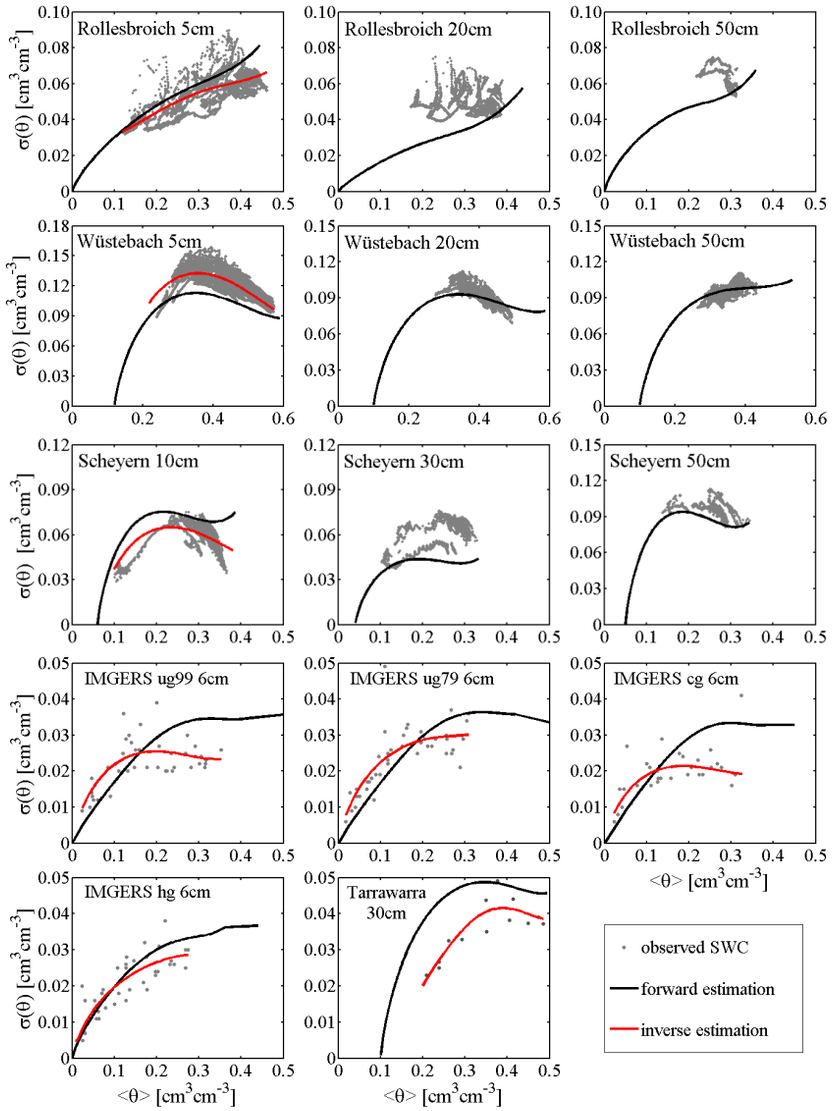

Figure 4. 3. Field observed $\sigma_\theta(<\theta>)$ data from the three TERENO test sites (Rollesbroich, Wüstebach and Scheyern), the four IMGERS experiment sites (ug99, ug79, cg and hg), and the Tarrawarra test site as well as the forward and inverse estimation results.

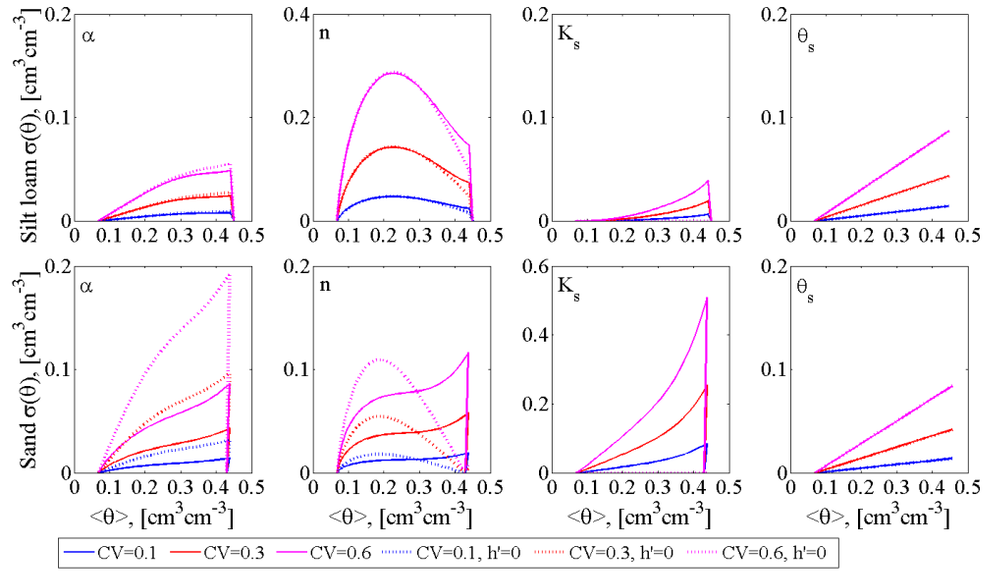

Figure 4. 4 The effect of variability of VGM parameters (α, n, ln(Ks), and θs, parameters are from Rosetta) on $\sigma_\theta(<\theta>)$ curve for silt and sand using three different degrees of variability expressed as coefficient of variation. Solid lines indicate the original closed-form expression ($h' \neq 0$) and dashed lines indicate the simplified version neglecting pressure head variation ($h' = 0$).

Noticeable deviations between observed and predicted $\sigma_\theta(<\theta>)$ can also be observed as well in Figure 4. 3. For example, $\sigma_\theta(<\theta>)$ at 5 cm depth at the Wüstebach test site and $\sigma_\theta(<\theta>)$ at 20 and 50 cm depth in the Rollesbroich test site were clearly underestimated. This can be explained by several factors. First, both the soil hydraulic parameter estimates obtained from the pedotransfer functions and the closed-form expression are only approximations. Second, the $\sigma_\theta(<\theta>)$ relationship is not only affected by soil hydraulic parameters but also by the interplay between evapotranspiration, interception, infiltration and lateral redistribution amongst other factors.

Compared to the other test sites, the IMGERS plots are considerably smaller and relatively homogeneous, which is reflected in the relatively small standard deviation of the VGM parameters (Table 4. 2). This results in comparably small predicted $\sigma_\theta(<\theta>)$ values for the IMGERS plots, which is in good agreement with measured $\sigma_\theta(<\theta>)$ values as indicated by the R^2-values that ranged between 0.55 and 0.84, and root mean square error values ranged between 0.005 cm^3cm^{-3} and 0.006 cm^3cm^{-3} (Table 4. 2). The good match between observations and predictions at this test site is likely related to the lack of lateral water fluxes and the relatively homogeneous vegetation within each treatment, which suggests that $\sigma_\theta(<\theta>)$ is likely dominated by the variability of the soil hydraulic properties.

The soil texture at Tarrawarra covers several soil textural classes (Figure 4. 1). However, the predicted values for the hydraulic parameters and their variability are similar to those found for the IMGERS plots despite the considerably larger area of Tarrawarra, except for $<\ln(K_s)>$ which is not included in the closed-form expression (Eq. 4. 4). Therefore, the predicted $\sigma_\theta(<\theta>)$ values at Tarrawarra are also relatively low compared to the TERENO test sites in Figure 4. 3. Interestingly, Tarrawarra is the only test site where the closed-form expression overestimates $\sigma_\theta(<\theta>)$. This might be an indication for processes compensating soil water content variability (e.g. higher transpiration rates in wetter parts of the Tarrawarra site or lateral water redistribution during wet seasons).

On the other hand, noticeable deviations can be observed as well in Figure 4. 3. For example, $\sigma_\theta(<\theta>)$ at 5 cm depth at the Wüstebach test site and $\sigma_\theta(<\theta>)$ at 20 and 50 cm depth in the Rollesbroich test site were clearly underestimated. This can be explained by several factors.

First, both the soil hydraulic parameter estimates obtained from the pedotransfer functions and the closed-form expression are only approximations. Second, the $\sigma_\theta(<\theta>)$ relationship is not only affected by soil hydraulic parameters but also by the interplay between evapotranspiration, interception, infiltration and lateral redistribution amongst other factors.

Table 4. 3. Correlation coefficients between observed and simulated σ_θ values.

			Forward		Inverse	
			R^2	RMSE	R^2	RMSE
Rollesbroich		5 cm	0.76	0.007	0.79	0.007
		20 cm	0.08	0.019	-	-
		50 cm	0.22	0.021	-	-
Wüstebach		5 cm	0.55	0.020	0.77	0.014
		20 cm	0.64	0.006	-	-
		50 cm	0.56	0.011	-	-
Scheyern		10 cm	0.72	0.008	0.86	0.006
		20 cm	0.77	0.027	-	-
		50 cm	0.43	0.014	-	-
IMGERS	ug99	0-6 cm	0.55	0.007	0.72	0.006
	ug79		0.84	0.007	0.88	0.006
	cg		0.59	0.007	0.69	0.006
	hg		0.82	0.005	0.83	0.005
Tarrawarra		0-30 cm	0.80	0.017	0.83	0.005

Compared to the other test sites, the IMGERS plots are considerably smaller and relatively homogeneous, which is reflected in the relatively small standard deviation of the VGM parameters (Table 4. 2). This results in comparably small predicted σ_θ values for the IMGERS plots, which is in good agreement with measured $\sigma_\theta(<\theta>)$ values as indicated by the R^2-values that ranged between 0.55 and 0.84 (Table 4. 3). The good match between

observations and predictions at this test site is likely related to the lack of lateral water fluxes and the relatively homogeneous vegetation within each treatment, which suggests that $\sigma_\theta(<\theta>)$ is likely dominated by the variability of the soil hydraulic properties.

The soil texture at Tarrawarra covers several soil textural classes (Figure 4. 1). However, the predicted values for the hydraulic parameters and their variability are similar to those found for the IMGERS plots despite the considerably larger area of Tarrawarra, except for $<ln(K_s)>$ which is not included in the closed-form expression (Eq. 4.). Therefore, the predicted σ_θ values at Tarrawarra are also relatively low compared to the TERENO test sites in Figure 4. 3. Interestingly, Tarrawarra is the only test site where the closed-form expression overestimates σ_θ. This might be an indication for processes compensating soil water content variability (e.g. higher transpiration rates in wetter parts of the Tarrawarra site or lateral water redistribution during wet seasons).

4.5.3 Inverse estimation of hydraulic parameter variability from observed $\sigma_\theta(<\theta>)$ data

We tested whether it is feasible to inversely estimate the variability of hydraulic parameters in Eq. 4. using the observed $\sigma_\theta(<\theta>)$ datasets described above. Estimating both the mean soil hydraulic parameters and their standard deviations in Eq. 4. turned out not to be possible (not shown) as no unique solutions could be obtained. In order to better constrain parameter estimates, a wide range of $<\theta>$ is needed. Since the variation of $<\theta>$ was less pronounced in the subsoil, we only analyzed soil water content data measured in the topsoil. We used a Markov Chain Monte Carlo algorithm (Vrugt et al., 2009) to inversely estimate the standard deviations of soil hydraulic parameters from measured $\sigma_\theta(<\theta>)$ data. We used wide parameter bounds to fully explore the parameter space (Table 4. 4). The generally high R^2-values listed

in Table 4. 3 indicate that the inversely estimated variability of hydraulic parameters (Table 4. 5) was able to capture the observed $\sigma_\theta(<\theta>)$ better than the forward model (Figure 4. 3). The inverse modeling particularly captured the peak of the observed $\sigma_\theta(<\theta>)$ at 5 cm depth much better (Figure 4. 3) than the forward estimation, leading to an increase of R^2-value from 0.23 to 0.77 at the Wüstebach test site. This is due to the higher standard deviation of *n* obtained in the inversion as compared to the estimate provided by the Rosetta pedotransfer function (i.e. σ(n) increased from 0.16 to 0.21).

Table 4. 4. Lower and upper boundaries of hydraulic parameters for the inverse estimation.

	$\log_{10}(\sigma(\theta_s))$	$\log_{10}(\sigma(\alpha))$	log10(σ(n))	log10(σ(ln(K_s)))
Lower	-2	-4	-2	-2
Upper	-0.7	-1.5	-0.3	0.2

Table 4. 5. Results of the best fit parameter set from the inverse $\sigma_\theta(<\theta>)$ model application for the TERENO, IMGERS, and Tarrawarra test sites.

		$\sigma(\theta_s)$	$\sigma(\alpha)$	σ(n)	σ(ln(K_s))
Rollesbroich (5 cm)		0.08	0.002	0.13	0.60
Wüstebach (5 cm)		0.05	0.004	0.21	0.41
Scheyern (10 cm)		0.02	0.013	0.15	0.10
IMGERS	ug99	0.02	0.002	0.07	0.32
	ug79	0.02	0.002	0.06	0.08
	cg	0.02	0.001	0.06	0.74
	hg	0.02	0.003	0.05	0.49
	0-6 cm				
Tarrawarra (0-30 cm)		0.01	0.004	0.05	0.11

4.6 Conclusions

We presented a new closed-form expression for $\sigma_\theta(<\theta>)$ based on the VGM model to study the effect of soil hydraulic properties on $\sigma_\theta(<\theta>)$. The sensitivity analysis showed that hydraulic parameters and their spatial variability affect $\sigma_\theta(<\theta>)$ differently. The most sensitive VGM parameter is the n parameter, followed by $\ln(K_s)$, θ_s, and α, respectively. In a next step, we used basic soil properties (i.e. sand, silt, clay content, and bulk density) to predict $\sigma_\theta(<\theta>)$ relationships for eight datasets with different soil texture and climate conditions using pedotransfer functions and our closed-form expression. In most cases, predicted $\sigma_\theta(<\theta>)$ agreed well with observed $\sigma_\theta(<\theta>)$. This indicates that soil hydraulic parameter variability is an important control on $\sigma_\theta(<\theta>)$. In addition, we demonstrated that the variability of soil hydraulic parameters can be inversely estimated from observed $\sigma_\theta(<\theta>)$ data.

We propose that the closed-form expression should be used in combination with pedotransfer functions and global soil maps to estimate sub-grid variability of soil water content, which is useful to further improve prediction accuracy of large-scale hydrologic, weather, and climate models. In addition, information on sub-grid variability of soil water content may be useful for the estimation of the uncertainty of large-scale remote sensing measurements of soil water content provided by ASCAT, SMOS, and the upcoming SMAP mission.

5 Synthesis

The wireless sensor network technology is ideally suited to provide long-term high spatial and temporal resolution soil water content measurements at catchment scale. The observed spatial variability of soil water content information is important in upscaling and improving hydrology models, weather prediction, and general circulation models. In addition, it is important for validation of large-scale remote sensing measurements of soil water content. This thesis firstly addressed the accuracy of newly developed SPADE TDT soil water content sensors used for the wireless sensor network application; secondly studied the relationship between soil hydraulic properties and spatial variability of soil water content using sensor network data and inverse modeling; furthermore, we predicted the sub-grid variability of soil water content from basic soil information.

5.1 Final Conclusions

Chapter 2 addressed the evaluation of the newly developed SPADE sensor using the two-step calibration procedure in the laboratory. The replication experiment showed that sensor-to-sensor variability was significant, and much larger than the measurement noise introduced by the instrumentation and our experimental procedures. The calibration of the 60 SPADE sensors showed that sensor-specific calibration by considering sensor-to-sensor variability significant improves the estimation of apparent dielectric permittivity as compared to a single universal calibration. Whether a sensor-specific calibration is worthwhile depends on the required accuracy of the wireless sensor network. A temperature correction function was derived in the reference liquids and successfully transferred into two different soil samples. The site specific complex refraction index model was used to convert the apparent dielectric permittivity to soil water content by using 15 soil samples in Rollesbroich catchment.

Considering the porosity and the physical realistic, the parameters of complex refraction index model were fitted for each depth, with a RMSE 0.028 at 5 cm, 0.025 at 20 cm, and 0.022 at 50 cm, respectively.

In Chapter 3 we analyzed the temporally stable characteristics both in soil water content and saturation degree. The range of *MRD* of soil water content and saturation degree show similar tendency that they are decreasing with the increasing of soil depth, these results are in consistent with the high standard deviation of soil water content value at deeper layer. The lower *SDRD* of soil water content and saturation degree at deeper layer indicates that the subsoil was more temporally stable than the topsoil. Our inverse estimated VGM parameters can reproduce the observed soil water content dynamics in all soil depths, with RMSE smaller than 0.08 cm^3cm^{-3} and the R^2 larger than 0.75 for the 41 SoilNet locations. Based on this information, we have explored the potential correlations between hydraulic properties and *MRDs* of soil water content and saturation degree. We found that the *MRDs* of soil water content were positively correlated with the θ_s and n parameters, and negatively correlated with the α and K_s parameters of the *VGM* model. Moreover, the *MRDs* of saturation degree were strongly correlated with the α and n parameters that determine the shape of the *VGM* model.

Chapter 4 presents a new closed-form expression of soil water variability based on van Genuchten-Mualem model and a stochastic analysis of 1D unsaturated gravitational flow. The sensitively analysis showed that the n parameter strongly influenced the shape of $\sigma_\theta(<\theta>)$ curve and specifically the magnitude of the maximum, in following are the parameter of $In(K_s)$, θ_s, and α. We can reproduce the observed $\sigma_\theta(<\theta>)$ patterns by combining our closed-

form expression with the pedotransfer functions of Rosetta from basic soil information for eight datasets located in Germany, China and Australia. Furthermore, we demonstrated that by using soil map and pedotransfer function of Rosetta to estimate VGM parameters combining with our closed-form expression, the variability of soil hydraulic parameters can be inversely estimated with the field observed $\sigma_\theta(<\theta>)$ data, with R^2-values ranging between 0.69 and 0.88.

5.2 Outlook

The two-step calibration procedure based on reference liquids and site specific soil samples provides promising accuracy of soil water content measurements. However, so far conductivity effects have not been accounted for. Thus, further research should be addressing the electrical conductivity correction function using dielectric liquids or porous media which are capable of covering the complete conductivity and permittivity ranges in nature soils.

So far we only analyzed the silt loam soil texture class occurring in our test site Rollesbroich to enhance the understanding of the relationship between soil hydraulic parameters and temporal variability of soil water content. Therefore, we suggest to extent our analysis to other soil textural classes and climate conditions in order to further explore the limitations and potential of this approach. Moreover, the factors that cause lateral redistribution are not yet well quantified. In future studies, the effect of topography on the *MRD* of soil water content and saturation degree should be considered in addition to the heterogeneity of soil hydraulic properties.

We have qualitatively studied the effect of hydraulic properties on the $\sigma_\theta(<\theta>)$ relationships with our novel closed-form expression. However, the factors that influence the $\sigma_\theta(<\theta>)$ relationship are not only affected by soil hydraulic properties but also by the interplay between evapotranspiration, interception, infiltration and lateral redistribution amongst other factors. In future, also meteorological forcing variability and the topographic effects on soil water content spatial distributions of model developments should be considered.

Finally, it can be concluded that the obtained data set provided by the wireless sensor network and the improved understanding of spatial temporal dynamics of soil water content can be used for data assimilation in hydrological models; calibration and validation of remote sensing retrievals of soil water content; estimating uncertainty in hydrological predictions; designing sensor networks and optimizing the number of sensors; and upscaling and downscaling of soil water content information.

Appendix A

In this section the apparent dielectric permittivity is converted to soil water content for Rollesbroich test site. The 15 undisturbed samples (length =7.7 cm, diameter = 5 cm) were taken from the two main soil types in 5, 20 and 50 cm depth. There are empirical and semi-theoretical models to solve the relationship between the apparent dielectric permittivity and the volume soil water content. Such as Topp model (Topp et al., 1980), which works well in sand soil; the two-point α-mixing model (Sakaki et al., 2008), just consider the air-dry and water-saturated conditions to set the model; and the petrophysical model of CRIM (Birchak et al., 1974), which has physical meaning, soil type and shape factor affect the soil water content. Here we use CRIM described in Eq. 2. 7 to convert apparent dielectric permittivity to soil water content with the site specific calibration.

The petrophysical model of CRIM for Rollesbroich catchment is determined in the laboratory. First step is to saturate the samples with the deionized water. Then insert the CS 640-L 3 –rod TDR100 probes in the middle of the sample to measure the permittivity of the samples (Figure A. 1). The MatLab algorithm which based on the travelling time analysis algorithm were used to analyze the TDR measurements (Heimovaara and Bouten, 1990) to estimate the apparent permittivity. Next, the samples were dried in room temperature, both the weight and the permittivities were determined in regular interval time. The volumetric soil water content were determined gravimetrically (soil samples were oven-dried at 105 °C for 24 hours). Because of the shrinkage of the samples caused by the gas and roots, the bad contract between the soils and the probes caused by the small stones, three samples which seemed to be unrepresented for the sampling location were deleted in later analyze.

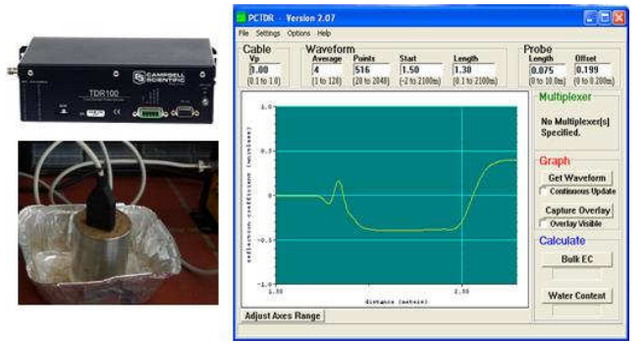

Figure A. 1. Soil samples measurement and waveform of TDR100.

Table A. 1. Parameters and the RMSE of the CRIM model for 5 cm, 20 cm, and 50 cm depth for our Rollesbroich catchment.

	5cm	20cm	50cm
K_{water}	78.54	78.54	78.54
K_{solid}	2.08	3.78	4.40
K_{air}	1.00	1.00	1.00
β	0.50	0.50	0.50
η	0.59	0.49	0.41
RMSE	0.028	0.025	0.022

The final dataset describing the relationship between apparent dielectric permittivity and soil water content using CRIM model are shown in Figure A. 2. Since the large different of porosity for different depths, three semi-theoretical models were fitted to the data and the performance of these models was judged by the RMSE for each depth (Table A. 1). It was found that three fitting methods performed equally well (Table A. 1) with a RMSE smaller than 0.028 cm^3cm^{-3}. The solid permittivity value was fitted and β was 0.5 as it is commonly used in the soil science literature (Birchak et al., 1974). At present, there is no method of measuring the permittivity of the solid mineral component of a granular material, the value of

the K_{solid} remain essentially a fitting parameter and prevent the rigorous testing of dielectric mixing models.

Because of the relatively high accuracy of Eq. 2. 7, we did not consider models with spatially variable porosity that would in principle allow more accurate soil water content predictions when the porosity at each sensor unit and soil depth is known for the wireless sensor network. The large effort required to obtain this additional soil information is too large considering the modest increase in accuracy of the soil water content measurements.

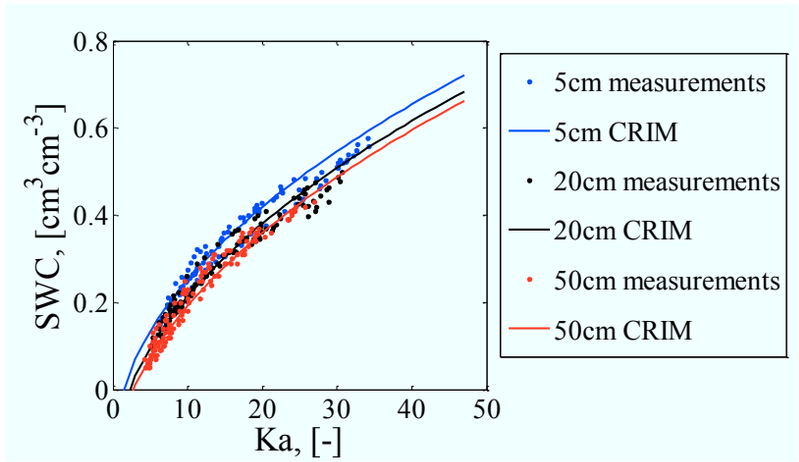

Figure A. 2. Relationship between apparent dielectric permittivity and soil water content in Rollesbroich test site and the derived K_a-θ model.

Appendix B

After the deployment of the sensor network at Rollesbroich test site, we found that the sensor output showed pronounced diurnal variations. Large differences between the two closely-spaced measurements at a single measuring point were also observed. After investigating this in detail, it was established that this behavior was related to the SPADE data acquisition where the first reading result was still affected by charging capacitors within the sensor. If multiple sensor readings were made sequentially without turning off the sensor, the stability of the measurement considerably improved and the temperature dependence of the measurements disappeared.

To correct these temperature-dependent oscillations effect in sensor reading, two reading results were sequentially made at each measurement time (Figure B. 1). We flashed the software to save two measurements each time from 5th September 2012 to 3th March 2013. After 3th March 2013, we only save the correct measurement of our wireless sensor network. However, we need to correct the measurements from April 2011 to September 2012 for all the sensors.

We found that the difference between the two sensor readings (Δv) is strongly correlated with soil temperature, and could be fitted with a sensor-specific second order empirical polynomial with a RMSE of 5.18 mV (Figure B. 2). It means that we can use the polynomial function and the measured soil temperature to calculate the difference between the temperature effected values and the true values.

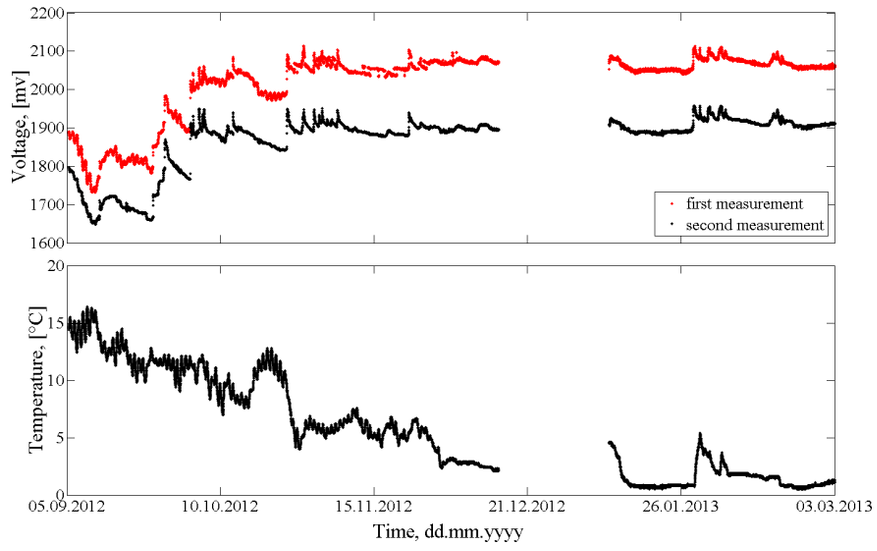

Figure B. 1. Time series data of two measured voltages and temperature after flash, the first measurement is affected by the temperature effect of charging capacitors, the second measurement is the right value.

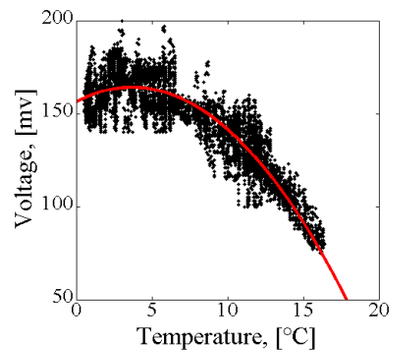

Figure B. 2. Polyfit between soil temperature and the difference between the two measurements at the same time using the second order polynomial function.

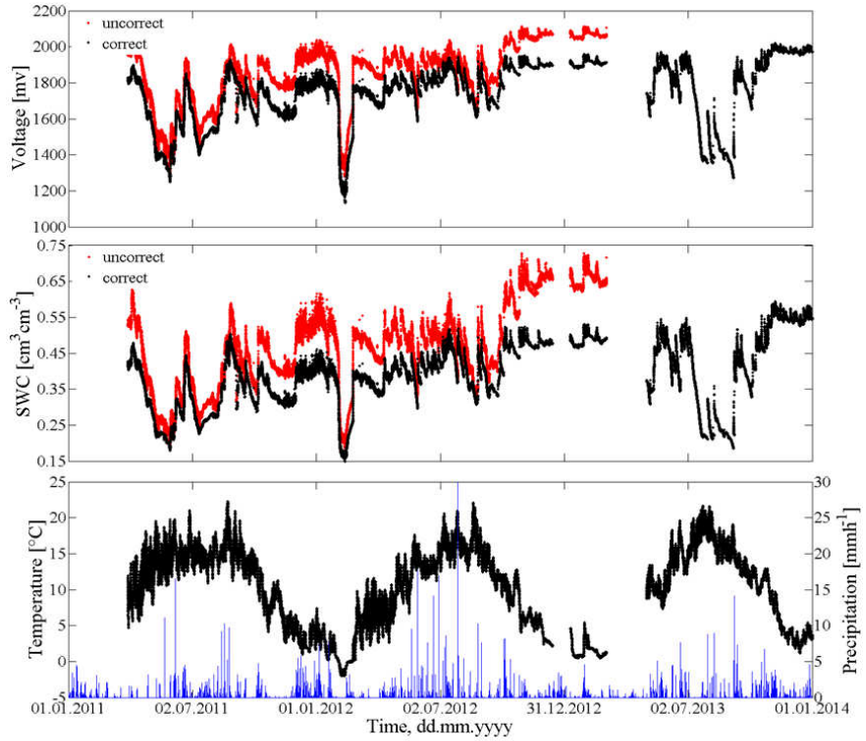

Figure B. 3. Correct the voltage observed before flash using the second order polynomial function, the black lines are the corrected data, and the red lines are the uncorrected data.

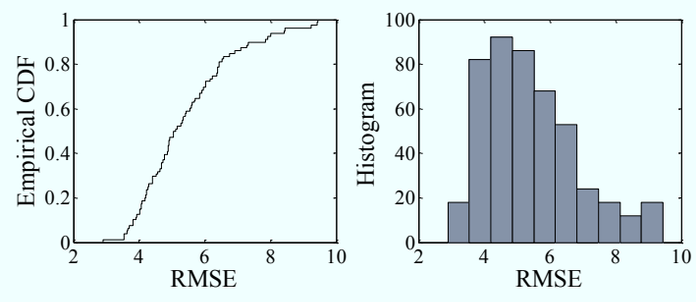

Figure B. 4. Cumulative distribution and the histogram of RMSE between the second order polynomial fitted Δv and measured Δv for all the sensors.

After the second order empirical polynomial function was derived (Figure B. 2), the temperature affected values can be corrected by deducing the Δv which was calibrated from the polynomial function and the soil temperature. And the uncorrected and corrected voltage, as well as soil water content is plotted in Figure B. 3. It is clearly to see that after the correlation for the measurements, the observed voltage before flash corresponds well to the second measurement after flash. In average, the temperature corrected soil water content is 0.07 cm^3cm^{-3} lower than the not corrected values. After flash the software, the second measurement of soil water content is lower than the first measurement, the difference is 0.17 cm^3cm^{-3} in the time period of after flash the software.

Using the method mentioned above, we first derived the second order empirical polynomial functions for all sensors, with a RMSE of fitted Δv and sensor output Δv less than 10 mV (Figure B. 4). Then we corrected the first measurements of the sensors to obtain a consistent time series of soil water content for all locations. After correction, the measurements from the closely-spaced sensors at a single measurement location agreed well with each other with a RMSE that varied from 0.010 to 0.035 cm^3 cm^{-3} between the two sensors installed at the same depths.

Appendix C

In order to derive the statistical moments of pressure head (h) and soil water content (θ), the constitutive relationships between θ and h, and hydraulic conductivity (K) and h must be specified. Previous studies relied on the use of the Brooks-Corey or the Gardner-Russo model for these constitutive relationships because of their mathematical tractability. Here, we present a new derivation using the van Genuchten-Mualem (VGM) model [*van Genuchten*, 1980], which is known to better describe experimental soil water retention data.

For the derivation, we made use of the following expansions (*Abramowitz and Stegun*, 1970; *Bansal*, 2006):

$$(1+x)^c = 1 + cx + \cdots; \quad \text{Eq. C 1}$$

$$(c)^x = 1 + xln(c) + \cdots; \quad \text{Eq. C 2}$$

$$\frac{1}{x} = \frac{1}{x_0} - \frac{1}{x_0^2}(x - x_0) + \cdots; \quad \text{Eq. C 3}$$

$$(x^n + y)^{\frac{1}{n}} = x + \frac{y}{nx^{n-1}} \ldots. \quad \text{Eq. C 4}$$

We assume that the variables and parameters, i.e. pressure head (h), soil water content (θ), hydraulic conductivity (K), effective saturation degree (S_e), saturated soil water content (θ_s), saturated hydraulic conductivity (K_s), and the fitting parameters α and n of the VGM model are realizations of a second-order stationary stochastic process and that they can be decomposed into their mean and perturbations. By applying the expansions from Eq. C 1 to Eq. C 4 to the VGM model and keeping the first-order terms only, a relationship that expresses the variance of soil water content as a function of the variance in VGM model parameters can be derived.

We start with decomposition of different parts of the water retention function of the VGM model. We first decomposed αh as follows,

$$\alpha h = (\langle\alpha\rangle + \alpha')(\langle h\rangle + h') \quad \text{Eq. C 5}$$

where $\langle ... \rangle$ indicates the mean value, and the prime indicates the perturbation. By writing out Eq. C 5 and neglecting small terms (i.e. α'h') we get:

$$\alpha h \approx \langle\alpha\rangle\langle h\rangle + \langle\alpha\rangle h' + \alpha'\langle h\rangle \quad \text{Eq. C 6}$$

Using the same approach, a decomposition of $(\alpha h)^n$ can be obtained:

$$\begin{aligned}(\alpha h)^n &= [(\langle\alpha\rangle + \alpha')(\langle h\rangle + h')]^{\langle n\rangle + n'} \\ &\approx [\langle\alpha\rangle\langle h\rangle + \langle\alpha\rangle h' + \alpha'\langle h\rangle]^{\langle n\rangle}\,[\langle\alpha\rangle\langle h\rangle + \langle\alpha\rangle h' + \alpha'\langle h\rangle]^{n'} \\ &\approx (\langle\alpha\rangle\langle h\rangle)^{\langle n\rangle}\left(1 + \frac{\langle\alpha\rangle h' + \alpha'\langle h\rangle}{\langle\alpha\rangle\langle h\rangle}\right)^{\langle n\rangle}\ (\langle\alpha\rangle\langle h\rangle)^{n'}\left(1 + \frac{\langle\alpha\rangle h' + \alpha'\langle h\rangle}{\langle\alpha\rangle\langle h\rangle}\right)^{n'}\end{aligned} \quad \text{Eq. C 7}$$

By applying the expansion of Eq. C 1 to the second and fourth term of Eq. C 7 and keeping first-order only, Eq. C 7 can be approximated as follows:

$$(\alpha h)^n \approx (\langle\alpha\rangle\langle h\rangle)^{\langle n\rangle}\left(1 + \langle n\rangle\frac{\langle\alpha\rangle h' + \alpha'\langle h\rangle}{\langle\alpha\rangle\langle h\rangle}\right)(\langle\alpha\rangle\langle h\rangle)^{n'}\left(1 + n'\frac{\langle\alpha\rangle h' + \alpha'\langle h\rangle}{\langle\alpha\rangle\langle h\rangle}\right) \quad \text{Eq. C 8}$$

The final term in Eq. C 8 is very close to 1. Therefore, A8 can be simplified to:

$$(\alpha h)^n \approx (\langle\alpha\rangle\langle h\rangle)^{\langle n\rangle}\left(1 + \langle n\rangle\frac{\langle\alpha\rangle h' + \alpha'\langle h\rangle}{\langle\alpha\rangle\langle h\rangle}\right)(\langle\alpha\rangle\langle h\rangle)^{n'} \quad \text{Eq. C 9}$$

By applying the expansion of Eq. C 2 to the last term of Eq. C 9, the following approximation can be obtained:

$$(\alpha h)^n \approx (\langle\alpha\rangle\langle h\rangle)^{\langle n\rangle}\left(1 + \langle n\rangle\frac{\langle\alpha\rangle h' + \alpha'\langle h\rangle}{\langle\alpha\rangle\langle h\rangle}\right)[1 + n' ln(\langle\alpha\rangle\langle h\rangle)] \quad \text{Eq. C 10}$$

By writing out Eq. C 10 and neglecting small terms, we finally derived an approximation for the decomposition of $(\alpha h)^n$:

$$(\alpha h)^n \approx (\langle\alpha\rangle\langle h\rangle)^{\langle n\rangle} + (\langle\alpha\rangle\langle h\rangle)^{\langle n\rangle}\left[\frac{\langle n\rangle}{\langle\alpha\rangle}\alpha' + \frac{\langle n\rangle}{\langle h\rangle}h' + n' ln(\langle\alpha\rangle\langle h\rangle)\right] \quad \text{Eq. C 11}$$

Following the same steps as used in Eq. C 7 to Eq. C 11, an expression for the decomposition of $(\alpha h)^{-n}$ can be derived:

$$(\alpha h)^{-n} \approx (\langle\alpha\rangle\langle h\rangle)^{-\langle n\rangle} + (\langle\alpha\rangle\langle h\rangle)^{-\langle n\rangle}\left[-\frac{\langle n\rangle}{\langle\alpha\rangle}\alpha' - \frac{\langle n\rangle}{\langle h\rangle}h' - n' ln(\langle\alpha\rangle\langle h\rangle)\right] \quad \text{Eq. C 12}$$

By expanding $\frac{1}{(1+(ah)^n)}$ at the mean value of $(\langle\alpha\rangle\langle h\rangle)^{\langle n\rangle}$ following Eq. C 3, we obtained:

$$\frac{1}{(1+(ah)^n)} \approx \frac{1}{(1+(\langle\alpha\rangle\langle h\rangle)^{\langle n\rangle})} - \frac{(ah)^n - (\langle\alpha\rangle\langle h\rangle)^{\langle n\rangle}}{(1+(\langle\alpha\rangle\langle h\rangle)^{\langle n\rangle})^2} \quad \text{Eq. C 13}$$

Substituting Eq. C 11 into Eq. C 13 resulted in:

$$\frac{1}{1+(ah)^n} \approx \frac{1}{(1+(\langle\alpha\rangle\langle h\rangle)^{\langle n\rangle})} - \frac{(\langle\alpha\rangle\langle h\rangle)^{\langle n\rangle}}{(1+(\langle\alpha\rangle\langle h\rangle)^{\langle n\rangle})^2}\left[\frac{\langle n\rangle}{\langle\alpha\rangle}\alpha' + \frac{\langle n\rangle}{\langle h\rangle}h' + n' ln(\langle\alpha\rangle\langle h\rangle)\right] \quad \text{Eq. C 14}$$

By applying the expansion of Eq. C 4 to $(1+(ah)^n)^{\frac{1}{n}}$, we got:

$$(1+(ah)^n)^{\frac{1}{n}} \approx \alpha h + \frac{1}{n}(\alpha h)^{-(n-1)} = \alpha h\left[1 + \frac{1}{n}(\alpha h)^{-n}\right] \quad \text{Eq. C 15}$$

By substituting the expressions for αh (Eq. C 6), $(\alpha h)^{-n}$ (Eq. C 12), and using the expansion $\frac{1}{n} = \frac{1}{\langle n\rangle} - \frac{n\prime}{\langle n\rangle^2}$, Eq. C 15 can be rewritten as:

$$(1+(ah)^n)^{\frac{1}{n}} \approx [\langle\alpha\rangle\langle h\rangle + \langle\alpha\rangle h' + \alpha'\langle h\rangle]\left\{1 + (\frac{1}{\langle n\rangle} - \frac{n'}{\langle n\rangle^2})(\langle\alpha\rangle\langle h\rangle)^{-\langle n\rangle}\left[1 - -\frac{\langle n\rangle}{\langle\alpha\rangle}\alpha' - \frac{\langle n\rangle}{\langle h\rangle}h' - n' ln(\langle\alpha\rangle\langle h\rangle)\right]\right\} \quad \text{Eq. C 16}$$

The VGM model can be written as:

$$\theta = (\theta_s - \theta_r)\frac{1}{1+(ah)^n}\,(1+(ah)^n)^{\frac{1}{n}} + \theta_r \quad \text{Eq. C 17}$$

After substituting the decompositions of $\frac{1}{1+(ah)^n}$ (Eq. C 14) and $(1+(ah)^n)^{\frac{1}{n}}$ (Eq. 16), and decomposing θ_s into $\langle\theta_s\rangle+\theta_s'$, we obtained an expression for the mean and perturbation of soil water content as a function of the VGM parameters. After rearranging and neglecting small terms, we obtained:

$$\begin{aligned}
&\langle\theta\rangle+\theta' \approx (\langle\theta_s\rangle-\theta_r)\left(\frac{\langle\alpha\rangle\langle h\rangle}{1+(\langle\alpha\rangle\langle h\rangle)^{\langle n\rangle}}\right)\left(\frac{\langle n\rangle(\langle\alpha\rangle\langle h\rangle)^{\langle n\rangle}+1}{\langle n\rangle(\langle\alpha\rangle\langle h\rangle)^{\langle n\rangle}}\right)+\theta_r \\
&+(\langle\theta_s\rangle-\theta_r)\left(\frac{\langle\alpha\rangle\langle h\rangle}{[1+(\langle\alpha\rangle\langle h\rangle)^{\langle n\rangle}](\langle\alpha\rangle\langle h\rangle)^{\langle n\rangle}\langle n\rangle}\right)* \\
&\left\{\left[\frac{\langle n\rangle(\langle\alpha\rangle\langle h\rangle)^{\langle n\rangle}+1-\langle n\rangle}{\langle\alpha\rangle}-\frac{\left[\langle n\rangle(\langle\alpha\rangle\langle h\rangle)^{\langle n\rangle}+1\right](\langle\alpha\rangle\langle h\rangle)^{\langle n\rangle}}{1+(\langle\alpha\rangle\langle h\rangle)^{\langle n\rangle}}\frac{\langle n\rangle}{\langle\alpha\rangle}\right]\alpha'\right. \\
&+\left[\frac{\langle n\rangle(\langle\alpha\rangle\langle h\rangle)^{\langle n\rangle}+1-\langle n\rangle}{\langle h\rangle}-\frac{\left[\langle n\rangle(\langle\alpha\rangle\langle h\rangle)^{\langle n\rangle}+1\right](\langle\alpha\rangle\langle h\rangle)^{\langle n\rangle}}{1+(\langle\alpha\rangle\langle h\rangle)^{\langle n\rangle}}\frac{\langle n\rangle}{\langle h\rangle}\right]h' \\
&+\left[\langle n\rangle(\langle\alpha\rangle\langle h\rangle)^{\langle n\rangle}+1\right]\theta_s' \\
&\left.+\left[-\frac{1}{\langle n\rangle}-In(\langle\alpha\rangle\langle h\rangle)-\frac{\left[\langle n\rangle(\langle\alpha\rangle\langle h\rangle)^{\langle n\rangle}+1\right](\langle\alpha\rangle\langle h\rangle)^{\langle n\rangle}}{1+(\langle\alpha\rangle\langle h\rangle)^{\langle n\rangle}}ln(\langle\alpha\rangle\langle h\rangle)\right]n'\right\}
\end{aligned} \qquad \text{Eq. C 18}$$

From this expression, we can derive a first-order approximation of the mean of soil water content and its perturbation:

$$\langle\theta\rangle=(\langle\theta_s\rangle-\theta_r)\left(\frac{\langle\alpha\rangle\langle h\rangle}{1+(\langle\alpha\rangle\langle h\rangle)^{\langle n\rangle}}\right)\left(\frac{\langle n\rangle(\langle\alpha\rangle\langle h\rangle)^{\langle n\rangle}+1}{\langle n\rangle(\langle\alpha\rangle\langle h\rangle)^{\langle n\rangle}}\right)+\theta_r \qquad \text{Eq. C 19}$$

$$\theta'=b_0[b_1\alpha'+b_2h'+b_3n'+b_4\theta_s'] \qquad \text{Eq. C 20}$$

where

$$b_0=(\langle\theta_s\rangle-\theta_r)\left(\frac{\langle\alpha\rangle\langle h\rangle}{[1+(\langle\alpha\rangle\langle h\rangle)^{\langle n\rangle}](\langle\alpha\rangle\langle h\rangle)^{\langle n\rangle}\langle n\rangle}\right) \qquad \text{Eq. C 21}$$

$$b_1=\frac{\langle n\rangle(\langle\alpha\rangle\langle h\rangle)^{\langle n\rangle}+1-\langle n\rangle}{\langle\alpha\rangle}-\frac{\left[\langle n\rangle(\langle\alpha\rangle\langle h\rangle)^{\langle n\rangle}+1\right](\langle\alpha\rangle\langle h\rangle)^{\langle n\rangle}}{1+(\langle\alpha\rangle\langle h\rangle)^{\langle n\rangle}}\frac{\langle n\rangle}{\langle\alpha\rangle} \qquad \text{Eq. C 22}$$

$$b_2=\frac{\langle n\rangle(\langle\alpha\rangle\langle h\rangle)^{\langle n\rangle}+1-\langle n\rangle}{\langle h\rangle}-\frac{\left[\langle n\rangle(\langle\alpha\rangle\langle h\rangle)^{\langle n\rangle}+1\right](\langle\alpha\rangle\langle h\rangle)^{\langle n\rangle}}{1+(\langle\alpha\rangle\langle h\rangle)^{\langle n\rangle}}\frac{\langle n\rangle}{\langle h\rangle} \qquad \text{Eq. C 23}$$

$$b_3=-\frac{1}{\langle n\rangle}-ln(\langle\alpha\rangle\langle h\rangle)-\frac{\left[\langle n\rangle(\langle\alpha\rangle\langle h\rangle)^{\langle n\rangle}+1\right](\langle\alpha\rangle\langle h\rangle)^{\langle n\rangle}}{1+(\langle\alpha\rangle\langle h\rangle)^{\langle n\rangle}}ln(\langle\alpha\rangle\langle h\rangle) \qquad \text{Eq. C 24}$$

$$b_4=\langle n\rangle(\langle\alpha\rangle\langle h\rangle)^{\langle n\rangle}+1 \qquad \text{Eq. C 25}$$

Equation Eq. C 19 expresses the mean soil water content as a function of the mean VGM parameters and Eq. C 20 shows that the perturbation of soil water content is linearly related to the perturbation of the VGM parameters (α', n', and θ_s') and the pressure head (h').

The covariance of soil water content can be derived as follows,

$$Cov_\theta(r) = Cov(\theta_\alpha, \theta_\beta) = \langle(\theta_\alpha - \langle\theta_\alpha\rangle)(\theta_\beta - \langle\theta_\beta\rangle)\rangle = \theta'_\alpha * \theta'_\beta$$
$$= b_0\left[b_1\alpha'_\alpha + b_2h'_\alpha + b_3n'_\alpha + b_4{\theta_s}'_\alpha\right] * b_0\left[b_1\alpha'_\alpha + b_2h'_\alpha + b_3n'_\alpha + b_4{\theta_s}'_\alpha\right]$$
$$= b_0^2\begin{bmatrix} b_1^2(\alpha'_\alpha\alpha'_\beta) + b_2^2(h'_\alpha h'_\beta) + b_3^2(n'_\alpha n'_\beta) + b_4^2({\theta_s}'_\alpha{\theta_s}'_\beta) \\ +b_1b_2(\alpha'_\alpha h'_\beta + h'_\alpha\alpha'_\beta) + b_1b_3(\alpha'_\alpha n'_\beta + n'_\alpha\alpha'_\beta) \\ +b_1b_4(\alpha'_\alpha{\theta_s}'_\beta + {\theta_s}'_\alpha\alpha'_\beta) + b_2b_3(h'_\alpha n'_\beta + n'_\alpha h'_\beta) \\ +b_2b_4(h'_\alpha{\theta_s}'_\beta + {\theta_s}'_\alpha h'_\beta) + b_3b_4(n'_\alpha{\theta_s}'_\beta + {\theta_s}'_\alpha n'_\beta) \end{bmatrix} \quad \text{Eq. C 26}$$
$$= {b_0}^2\{{b_1}^2Cov_\alpha(\boldsymbol{r}) + {b_2}^2Cov_h(\boldsymbol{r}) + {b_3}^2Cov_n(\boldsymbol{r}) + {b_4}^2Cov_{\theta_s}(\boldsymbol{r})$$
$$+b_1b_2[Cov_{\alpha h}(\boldsymbol{r}) + Cov_{\alpha h}(-\boldsymbol{r})] + b_1b_3[Cov_{\alpha n}(\boldsymbol{r}) + Cov_{\alpha n}(-\boldsymbol{r})]$$
$$+b_1b_4\left[Cov_{\alpha\theta_s}(\boldsymbol{r}) + Cov_{\alpha\theta_s}(-\boldsymbol{r})\right] + b_2b_3[Cov_{nh}(\boldsymbol{r}) + Cov_{nh}(-\boldsymbol{r})]$$
$$+b_2b_4\left[Cov_{h\theta_s}(\boldsymbol{r}) + Cov_{h\theta_s}(-\boldsymbol{r})\right] + b_3b_4\left[Cov_{n\theta_s}(\boldsymbol{r}) + Cov_{n\theta_s}(-\boldsymbol{r})\right]\}$$

where ***r*** is a vector (***r*** = α-β, and -***r*** = β-α), α and β are positions within the soil profile, and b_0 to b_4 are as defined above (Eq. C 21 to Eq. C 25). This equation shows that the covariance of soil water content is only related to the covariances of the VGM parameters and pressure head. We explain the positive (***r***) and negative (-***r***) covariances shown in Eq. C 26 with the example covariance between α_α and h_β:

$$Cov_{\alpha h}(\boldsymbol{r}) = Cov(\alpha_\alpha, h_\beta) = \langle(\alpha_\alpha - \langle\alpha_\alpha\rangle)(h_\beta - \langle h_\beta\rangle)\rangle = \alpha'_\alpha * h'_\beta \quad \text{Eq. C 27}$$
$$Cov_{\alpha h}(-\boldsymbol{r}) = Cov(\alpha_\beta, h_\alpha) = \langle(\alpha_\beta - \langle\alpha_\beta\rangle)(h_\alpha - \langle h_\alpha\rangle)\rangle = \alpha'_\beta * h'_\alpha \quad \text{Eq. C 28}$$

The other covariances in Eq. C 26 can be expressed in a similar manner.

In a next step, we derive the covariance between the VGM model parameters and the pressure head, which involves a first-order approximation of the hydraulic conductivity function of the

VGM model. For mathematical convenience, we used a natural logarithm transformation of hydraulic conductivity, i.e. Y=*ln*(K), f=*ln*(K_s). The hydraulic conductivity of VGM model can be written as:

$$Y = f + \frac{1}{2} ln(\frac{1}{1+(ah)^n})^m + 2ln\left\{1 - \left[1 - \left(\frac{1}{(1+(ah)^n)^m}\right)^{\frac{1}{m}}\right]^m\right\} \quad \text{Eq. C 29}$$

where $m = 1 - \frac{1}{n}$.

Writing out the last term of Eq. C 29 and replacing m with $1 - \frac{1}{n}$ resulted in:

$$1 - \left[1 - \left(\frac{1}{(1+(ah)^n)^m}\right)^{\frac{1}{m}}\right]^m = 1 - (ah)^n \left[\frac{1}{1+(ah)^n}\right] \frac{1}{ah} [1+(ah)^n]^{\frac{1}{n}} \quad \text{Eq. C 30}$$

By applying the expansion of Eq. C 4 to $[1+(ah)^n]^{\frac{1}{n}}$, we obtained:

$$1 - \left[1 - \left(\frac{1}{(1+(ah)^n)^m}\right)^{\frac{1}{m}}\right]^m \approx 1 - (ah)^n \left[\frac{1}{1+(ah)^n}\right] \frac{1}{ah} \left[ah + \frac{1}{n(ah)^{n-1}}\right] \quad \text{Eq. C 31}$$

By rewriting the right side of Eq. C 31, we obtained:

$$1 - \left[1 - \left(\frac{1}{(1+(ah)^n)^m}\right)^{\frac{1}{m}}\right]^m \approx \frac{1}{1+(ah)^n}\left(1 - \frac{1}{n}\right) \quad \text{Eq. C 32}$$

By substituting Eq. C 32 into Eq. C 29, we obtained:

$$Y \approx f + \frac{1}{2}\left(1 - \frac{1}{n}\right) ln\left[\frac{1}{1+(ah)^n}\right] + 2ln\left[\frac{1}{1+(ah)^n}\right] + ln\left(1 - \frac{1}{n}\right) \quad \text{Eq. C 33}$$

Inserting Eq. C 3 and Eq. C 14 into Eq. C 33, and decomposing f into <f>+f' resulted in:

$$\langle Y\rangle + Y' \approx \langle f\rangle + 2ln\left(1 - \frac{1}{\langle n\rangle}\right) + \left(\frac{5}{2} - \frac{1}{2\langle n\rangle}\right) ln\left(\frac{1}{1+(\langle\alpha\rangle\langle h\rangle)^{\langle n\rangle}}\right)$$
$$+ f' - \left\{\left[\frac{(\frac{5}{2} - \frac{1}{2\langle n\rangle})(\langle\alpha\rangle\langle h\rangle)^{\langle n\rangle}}{1+(\langle\alpha\rangle\langle h\rangle)^{\langle n\rangle}} \frac{\langle n\rangle}{\langle\alpha\rangle}\right]\alpha' \right. \quad \text{Eq. C 34}$$

$$-\left[\frac{(\frac{5}{2}-\frac{1}{2\langle n\rangle})(\langle\alpha\rangle\langle h\rangle)^{\langle n\rangle}}{1+(\langle\alpha\rangle\langle h\rangle)^{\langle n\rangle}}\frac{\langle n\rangle}{\langle h\rangle}\right]h'$$
$$-\left[\frac{\left(\frac{5}{2}-\frac{1}{2\langle n\rangle}\right)(\langle\alpha\rangle\langle h\rangle)^{\langle n\rangle}}{1+(\langle\alpha\rangle\langle h\rangle)^{\langle n\rangle}}ln(\langle\alpha\rangle\langle h\rangle)+\frac{ln\left[1+(\langle\alpha\rangle\langle h\rangle)^{\langle n\rangle}\right]}{2\langle n\rangle^2}-\frac{2}{\langle n\rangle^2-\langle n\rangle}\right]n'\Bigg\}$$

After rearranging, the following first-order approximations for the hydraulic conductivity and its perturbation are obtained:

$$\langle Y\rangle=\langle f\rangle+2ln\left(1-\frac{1}{\langle n\rangle}\right)+\left(\frac{5}{2}-\frac{1}{2\langle n\rangle}\right)ln\left(\frac{1}{1+(\langle\alpha\rangle\langle h\rangle)^{\langle n\rangle}}\right) \quad \text{Eq. C 35}$$

$$Y'=f'-a_1\alpha'-a_2h'-a_3n' \quad \text{Eq. C 36}$$

where

$$a_1=\frac{(\frac{5}{2}-\frac{1}{2\langle n\rangle})(\langle\alpha\rangle\langle h\rangle)^{\langle n\rangle}}{1+(\langle\alpha\rangle\langle h\rangle)^{\langle n\rangle}}\frac{\langle n\rangle}{\langle\alpha\rangle} \quad \text{Eq. C 37}$$

$$a_2=\frac{(\frac{5}{2}-\frac{1}{2\langle n\rangle})(\langle\alpha\rangle\langle h\rangle)^{\langle n\rangle}}{1+(\langle\alpha\rangle\langle h\rangle)^{\langle n\rangle}}\frac{\langle n\rangle}{\langle h\rangle} \quad \text{Eq. C 38}$$

$$a_3=\frac{\left(\frac{5}{2}-\frac{1}{2\langle n\rangle}\right)(\langle\alpha\rangle\langle h\rangle)^{\langle n\rangle}}{1+(\langle\alpha\rangle\langle h\rangle)^{\langle n\rangle}}ln(\langle\alpha\rangle\langle h\rangle)+\frac{ln\left[1+(\langle\alpha\rangle\langle h\rangle)^{\langle n\rangle}\right]}{2\langle n\rangle^2}-\frac{2}{\langle n\rangle^2-\langle n\rangle} \quad \text{Eq. C 39}$$

For reasons of mathematical tractability, we only consider gravity-dominated flow. Therefore, we substituted the pressure head $h(x)=\langle h\rangle+h'$ and log-transformed hydraulic conductivity $Y(x)=\langle Y(x)\rangle+Y'$ into the steady-state simplification of the Richards equation ($\frac{\partial}{\partial x}\left[K(h)(\frac{\partial h}{\partial x}+1)\right]=0$). The perturbation of pressure head can be expressed as:

$$(\langle Y\rangle+Y')\frac{\partial^2\langle h(x)\rangle}{\partial x^2}+(\langle Y\rangle+Y')\frac{\partial^2h(x)'}{\partial x^2}+\frac{\partial\langle h(x)\rangle}{\partial x}\frac{\partial\langle Y(x)\rangle}{\partial x}+\frac{\partial\langle Y(x)\rangle}{\partial x}\frac{\partial h(x)'}{\partial x}$$
$$+\frac{\partial\langle h(x)\rangle}{\partial x}\frac{\partial Y(x)'}{\partial x}+\frac{\partial h(x)'}{\partial x}\frac{\partial Y(x)'}{\partial x}+\frac{\partial\langle Y(x)\rangle}{\partial x}+\frac{\partial Y(x)'}{\partial x}=0 \quad \text{Eq. C 40}$$

The covariance between pressure head and hydraulic conductivity was already derived by Zhang et al. [1998], so here we just briefly reiterate the fundamental steps of this derivation. Since $\langle h(x)\rangle$ and $\langle Y(x)\rangle$ are constant and by neglecting higher-order terms, the following expression can be obtained from Eq. C 40:

$$\frac{\partial^2 h(x)'}{\partial x^2} + \frac{\partial Y(x)'}{\partial x} = 0 \qquad \text{Eq. C 41}$$

By substituting Eq. C 36 into Eq. C 41, we obtained the following equation:

$$\frac{\partial^2 h(x)'}{\partial x^2} - a_2 \frac{\partial h(x)'}{\partial x} = -\frac{\partial f'}{\partial x} + a_1 \frac{\partial \alpha'}{\partial x} + a_3 \frac{\partial n'}{\partial x} \qquad \text{Eq. C 42}$$

By multiplying Eq. C 42 with the head fluctuations at a different location and taking the ensemble mean, we obtained the following expression for the covariance of pressure head:

$$\frac{\partial^2 Cov_h(\boldsymbol{r})}{\partial \boldsymbol{r}^2} - a_2 \frac{\partial Cov_h(\boldsymbol{r})}{\partial \boldsymbol{r}} = -\frac{\partial Cov_{fh}(\boldsymbol{r})}{\partial \boldsymbol{r}} + a_1 \frac{\partial Cov_{\alpha h}(\boldsymbol{r})}{\partial \boldsymbol{r}} + a_3 \frac{\partial Cov_{nh}(\boldsymbol{r})}{\partial \boldsymbol{r}} \qquad \text{Eq. C 43}$$

Using the same method, we derived the following three equations for the covariance between the hydraulic parameters of the VGM model:

$$\frac{\partial Cov_{fh}(\boldsymbol{r})}{\partial \boldsymbol{r}^2} - a_2 \frac{\partial Cov_{fh}(\boldsymbol{r})}{\partial \boldsymbol{r}} = \frac{\partial Cov_f(\boldsymbol{r})}{\partial \boldsymbol{r}} - a_1 \frac{\partial Cov_{f\alpha}(\boldsymbol{r})}{\partial \boldsymbol{r}} - a_3 \frac{\partial Cov_{fn}(\boldsymbol{r})}{\partial r} \qquad \text{Eq. C 44}$$

$$\frac{\partial Cov_{\alpha h}(\boldsymbol{r})}{\partial \boldsymbol{r}^2} - a_2 \frac{\partial Cov_{\alpha h}(\boldsymbol{r})}{\partial \boldsymbol{r}} = \frac{\partial Cov_{f\alpha}(-\boldsymbol{r})}{\partial \boldsymbol{r}} - a_1 \frac{\partial Cov_{\alpha}(\boldsymbol{r})}{\partial \boldsymbol{r}} - a_3 \frac{\partial Cov_{\alpha n}(\boldsymbol{r})}{\partial \boldsymbol{r}} \qquad \text{Eq. C 45}$$

$$\frac{\partial Cov_{nh}(\boldsymbol{r})}{\partial \boldsymbol{r}^2} - a_2 \frac{\partial Cov_{nh}(\boldsymbol{r})}{\partial \boldsymbol{r}} = -\frac{\partial Cov_{fn}(-\boldsymbol{r})}{\partial \boldsymbol{r}} - a_1 \frac{\partial Cov_{\alpha n}(-\boldsymbol{r})}{\partial \boldsymbol{r}} - a_3 \frac{\partial Cov_{n}(\boldsymbol{r})}{\partial \boldsymbol{r}} \qquad \text{Eq. C 46}$$

We assume that the hydraulic parameters can be described as a second-order stationary random variable using an exponential function:

$$Cov_V(\boldsymbol{r}) = \sigma_V^2 \exp\left(-\frac{|\boldsymbol{r}|}{\rho_V}\right) \qquad \text{Eq. C 47}$$

where V signifies one of the hydraulic parameters (i.e. θ_s, α, n, and $Y=ln(K_s)$), σ_V^2 is the variance, and ρ_V is the correlation length. We only considered a vertical domain, and to keep

things simple, we assumed that the VGM parameters are uncorrelated. This strongly simplifies Eqs. A44 to A46. By using the fact that $Cov_{fh}(\boldsymbol{r}) = 0$ when **r** is close to ∞ or -∞, and integrating Eq. C 43 to Eq. C 46 using Eq. C 47, the following expressions were derived by *Zhang et al.* [1998]:

$$Cov_{fh}(\boldsymbol{r}) = \frac{\sigma_f^2 \rho_f}{1 - {a_2}^2 {\rho_f}^2}\left\{2H(\boldsymbol{r})\exp(-a_2|\boldsymbol{r}|) - \left[2H(\boldsymbol{r}) - 1 + a_2\rho_f\right]\exp(-\frac{|\boldsymbol{r}|}{\rho_f})\right\} \quad \text{Eq. C 48}$$

$$Cov_{\alpha h}(\boldsymbol{r}) = \frac{a_1\sigma_\alpha^2 \rho_\alpha}{1 - {a_2}^2 {\rho_\alpha}^2}\left\{2H(\boldsymbol{r})\exp(-a_2|\boldsymbol{r}|) - [2H(\boldsymbol{r}) - 1 + a_2\rho_\alpha]\exp(-\frac{|\boldsymbol{r}|}{\rho_\alpha})\right\} \quad \text{Eq. C 49}$$

$$Cov_{nh}(\boldsymbol{r}) = \frac{a_3\sigma_n^2 \rho_n}{1 - {a_2}^2 {\rho_n}^2}\left\{2H(\boldsymbol{r})\exp(-a_2|\boldsymbol{r}|) - [2H(\boldsymbol{r}) - 1 + a_2\rho_n]\exp(-\frac{|\boldsymbol{r}|}{\rho_n})\right\} \quad \text{Eq. C 50}$$

$$\begin{aligned} Cov_h(\boldsymbol{r}) = {} & \frac{\sigma_f^2 \rho_f}{1 - {a_2}^2 {\rho_f}^2}\left[\exp\left(-\frac{a_2|\boldsymbol{r}|}{a_2}\right) - \rho_f \exp\left(-\frac{|\boldsymbol{r}|}{\rho_f}\right)\right] \\ & + \frac{a_1\sigma_\alpha^2 \rho_\alpha}{1 - {a_2}^2 {\rho_\alpha}^2}\left[\exp\left(-\frac{a_2|\boldsymbol{r}|}{a_2}\right) - \rho_\alpha \exp\left(-\frac{|\boldsymbol{r}|}{\rho_\alpha}\right)\right] \\ & + \frac{a_3\sigma_n^2 \rho_n}{1 - {a_2}^2 {\rho_n}^2}\left[\exp\left(-\frac{a_2|\boldsymbol{r}|}{a_2}\right) - \rho_n \exp\left(-\frac{|\boldsymbol{r}|}{\rho_n}\right)\right] \end{aligned} \quad \text{Eq. C 51}$$

where $H(\boldsymbol{r})$ is the Heaviside function: $H(\boldsymbol{r}) = \begin{cases} 0, & \boldsymbol{r} < 0 \\ 1, & \boldsymbol{r} \geq 0 \end{cases}$, and a_1 to a_3 are as defined above (Eq. C 48 to Eq. C 50). By substituting the covariance of pressure head and the hydraulic parameters expressed in Eq. C 48 to Eq. C 50 into Eq. C 26 and setting $\boldsymbol{r} = 0$, an expression can be derived for the variance of soil water content (σ_θ^2):

$$\begin{aligned} \sigma_\theta^2 = {b_0}^2 \Bigg\{ & {b_1}^2\sigma_\alpha^2 + {b_2}^2\left[\frac{\sigma_f^2\rho_f}{(1 + a_2\rho_f)a_2} + \frac{a_1\sigma_\alpha^2\rho_\alpha}{(1 + a_2\rho_\alpha)a_2} + \frac{a_3\sigma_n^2\rho_n}{(1 + a_2\rho_n)a_2}\right] \\ & + {b_3}^2\sigma_n^2 + {b_4}^2\sigma_{\theta_s}^2 + 2b_1b_2\left(-\frac{a_1\sigma_\alpha^2\rho_\alpha}{1 + a_2\rho_\alpha}\right) \\ & + 2b_2b_3\left(-\frac{a_3\sigma_n^2\rho_n}{1 + a_2\rho_n}\right)\Bigg\} \end{aligned} \quad \text{Eq. C 52}$$

where b_0 to b_4 are as defined above (Eq. C 21 to Eq. C 25), and a_1 to a_3 are as defined above (Eq. C 37 to Eq. C 39). This closed-form expression for $\sigma_\theta^2(\langle h \rangle)$ shows that the variance of soil water content is a function of the mean (i.e. $<\theta_s>$, $<ln(K_s)>$, $<\alpha>$, and $<n>$), the standard deviation (i.e. $\sigma(\theta_s)$, $\sigma(\ln(K_s))$, $\sigma(\alpha)$, and $\sigma(n)$), and the vertical correlation length (i.e. $\rho_{\ln(Ks)}$, ρ_α, and ρ_n) of the VGM model parameters.

In order to assess the importance of the pressure head fluctuations that result from flow in the heterogeneous soil profiles, we also calculated σ_θ for h'=0 (i.e. assuming that the system has the same pressure head everywhere). We start this derivation from Eq. C 16 by setting h'=0. This results in:

$$\theta' = b_0[b_1\alpha' + b_3 n' + b_4 {\theta_s}'] \qquad \text{Eq. C 53}$$

where b_0 to b_4 are as defined above (Eq. C 21 to Eq. C 25). Following the same method as used to derive Eq. C 26, the covariance between θ_α and θ_β can now be expressed as:

$$\begin{aligned} Cov_\theta(r) = {b_0}^2\{ & {b_1}^2 Cov_\alpha(\boldsymbol{r}) + {b_3}^2 Cov_n(\boldsymbol{r}) \\ & + {b_4}^2 Cov_{\theta_s}(\boldsymbol{r}) + b_1 b_3[Cov_{\alpha n}(\boldsymbol{r}) + Cov_{\alpha n}(-\boldsymbol{r})] \\ & + b_1 b_4\left[Cov_{\alpha\theta_s}(\boldsymbol{r}) + Cov_{\alpha\theta_s}(-\boldsymbol{r})\right] \\ & + b_3 b_4\left[Cov_{n\theta_s}(\boldsymbol{r}) + Cov_{\alpha n}(-\boldsymbol{r})\right]\Big\} \end{aligned} \qquad \text{Eq. C 54}$$

By assuming that the VGM parameters are uncorrelated and setting $\boldsymbol{r}$=0, $\sigma_{\theta_e}^2$ can be expressed as follows when h'=0:

$$\sigma_\theta^2 = {b_0}^2\{{b_1}^2\sigma_\alpha^2 + {b_3}^2\sigma_n^2 + {b_4}^2\sigma_{\theta_s}^2\} \qquad \text{Eq. C 55}$$

where b_0 to b_4 are as defined above (Eq. C 21 to Eq. C 25). This equation shows that the variance of soil water content is only related to the variance of VGM parameters (α, n, and θ_s) if we ignore the effect of perturbation of pressure head (h'=0).

Acknowledgements

I would like to sincerely thank my supervisor, Prof. Harry Vereecken (director of IBG-3) and Dr. Heye Bogena for the guidance, discussion and all the various possibilities. I will always be grateful to you and your support. I would very much like to thank Prof. Bernd Diekkrüger in the University of Bonn (Department of Geography) for serving as co-supervisor. Furthermore, thanks to Prof. Johan Alexander Huisman for the fruitful discussions, for his intelligence, patience and kindness, when I just dropped in and long-lasting engagement and support.

A deep bow to my colleagues in IBG-3, this work would not have been possible without all your support. In particular, I am grateful to Ansgar Weuthen and Bernd Schilling for always being motivated to help me whether in the laboratory or in the field, and the deployment and maintenance of the network would not have been possible without the knowledge and commitment of them. Furthermore, I would like to thank Ansgar Weuthen, Bernd Schilling, Henning Schiedung, and Rainer Harms for all their hard work during the deployment of the SoilNet. And a special thanks goes to Ulrike Rosenbaum for the explanations and helpings of the calibration work at the beginning of my PhD.

As extraordinary experience, both personal and professional, emerged my stay abroad for three months in USDA. Therefore, I would like to express my gratitude to Prof. Yakov Pachepsky and postdoc Gonzalo Martínez in the Environmental Microbial and Food Safety Lab in USDA for their valuable ideas, support and unexpected time that they spend on my topic.

I would to thank the scholarship of CSC for the finical support of my life in Germany in the last three years. And I would also like to thank the German Research Foundation (DFG) for funding of the SFB 32 (Transregional Collaborative Research Centre) for support my work. Moreover, I thank the people of TERENO (Terrestrial Environmental Observatories), and the graduate school of TR32 for further support.

I am deeply grateful to the persons who supported me beyond the professional level. I'd like to thank my office colleges Betiglu, Katrin, Markus, Sayeh, and Sebastian for the growing friendship, not only sharing my happiness, also listen my complaint. I thank the people in the lunch group for talks and jokes during lunch time and all the support of other colleges, in particular Roland, Dorina, Anja, Maria, Inge, Hanna, Katrina, Michael, Sadam, Steffen, Sep, and there are still a lot of people to name, I can only say you know who you are and I am so fortunate you are in my life. A special thanks to all my Chinese colleges, Canlan, Yan, Xujun, Zhufeng, Shurong, Gaochao, and still so many people to name, for celebrate the Chinese festivals and share the traditional food, I feel less homesick to hang up with you.

Last but not least, thanks to the family of my landlady for taking care of me in the last few years. Thanks to my dear, Hongbin, who always believe me and encourage me during the hard time at work. In particular, I am grateful to my family for never complaining about being busy and far away from them. And thanks so much to my parents for support me all the time.

References

Abramowitz, M., Stegun, I. A. (1970), Handbook of Mathematical Functions with Formulas, Graphs, and Mathematical Tables, New York: Dover Publications, Ninth printing.

Ali, M., Montzka, C., Stadler, A., Menz, G., Vereecken, H., 2013. Estimation and validation of leaf area index time series for crops on 5m scale from space. International geosciences and remote Sensing Symposium (IGARSS), Melbourne, Australia, 21-26 July 2013.

Albertson, J. D., and Montaldo, N., 2003, Temporal dynamics of soil moisture variability: 1. Theoretical basis: Water Resources Research, v. 39, no. 10.

Angulo-Jaramillo, R., Vandervaere, J. P., Roulier, S., Thony, J. L., Gaudet, J. P., and Vauclin, M., 2000, Field measurement of soil surface hydraulic properties by disc and ring infiltrometers - a review and recent developments: Soil & Tillage Research, v. 55, no. 1-2, p. 1-29.

Arora, V. K., 2001, Assessment of simulated water balance for continental-scale river basins in an amip 2 simulation: Journal of Geophysical Research-Atmospheres, v. 106, no. D14, p. 14827-14842.

Assouline, S., Narkis, K., Tyler, S. W., Lunati, I., Parlange, M. B., and Selker, J. S., 2010, On the diurnal soil water content dynamics during evaporation using dielectric methods: Vadose Zone Journal, v. 9, no. 3, p. 709-718.

Avila, L. F., de Mello, C. R., and da Silva, A. M., 2010, Temporal stability of soil moisture under three soil uses in a catchment of the mantiqueira range region, minas gerais state, brazil: Revista Brasileira De Ciencia Do Solo, v. 34, no. 6, p. 2001-2009.

Baroni, G., Ortuani, B., Facchi, A., and Gandolfi, C., 2013, The role of vegetation and soil properties on the spatio-temporal variability of the surface soil moisture in a maize-cropped field: Journal of Hydrology, v. 489, p. 148-159.

Bauer, J., Weihermueller, L., Huisman, J. A., Herbst, M., Graf, A., Sequaris, J. M., and Vereecken, H., 2012, Inverse determination of heterotrophic soil respiration response to temperature and water content under field conditions: Biogeochemistry, v. 108, no. 1-3, p. 119-134.

Bansal, R. K. (2006). New Approach to CBSE Mathematics IX. Laxmi Publications. p. 25. ISBN 978-81-318-0013-3.

Betts, A. K., Ball, J. H., Beljaars, A. C. M., Miller, M. J., and Viterbo, P. A., 1996, The land surface-atmosphere interaction: A review based on observational and global modeling perspectives: Journal of Geophysical Research-Atmospheres, v. 101, no. D3, p. 7209-7225.

Birchak, J. R., Gardner, C. G., Hipp, J. E., and Victor, J. M., 1974, High dielectric constant microwave probes for sensing soil moisture: Proceedings of the Ieee, v. 62, no. 1, p. 93-98.

Biswas, A., and Si, B. C., 2011, Revealing the controls of soil water storage at different scales in a hummocky landscape: Soil Science Society of America Journal, v. 75, no. 4, p. 1295-1306.

Bittelli, M., 2011, Measuring soil water content: A review: Horttechnology, v. 21, no. 3, p. 293-300.

Blonquist, J. M., Jones, S. B., and Robinson, D. A., 2005a, Standardizing characterization of electromagnetic water content sensors: Part 2. Evaluation of seven sensing systems: Vadose Zone Journal, v. 4, no. 4, p. 1059-1069.

Blonquist, J. M., Jones, S. B., and Robinson, D. A., 2005b, A time domain transmission sensor with tdr performance characteristics: Journal of Hydrology, v. 314, no. 1-4, p. 235-245.

Bogena, H., Kunkel, R., Pütz, T., Vereecken, H., Krüger, E., Zacharias, S., Dietrich, P., Wollschläger, U., Kunstmann, H., Papen, H., Schmid, H. P., and Munch, J. C., 2012, Tereno – long-term monitoring network for terrestrial research: Hydrologie und Wasserbewirtschaftung, v. 56, no. 3, p. 138-143.

Bogena, H. R., Herbst, M., Huisman, J. A., Rosenbaum, U., Weuthen, A., and Vereecken, H., 2010, Potential of wireless sensor networks for measuring soil water content variability: Vadose Zone Journal, v. 9, no. 4, p. 1002-1013.

Bogena, H. R., Huisman, J. A., Meier, H., Rosenbaum, U., and Weuthen, A., 2009, Hybrid wireless underground sensor networks: Quantification of signal attenuation in soil: Vadose Zone Journal, v. 8, no. 3, p. 755-761.

Bogena, H. R., Huisman, J. A., Oberdoerster, C., and Vereecken, H., 2007, Evaluation of a low-cost soil water content sensor for wireless network applications: Journal of Hydrology, v. 344, no. 1-2, p. 32-42.

Bonan, G. B., Pollard, D., and Thompson, S. L., 1993, Influence of subgrid-scale heterogeneity in leaf-area index, stomatal-resistance, and soil-moisture on grid-scale land-atmosphere interactions: Journal of Climate, v. 6, no. 10, p. 1882-1897.

Brocca, L., Melone, F., Moramarco, T., and Morbidelli, R., 2009, Soil moisture temporal stability over experimental areas in central italy: Geoderma, v. 148, no. 3-4, p. 364-374.

Campbell, J. E., 1990, Dielectric-properties and influence of conductivity in soils at on to 50 megahertz: Soil Science Society of America Journal, v. 54, no. 2, p. 332-341.

Carsel, R. F., and Parrish, R. S., 1988, Developing joint probability-distributions of soil-water retention characteristics: Water Resources Research, v. 24, no. 5, p. 755-769.

Cassel, D. K., Wendroth, O., and Nielsen, D. R., 2000, Assessing spatial variability in an agricultural experiment station field: Opportunities arising from spatial dependence: Agronomy Journal, v. 92, no. 4, p. 706-714.

Castillo, V. M., Gomez-Plaza, A., and Martinez-Mena, M., 2003, The role of antecedent soil water content in the runoff response of semiarid catchments: A simulation approach: Journal of Hydrology, v. 284, no. 1-4, p. 114-130.

Choi, M., and Jacobs, J. M., 2007, Soil moisture variability of root zone profiles within smex02 remote sensing footprints: Advances in Water Resources, v. 30, no. 4, p. 883-896.

Cosh, M. H., Jackson, T. J., Bindlish, R., and Prueger, J. H., 2004, Watershed scale temporal and spatial stability of soil moisture and its role in validating satellite estimates: Remote Sensing of Environment, v. 92, no. 4, p. 427-435.

Cosh, M. H., Jackson, T. J., Moran, S., and Bindlish, R., 2008, Temporal persistence and stability of surface soil moisture in a semi-arid watershed: Remote Sensing of Environment, v. 112, no. 2, p. 304-313.

Cosh, M. H., Jackson, T. J., Starks, P., and Heathman, G., 2006, Temporal stability of surface soil moisture in the little washita river watershed and its applications in satellite soil moisture product validation: Journal of Hydrology, v. 323, no. 1-4, p. 168-177.

Crow, W. T., Ryu, D., and Famiglietti, J. S., 2005, Upscaling of field-scale soil moisture measurements using distributed land surface modeling: Advances in Water Resources, v. 28, no. 1, p. 1-14.

Dorigo, W. A., Xaver, A., Vreugdenhil, M., Gruber, A., Hegyiova, A., Sanchis-Dufau, A. D., Zamojski, D., Cordes, C., Wagner, W., and Drusch, M., 2013, Global automated quality control of in situ soil moisture data from the international soil moisture network: Vadose Zone Journal, v. 12, no. 3.

Duan, Q. Y., Sorooshian, S., and Gupta, V., 1992, Effective and efficient global optimization for conceptual rainfall-runoff models: Water Resources Research, v. 28, no. 4, p. 1015-1031.

Eltahir, E. A. B., 1998, A soil moisture rainfall feedback mechanism 1. Theory and observations: Water Resources Research, v. 34, no. 4, p. 765-776.

Famiglietti, J. S., Devereaux, J. A., Laymon, C. A., Tsegaye, T., Houser, P. R., Jackson, T. J., Graham, S. T., Rodell, M., and van Oevelen, P. J., 1999, Ground-based investigation of soil moisture variability within remote sensing footprints during the southern great plains

1997 (sgp97) hydrology experiment: Water Resources Research, v. 35, no. 6, p. 1839-1851.

Famiglietti, J. S., Rudnicki, J. W., and Rodell, M., 1998, Variability in surface moisture content along a hillslope transect: Rattlesnake hill, texas: Journal of Hydrology, v. 210, no. 1-4, p. 259-281.

Famiglietti, J. S., Ryu, D., Berg, A. A., Rodell, M., and Jackson, T. J., 2008, Field observations of soil moisture variability across scales: Water Resources Research, v. 44, no. 1.

Farber, O., and Kadmon, R., 2003, Assessment of alternative approaches for bioclimatic modeling with special emphasis on the mahalanobis distance: Ecological Modelling, v. 160, no. 1-2, p. 115-130.

Feddes, R. A., Kowalik, P., Kolinskamalinka, K., and Zaradny, H., 1976, Simulation of field water-uptake by plants using a soil-water dependent root extraction function: Journal of Hydrology, v. 31, no. 1-2, p. 13-26.

Fredlund, D. G., 2000, The 1999 r.M. Hardy lecture: The implementation of unsaturated soil mechanics into geotechnical engineering: Canadian Geotechnical Journal, v. 37, no. 5, p. 963-986.

Gao, L., and Shao, M., 2012, Temporal stability of shallow soil water content for three adjacent transects on a hillslope: Agricultural Water Management, v. 110, p. 41-54.

Garcia-Estringana, P., Latron, J., Llorens, P., and Gallart, F., 2013, Spatial and temporal dynamics of soil moisture in a mediterranean mountain area (vallcebre, ne spain): Ecohydrology, v. 6, no. 5, p. 741-753.

Gedney, N., and Cox, P. M., 2003, The sensitivity of global climate model simulations to the representation of soil moisture heterogeneity: Journal of Hydrometeorology, v. 4, no. 6, p. 1265-1275.

Gomez-Plaza, A., Martinez-Mena, M., Albaladejo, J., and Castillo, V. M., 2001, Factors regulating spatial distribution of soil water content in small semiarid catchments: Journal of Hydrology, v. 253, no. 1-4, p. 211-226.

Grayson, R. B., and Western, A. W., 1998, Towards areal estimation of soil water content from point measurements: Time and space stability of mean response: Journal of Hydrology, v. 207, no. 1-2, p. 68-82.

Guber, A. K., Gish, T. J., Pachepsky, Y. A., Van Genuchten, M. T., Daughtry, C. S. T., Nicholson, T. J., and Cady, R. E., 2008, Temporal stability in soil water content patterns across agricultural fields: Catena, v. 73, no. 1, p. 125-133.

Heathman, G. C., Larose, M., Cosh, M. H., and Bindlish, R., 2009, Surface and profile soil moisture spatio-temporal analysis during an excessive rainfall period in the southern great plains, USA: Catena, v. 78, no. 2, p. 159-169.

Heathman, G. C., Starks, P. J., Ahuja, L. R., and Jackson, T. J., 2003, Assimilation of surface soil moisture to estimate profile soil water content: Journal of Hydrology, v. 279, no. 1-4, p. 1-17.

Heimovaara, T. J., and Bouten, W., 1990, A computer-controlled 36-channel time domain reflectometry system for monitoring soil-water contents: Water Resources Research, v. 26, no. 10, p. 2311-2316.

Heuvelink, G. B. M., and Webster, R., 2001, Modelling soil variation: Past, present, and future: Geoderma, v. 100, no. 3-4, p. 269-301.

Hu, W., Shao, M., Han, F., Reichardt, K., and Tan, J., 2010a, Watershed scale temporal stability of soil water content: Geoderma, v. 158, no. 3-4, p. 181-198.

Hu, W., Shao, M., and Reichardt, K., 2010b, Using a new criterion to identify sites for mean soil water storage evaluation: Soil Science Society of America Journal, v. 74, no. 3, p. 762-773.

Hu, Z. L., and Islam, S., 1998, Effects of subgrid-scale heterogeneity of soil wetness and temperature on grid-scale evaporation and its parametrization: International Journal of Climatology, v. 18, no. 1, p. 49-63.

Hübner, C., Cardell-Oliver, R., Becker, R., Spohrer, K., Jotter, K., and Wagenknecht, T., 2009, Wireless soil moisture sensor networks for environmental monitoring and vineyard irrigation: Helsinki University of Technology, no. 1, p. 408-415.

Hupet, F., and Vanclooster, M., 2002, Intraseasonal dynamics of soil moisture variability within a small agricultural maize cropped field: Journal of Hydrology, v. 261, no. 1-4, p. 86-101.

IMGERS, 1979, Inner Mongolia Grassland Ecosystem Research Station (IMGERS), http://imk-ifu.fzk.de/355.php.

Jacobs, J. M., Mohanty, B. P., Hsu, E. C., and Miller, D., 2004, Smex02: Field scale variability, time stability and similarity of soil moisture: Remote Sensing of Environment, v. 92, no. 4, p. 436-446.

Jawson, S. D., and Niemann, J. D., 2007, Spatial patterns from eof analysis of soil moisture at a large scale and their dependence on soil, land-use, and topographic properties: Advances in Water Resources, v. 30, no. 3, p. 366-381.

Jensen, D. T., Hargreaves, G. H., Temesgen, B., and Allen, R. G., 1997, Computation of eto under nonideal conditions: Journal of Irrigation and Drainage Engineering-Asce, v. 123, no. 5, p. 394-400.

Jones, S. B., Blonquist, J. M., Robinson, D. A., Rasmussen, V. P., and Or, D., 2005, Standardizing characterization of electromagnetic water content sensors: Part 1. Methodology: Vadose Zone Journal, v. 4, no. 4, p. 1048-1058.

Kaatze, U., and Huebner, C., 2010, Electromagnetic techniques for moisture content determination of materials: Measurement Science & Technology, v. 21, no. 8.

Kaatze, U., Kettler, M., and Pottel, R., 1996, Dielectric relaxation spectrometry of mixtures of water with isopropoxy- and isobutoxyethanol. Comparison to unbranched poly(ethylene glycol) monoalkyl ethers: Journal of Physical Chemistry, v. 100, no. 6, p. 2360-2366.

Kamgar, A., Hopmans, J. W., Wallender, W. W., and Wendroth, O., 1993, Plotsize and sample number for neutron probe measurements in small-field trials: Soil Science, v. 156, no. 4, p. 213-224.

Kelleners, T. J., Robinson, D. A., Shouse, P. J., Ayars, J. E., and Skaggs, T. H., 2005, Frequency dependence of the complex permittivity and its impact on dielectric sensor calibration in soils: Soil Science Society of America Journal, v. 69, no. 1, p. 67-76.

Kim, C. P., and Stricker, J. N. M., 1996, Influence of spatially variable soil hydraulic properties and rainfall intensity on the water budget: Water Resources Research, v. 32, no. 6, p. 1699-1712.

Kizito, F., Campbell, C. S., Campbell, G. S., Cobos, D. R., Teare, B. L., Carter, B., and Hopmans, J. W., 2008, Frequency, electrical conductivity and temperature analysis of a low-cost capacitance soil moisture sensor: Journal of Hydrology, v. 352, no. 3-4, p. 367-378.

Korres, W., Koyama, C. N., Fiener, P., and Schneider, K., 2010, Analysis of surface soil moisture patterns in agricultural landscapes using empirical orthogonal functions: Hydrology and Earth System Sciences, v. 14, no. 5, p. 751-764.

Martinez, G., Pachepsky, Y. A., and Vereecken, H., 2014, Temporal stability of soil water content as affected by climate and soil hydraulic properties: A simulation study.: Hydrological Processes, v. 28, p. 1899–1915.

Martinez, G., Pachepsky, Y. A., Vereecken, H., Hardelauf, H., Herbst, M., and Vanderlindend, K., 2013, Modeling local control effects on the temporal stability of soil water content: Journal of Hydrology, v. 481, p. 106–118.

Martinez, G., Vanderlinden, K., Giraldez, J. V., Espejo, A. J., and Muriel, J. L., 2010, Field-scale soil moisture pattern mapping using electromagnetic induction: Vadose Zone Journal, v. 9, no. 4, p. 871-881.

McCready, M. S., Dukes, M. D., and Miller, G. L., 2009, Water conservation potential of smart irrigation controllers on st. Augustinegrass: Agricultural Water Management, v. 96, no. 11, p. 1623-1632.

Mermoud, A., and Xu, D., 2006, Comparative analysis of three methods to generate soil hydraulic functions: Soil & Tillage Research, v. 87, no. 1, p. 89-100.

Mertens, J., Madsen, H., Feyen, L., Jacques, D., and Feyen, J., 2004, Including prior information in the estimation of effective soil parameters in unsaturated zone modelling: Journal of Hydrology, v. 294, no. 4, p. 251-269.

Mittelbach, H., and Seneviratne, S. I., 2012, A new perspective on the spatio-temporal variability of soil moisture: Temporal dynamics versus time-invariant contributions: Hydrology and Earth System Sciences, v. 16, no. 7, p. 2169-2179.

Mohanty, B. P., and Skaggs, T. H., 2001, Spatio-temporal evolution and time-stable characteristics of soil moisture within remote sensing footprints with varying soil, slope, and vegetation: Advances in Water Resources, v. 24, no. 9-10, p. 1051-1067.

Montaldo, N., and Albertson, J. D., 2003, Temporal dynamics of soil moisture variability: 2. Implications for land surface models: Water Resources Research, v. 39, no. 10.

Montzka, C., Bogena, H., Weihermueller, L., Jonard, F., Dimitrov, M., Bouzinac, C., Kainulainen, J., Balling, J. E., Vanderborght, J., Vereecken, H., and Ieee, 2011, Radiobrighteness validation on different spatial scales during the smos validation campaing 2010 in the rur catchment, germany, 2011 ieee international geoscience and remote sensing symposium, 3760-3763 p.:

Montzka, C., Bogena, H. R., Weihermuller, L., Jonard, F., Bouzinac, C., Kainulainen, J., Balling, J. E., Loew, A., Dall'Amico, J. T., Rouhe, E., Vanderborght, J., and Vereecken, H., 2013, Brightness temperature and soil moisture validation at different scales during the smos validation campaign in the rur and erft catchments, germany: Ieee Transactions on Geoscience and Remote Sensing, v. 51, no. 3, p. 1728-1743.

Myneni, R. B., Nemani, R. R., and Running, S. W., 1997, Estimation of global leaf area index and absorbed par using radiative transfer models: Ieee Transactions on Geoscience and Remote Sensing, v. 35, no. 6, p. 1380-1393.

Noborio, K., 2001, Measurement of soil water content and electrical conductivity by time domain reflectometry: A review: Computers and Electronics in Agriculture, v. 31, no. 3, p. 213-237.

Oldak, A., Jackson, T. J., and Pachepsky, Y., 2002, Using gis in passive microwave soil moisture mapping and geostatistical analysis: International Journal of Geographical Information Science, v. 16, no. 7, p. 681-698.

Or, D., and Wraith, J. M., 1999, Temperature effects on soil bulk dielectric permittivity measured by time domain reflectometry: A physical model (vol 35, pg 371, 1999): Water Resources Research, v. 35, no. 7, p. 2283-2283.

Pachepsky, Y. A., Guber, A. K., and Jacques, D., 2005, Temporal persistence in vertical distributions of soil moisture contents: Soil Science Society of America Journal, v. 69, no. 2, p. 347-352.

Pachepsky, Y. A., Rawls, W. J., and Lin, H. S., 2006, Hydropedology and pedotransfer functions: Geoderma, v. 131, no. 3-4, p. 308-316.

Pan, F., Pachepsky, Y., Jacques, D., Guber, A., and Hill, R. L., 2012, Data assimilation with soil water content sensors and pedotransfer functions in soil water flow modeling: Soil Science Society of America Journal, v. 76, no. 3, p. 829-844.

Pearson, R., 2011, Exploring data in engineering, the sciences, and medicine: OXFORD University Press, p. 275-327.

Pepin, S., Livingston, N. J., and Hook, W. R., 1995, Temperature dependent measurement errors in time-domain reflectometry determinations of soil water: Soil Science Society of America Journal, v. 59, no. 1, p. 38-43.

Perry, M. A., and Niemann, J. D., 2007, Analysis and estimation of soil moisture at the catchment scale using eofs: Journal of Hydrology, v. 334, no. 3-4, p. 388-404.

Qu, W., Bogena, H. R., Huisman, J. A., and Vereecken, H., 2013, Calibration of a novel low-cost soil water content sensor based on a ring oscillator: Vadose Zone Journal, v. 12, no. 2.

Ratliff, L. F., Ritchie, J. T., and Cassel, D. K., 1983, Field-measured limits of soil-water availability as related to laboratory-measured properties: Soil Science Society of America Journal, v. 47, no. 4, p. 770-775.

Reynolds, S. G., 1970, The gravimetric method of soil moisture determination part iii an examination of factors influencing soil moisture variability: Journal of Hydrology, v. 11, p. 13.

Ritter, A., Hupet, F., Munoz-Carpena, R., Lambot, S., and Vanclooster, M., 2003, Using inverse methods for estimating soil hydraulic properties from field data as an alternative to direct methods: Agricultural Water Management, v. 59, no. 2, p. 77-96.

Robinson, D. A., 2004, Measurement of the solid dielectric permittivity of clay minerals and granular samples using a time domain reflectometry immersion method: Vadose Zone Journal, v. 3, no. 2, p. 705-713.

Robinson, D. A., Campbell, C. S., Hopmans, J. W., Hornbuckle, B. K., Jones, S. B., Knight, R., Ogden, F., Selker, J., and Wendroth, O., 2008, Soil moisture measurement for ecological and hydrological watershed-scale observatories: A review: Vadose Zone Journal, v. 7, no. 1, p. 358-389.

Robinson, D. A., and Friedman, S. P., 2003, A method for measuring the solid particle permittivity or electrical conductivity of rocks, sediments, and granular materials: Journal of Geophysical Research-Solid Earth, v. 108, no. B2.

Robinson, D. A., Gardner, C. M. K., and Cooper, J. D., 1999, Measurement of relative permittivity in sandy soils using tdr, capacitance and theta probes: Comparison, including the effects of bulk soil electrical conductivity: Journal of Hydrology, v. 223, no. 3-4, p. 198-211.

Robinson, D. A., Jones, S. B., Blonquist, J. M., and Friedman, S. P., 2005a, A physically derived water content/permittivity calibration model for coarse-textured, layered soils: Soil Science Society of America Journal, v. 69, no. 5, p. 1372-1378.

Robinson, D. A., Jones, S. B., Wraith, J. M., Or, D., and Friedman, S. P., 2003, A review of advances in dielectric and electrical conductivity measurement in soils using time domain reflectometry: Vadose Zone Journal, v. 2, no. 4, p. 444-475.

Robinson, D. A., Kelleners, T. J., Cooper, J. D., Gardner, C. M. K., Wilson, P., Lebron, I., and Logsdon, S., 2005b, Evaluation of a capacitance probe frequency response model accounting for bulk electrical conductivity: Comparison with tdr and network analyzer measurements: Vadose Zone Journal, v. 4, no. 4, p. 992-1003.

Ronda, R. J., van den Hurk, B., and Holtslag, A. A. M., 2002, Spatial heterogeneity of the soil moisture content and its impact on surface flux densities and near-surface meteorology: Journal of Hydrometeorology, v. 3, no. 5, p. 556-570.

Rosenbaum, U., Bogena, H. R., Herbst, M., Huisman, J. A., Peterson, T. J., Weuthen, A., Western, A. W., and Vereecken, H., 2012, Seasonal and event dynamics of spatial soil moisture patterns at the small catchment scale: Water Resources Research, v. 48.

Rosenbaum, U., Huisman, J. A., Vrba, J., Vereecken, H., and Bogena, H. R., 2011, Correction of temperature and electrical conductivity effects on dielectric permittivity measurements with ech2o sensors: Vadose Zone Journal, v. 10, no. 2, p. 582-593.

Rosenbaum, U., Huisman, J. A., Weuthen, A., Vereecken, H., and Bogena, H. R., 2010, Sensor-to-sensor variability of the ech2o ec-5, te, and 5te sensors in dielectric liquids: Vadose Zone Journal, v. 9, no. 1, p. 181-186.

Roth, K., 1995, Steady-state flow in an unsaturated, 2-dimensional, macroscopically homogeneous, miller-similar medium: Water Resources Research, v. 31, no. 9, p. 2127-2140.

Ryu, D., and Famiglietti, J. S., 2005, Characterization of footprint-scale surface soil moisture variability using gaussian and beta distribution functions during the southern great plains 1997 (sgp97) hydrology experiment: Water Resources Research, v. 41, no. 12.

Sakaki, T., Limsuwat, A., Smits, K. M., and Illangasekare, T. H., 2008, Empirical two-point alpha-mixing model for calibrating the ech2o ec-5 soil moisture sensor in sands: Water Resources Research, v. 44.

Schaap, M. G., and Leij, F. J., 1998, Database-related accuracy and uncertainty of pedotransfer functions: Soil Science, v. 163, no. 10, p. 765-779.

Schaap, M. G., Leij, F. J., and van Genuchten, M. T., 2001, Rosetta: A computer program for estimating soil hydraulic parameters with hierarchical pedotransfer functions: Journal of Hydrology, v. 251, no. 3-4, p. 163-176.

Scharnagl, B., Vrugt, J. A., Vereecken, H., and Herbst, M., 2011, Inverse modelling of in situ soil water dynamics: Investigating the effect of different prior distributions of the soil hydraulic parameters: Hydrology and Earth System Sciences, v. 15, no. 10, p. 3043-3059.

Schneider, K., Huisman, J. A., Breuer, L., and Frede, H. G., 2008a, Ambiguous effects of grazing intensity on surface soil moisture: A geostatistical case study from a steppe environment in inner mongolia, pr china: Journal of Arid Environments, v. 72, no. 7, p. 1305-1319.

Schneider, K., Huisman, J. A., Breuer, L., Zhao, Y., and Frede, H. G., 2008b, Temporal stability of soil moisture in various semi-arid steppe ecosystems and its application in remote sensing: Journal of Hydrology, v. 359, no. 1-2, p. 16-29.

Schneider, K., Leopold, U., Gerschlauer, F., Barthold, F., Giese, M., Steffens, M., Hoffmann, C., Frede, H.-G., and Breuer, L., 2011, Spatial and temporal variation of soil moisture in dependence of multiple environmental parameters in semi-arid grasslands: Plant and Soil, v. 340, no. 1-2, p. 73-88.

Schwank, M., Green, T. R., Maetzler, C., Benedickter, H., and Fluehler, H., 2006, Laboratory characterization of a commercial capacitance sensor for estimating permittivity and inferring soil water content: Vadose Zone Journal, v. 5, no. 3, p. 1048-1064.

Schwartz, R. C., Evett, S. R., Pelletier, M. G., and Bell, J. M., 2009, Complex permittivity model for time domain reflectometry soil water content sensing: I. Theory: Soil Science Society of America Journal, v. 73, no. 3, p. 886-897.

Seneviratne, S. I., Corti, T., Davin, E. L., Hirschi, M., Jaeger, E. B., Lehner, I., Orlowsky, B., and Teuling, A. J., 2010, Investigating soil moisture-climate interactions in a changing climate: A review: Earth-Science Reviews, v. 99, no. 3-4, p. 125-161.

Simunek, J., and van Genuchten, M. T., 2008, Modeling nonequilibrium flow and transport processes using hydrus: Vadose Zone Journal, v. 7, no. 2, p. 782-797.

Simunek, J., van Genuchten, M. T., and Sejna, M., 2008a, Development and applications of the hydrus and stanmod software packages and related codes: Vadose Zone Journal, v. 7, no. 2, p. 587-600.

Simunek, J., van Genuchten, M. T., and Sejna, M., 2008b, Modeling subsurface water flow and solute transport with hydrus and related numerical software packages, Numerical modelling of hydrodynamics for water resources.

Smith, S. K., Franti, T. G., and Comfort, S. D., 2002, Impact of initial soil water content, crop residue cover, and post-herbicide irrigation on herbicide runoff: Transactions of the ASAE, v. 45, no. 6, p. 1817-1824.

SoilNet, 2012, Wireless sensor network in rollesbroich: http://www.fz-juelich.de/ibg/ibg-3/EN/About%20us/Tereno/SoilNet/Applications/rollesbroich/_node.html.

Starks, P. J., Heathman, G. C., Jackson, T. J., and Cosh, M. H., 2006, Temporal stability of soil moisture profile: Journal of Hydrology, v. 324, no. 1-4, p. 400-411.

Sudduth, K. A., Drummond, S. T., and Kitchen, N. R., 2001, Accuracy issues in electromagnetic induction sensing of soil electrical conductivity for precision agriculture: Computers and Electronics in Agriculture, v. 31, no. 3, p. 239-264.

Takagi, K., and Lin, H. S., 2011, Temporal dynamics of soil moisture spatial variability in the shale hills critical zone observatory: Vadose Zone Journal, v. 10, no. 3, p. 832-842.

TERENO, 2012, Terrestrial Environmental Observatories (TERENO), http://teodoor.icg.kfa-juelich.de/.

Teuling, A. J., Hupet, F., Uijlenhoet, R., and Troch, P. A., 2007, Climate variability effects on spatial soil moisture dynamics: Geophysical Research Letters, v. 34, no. 6.

Teuling, A. J., and Troch, P. A., 2005, Improved understanding of soil moisture variability dynamics: Geophysical Research Letters, v. 32, no. 5.

Topp, G. C., Davis, J. L., and Annan, A. P., 1980, Electromagnetic determination of soil water content - measurements in coaxial transmission-lines: Water Resources Research, v. 16, no. 3, p. 574-582.

Topp, G. C., Zegelin, S., and White, I., 2000, Impacts of the real and imaginary components of relative permittivity on time domain reflectometry measurements in soils: Soil Science Society of America Journal, v. 64, no. 4, p. 1244-1252.

Vachaud, G., Desilans, A. P., Balabanis, P., and Vauclin, M., 1985, Temporal stability of spatially measured soil-water probability density-function: Soil Science Society of America Journal, v. 49, no. 4, p. 822-828.

Van Dam, R. L., Schlager, W., Dekkers, M. J., and Huisman, J. A., 2002, Iron oxides as a cause of gpr reflections: Geophysics, v. 67, no. 2, p. 536-545.

van Genuchten, M. T., 1980, A closed-form equation for predicting the hydraulic conductivity of unsaturated soils: Soil Science Society of America Journal, v. 44, no. 5, p. 892-898.

Vandam, J. C., Stricker, J. N. M., and Droogers, P., 1994, Inverse method to determine soil hydraulic functions from multistep outflow experiments: Soil Science Society of America Journal, v. 58, no. 3, p. 647-652.

Vanderlinden, K., Vereecken, H., Hardelauf, H., Herbst, M., Martinez, G., Cosh, M. H., and Pachepsky, Y. A., 2012, Temporal stability of soil water contents: A review of data and analyses: Vadose Zone Journal, v. 11, no. 4.

Vereecken, H., Huisman, J. A., Bogena, H., Vanderborght, J., Vrugt, J. A., and Hopmans, J. W., 2008, On the value of soil moisture measurements in vadose zone hydrology: A review: Water Resources Research, v. 44.

Vereecken, H., Huisman, J. A., Pachepsky, Y., Montzka, C., van der Kruk, J., Bogena, H., Weihermüller, L., Herbst, M., Martinez, G., and Vanderborght, J., 2014, On the spatio-temporal dynamics of soil moisture at the field scale: Journal of Hydrology, v. 515, p. 76-96.

Vereecken, H., Kamai, T., Harter, T., Kasteel, R., Hopmans, J., and Vanderborght, J., 2007, Explaining soil moisture variability as a function of mean soil moisture: A stochastic unsaturated flow perspective: Geophysical Research Letters, v. 34, no. 22.

Vereecken, H., Weynants, M., Javaux, M., Pachepsky, Y., Schaap, M. G., and van Genuchten, M. T., 2010, Using pedotransfer functions to estimate the van genuchten-mualem soil hydraulic properties: A review: Vadose Zone Journal, v. 9, no. 4, p. 795-820.

Vrugt, J. A., Gupta, H. V., Bouten, W., and Sorooshian, S., 2003, A shuffled complex evolution metropolis algorithm for optimization and uncertainty assessment of hydrologic model parameters: Water Resources Research, v. 39, no. 8.

Vrugt, J. A., Schoups, G., Hopmans, J. W., Young, C., Wallender, W. W., Harter, T., and Bouten, W., 2004, Inverse modeling of large-scale spatially distributed vadose zone properties using global optimization: Water Resources Research, v. 40, no. 6.

Vrugt, J. A., Stauffer, P. H., Woehling, T., Robinson, B. A., and Vesselinov, V. V., 2008, Inverse modeling of subsurface flow and transport properties: A review with new developments: Vadose Zone Journal, v. 7, no. 2, p. 843-864.

Vrugt, J. A., ter Braak, C. J. F., Diks, C. G. H., Robinson, B. A., Hyman, J. M., and Higdon, D., 2009, Accelerating markov chain monte carlo simulation by differential evolution with self-adaptive randomized subspace sampling: International Journal of Nonlinear Sciences and Numerical Simulation, v. 10, no. 3, p. 273-290.

Wagner, N., Emmerich, K., Bonitz, F., and Kupfer, K., 2011, Experimental investigations on the frequency- and temperature-dependent dielectric material properties of soil: Ieee Transactions on Geoscience and Remote Sensing, v. 49, no. 7, p. 2518-2530.

Wang, T. J., 2014, Modeling the impacts of soil hydraulic properties on temporal stability of soil moisture under a semi-arid climate: Journal of Hydrology, v. 519, p. 11.

Wang, Z., and Zhu, T., 2003, Effect of flooding disturbance on aboveground biomass of leymus chinensis grassland - a preliminary study: Yingyong Shengtai Xuebao, v. 14, no. 12, p. 2162-2166.

Weast, R. C., 1986, Handbook of physics and chemistry, v. CRC press.

Wessolek, G., Plagge, R., Leij, F. J., and Vangenuchten, M. T., 1994, Analyzing problems in describing field and laboratory measured soil hydraulic-properties: Geoderma, v. 64, no. 1-2, p. 93-110.

Western, A. W., and Grayson, R. B., 1998, The tarrawarra data set: Soil moisture patterns, soil characteristics, and hydrological flux measurements: Water Resources Research, v. 34, no. 10, p. 2765-2768.

Western, A. W., Grayson, R. B., and Bloschl, G., 2002, Scaling of soil moisture: A hydrologic perspective: Annual Review of Earth and Planetary Sciences, v. 30, p. 149-180.

Western, A. W., Zhou, S. L., Grayson, R. B., McMahon, T. A., Bloschl, G., and Wilson, D. J., 2004, Spatial correlation of soil moisture in small catchments and its relationship to dominant spatial hydrological processes: Journal of Hydrology, v. 286, no. 1-4, p. 113-134.

Williams, C. J., McNamara, J. P., and Chandler, D. G., 2009, Controls on the temporal and spatial variability of soil moisture in a mountainous landscape: The signature of snow and complex terrain: Hydrology and Earth System Sciences, v. 13, no. 7, p. 1325-1336.

Wosten, J. H. M., Lilly, A., Nemes, A., and Le Bas, C., 1999, Development and use of a database of hydraulic properties of european soils: Geoderma, v. 90, no. 3-4, p. 169-185.

Wosten, J. H. M., Pachepsky, Y. A., and Rawls, W. J., 2001, Pedotransfer functions: Bridging the gap between available basic soil data and missing soil hydraulic characteristics: Journal of Hydrology, v. 251, no. 3-4, p. 123-150.

Yoo, C., and Kim, S., 2004, Eof analysis of surface soil moisture field variability: Advances in Water Resources, v. 27, no. 8, p. 831-842.

Yu, C., Warrick, A. W., Conklin, M. H., Young, M. H., and Zreda, M., 1997, Two- and three-parameter calibrations of time domain reflectometry for soil moisture measurement: Water Resources Research, v. 33, no. 10, p. 2417-2421.

Zacharias, S., Bogena, H., Samaniego, L., Mauder, M., Fuss, R., Puetz, T., Frenzel, M., Schwank, M., Baessler, C., Butterbach-Bahl, K., Bens, O., Borg, E., Brauer, A., Dietrich, P., Hajnsek, I., Helle, G., Kiese, R., Kunstmann, H., Klotz, S., Munch, J. C., Papen, H., Priesack, E., Schmid, H. P., Steinbrecher, R., Rosenbaum, U., Teutsch, G., and Vereecken, H., 2011, A network of terrestrial environmental observatories in germany: Vadose Zone Journal, v. 10, no. 3, p. 955-973.

Zhang, D. X., Wallstrom, T. C., and Winter, C. L., 1998, Stochastic analysis of steady-state unsaturated flow in heterogeneous media: Comparison of the brooks-corey and gardner-russo models: Water Resources Research, v. 34, no. 6, p. 1437-1449.

Zhang, N. Q., Wang, M. H., and Wang, N., 2002, Precision agriculture - a worldwide overview: Computers and Electronics in Agriculture, v. 36, no. 2-3, p. 113-132.

Zhang, Z. F., Ward, A. L., and Gee, G. W., 2003, Estimating soil hydraulic parameters of a field drainage experiment using inverse techniques: Vadose Zone Journal, v. 2, no. 2, p. 201-211.

Zhao, L., Yang, K., Qin, J., Chen, Y., Tang, W., Montzka, C., Wu, H., Lin, C., Han, M., and Vereecken, H., 2013, Spatiotemporal analysis of soil moisture observations within a tibetan mesoscale area and its implication to regional soil moisture measurements: Journal of Hydrology, v. 482, p. 92-104.

Zijl, W., 1999, Scale aspects of groundwater flow and transport systems: Hydrogeology Journal, v. 7, no. 1, p. 139-150.

Publications

1. **W. Qu**, H. R. Bogena, J. A. Huisman, J. Vanderborght, M. Schuh, E. Priesack, H. Vereecken, *Predicting subgrid variability of soil water content from basic soil information*, Geophysical Research Letters, 2015, 42, 1-8.

2. **W. Qu**, H. R. Bogena, J. A. Huisman, G. Martinez, Y. A. Pachepsky, H. Vereecken, *Effects of soil hydraulic properties on the spatial variability of soil water content: evidence from sensor network data and inverse modeling*, Vadose Zone Journal, 2014, 13(12), 1-12.

3. R. Baatz, H. R. Bogena, H. J. Hendricks Franssen, J. A. Huisman, **W. Qu,** C. Montzka, H. Vereecken, *Calibration of a catchment scale cosmic-ray probe network: A comparison of three parameterization methods*, Journal of Hydrology, 2014, 516, 231–244.

4. **W. Qu,** H. R. Bogena, J. A. Huisman, H. Vereecken, *Calibration of a novel low-cost time domain transmission soil water content sensor*, Vadose Zone Journal, 2013, 12(2), 1-10.

5. F.S. Zhang, **W. Qu**, G.H. Yin, and Z.X. Liu, *Spatial pattern of surface soil organic matter based on remotely sensed multispectral image*, Chinese Journal of Applied Ecology, 2010, 21(4), 883-888.

6. **W. Qu**, Z.X. Liu, F.S. Zhang, Z.J. Kang, and Y.J. Shen, *Coupling effects of water and fertilizer on nitrogen content of maize grain*, Chinese Journal of Ecology, 2010, 29(9), 1749-1753. (In Chinese)

7. F.S. Zhang, Z.X. Liu, **W. Qu**, Z.J. Kang and Y.J. Shen, *Spatial variability of soil organic matter in long-term small scale across cultivated crop land*, Agricultural Research in the Arid Areas, 2010, 28(2), 167-171. (In Chinese)

8. Z.X. Liu, **W. Qu**, Y.G. Miao, Z.Y. Wang, G.H. Yin, F.S. Zhang, *Adsorbing Performance of CMC Polymer for Heavy Metal Ions*, Journal of the Graduate School of the Chinese Academic of Sciences, 2009, 26(5), 627-632. (In Chinese)

Band / Volume 257
**Extension of the Reactor Dynamics Code MGT-3D
for Pebble-bed and Block-type High-Temperature-Reactors**
D. Shi (2015), x, 162 pp
ISBN: 978-3-95806-045-6

Band / Volume 258
Failure Analysis of Thin Film Solar Modules using Lock-in Thermography
M. Siegloch (2015), XIII, 131 pp
ISBN: 978-3-95806-047-0

Band / Volume 259
**Relation between growth rate, material quality, and device grade condition
for intrinsic microcrystalline silicon:**
From layer investigation to the application to thin-film tandem solar cells
S. Michard (2015), vi, 184 pp
ISBN: 978-3-95806-048-7

Band / Volume 260
**Quantitative analysis of spatially resolved electroluminescence
of Cu(In,Ga)Se_2 and a-Si:H thin-film solar cells and modules**
T. Tran (2015), iii, 161 pp
ISBN: 978-3-95806-050-0

Band / Volume 261
**Influence of the surface composition and morphology
on the reflectivity of diagnostic mirrors in a fusion reactor**
M. Matveeva (2015), 158 pp
ISBN: 978-3-95806-051-7

Band / Volume 262
**Very High Cycle Fatigue Behavior of Riblet Structured
High Strength Aluminum Alloy Thin Sheets**
S. Stille (2015), XII, 123 pp
ISBN: 978-3-95806-054-8

Band / Volume 263
**The role of soil heterogeneity on field scale evapotranspiration:
3D integrative modelling and upscaling of root water uptake**
K. Huber (2015), xii, 128 pp
ISBN: 978-3-95806-057-9

Band / Volume 264
**Strontium-Diffusion in Cer-Gadolinium-Oxid
als Degradationsmechanismus der Festoxid-Brennstoffzelle**
T. Mandt (2015), iii, 160 pp
ISBN: 978-3-95806-058-6

Band / Volume 265
Cluster analysis of European surface ozone observations for evaluation of MACC reanalysis data
O. Lyapina (2015), 187 pp
ISBN: 978-3-95806-060-9

Band / Volume 266
Real-time quantification of oxygen isotope exchange between carbon dioxide and leaf/soil water in terrestrial ecosystems with laser-based spectroscopy
L. Gangi (2015), XX, 156 pp
ISBN: 978-3-95806-061-6

Band / Volume 267
Secondary Uranium Phases of Spent Nuclear Fuel – CoXnite, $USiO_4$, and Studtite, UO_44H_2O – Synthesis, Characterization, and Investigations Regarding Phase Stability
S. Labs (2015), 153, xlii pp
ISBN: 978-3-95806-063-0

Band / Volume 268
Chemische, verfahrenstechnische und ökonomische Bewertung von Kohlendioxid als Rohstoff in der chemischen Industrie
A. Otto (2015), viii, 272 pp
ISBN: 978-3-95806-064-7

Band / Volume 269
In Vorbereitung

Band / Volume 270
Investigation of light propagation in thin-film silicon solar cells by dual-probe scanning near-field optical microscopy
S. Lehnen (2015),120 pp
ISBN: 978-3-95806-066-1

Band / Volume 271
Characterization of soil water content variability at the catchment scale using sensor network and stochastic modelling
W. Qu (2015), XVI, 123 pp
ISBN: 978-3-95806-067-8

Energie & Umwelt
Energy & Environment
271

Characterization of soil water content variability at the catchment scale using sensor network and stochastic modelling

Wei Qu

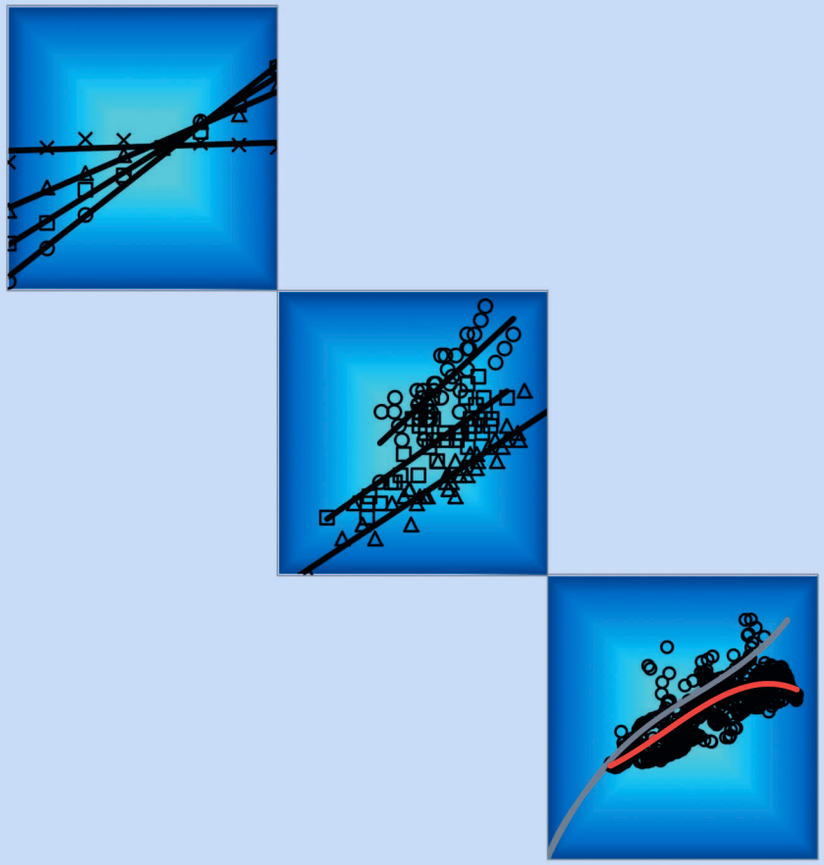

Energie & Umwelt / Energy & Environment
Band / Volume 271
ISBN 978-3-95806-067-8

JÜLICH FORSCHUNGSZENTRUM

Characterization of soil water content variability
Wei Qu

Member of the Helmholtz Association
JÜLICH FORSCHUNGSZENTRUM

Energie & Umwelt / Energy & Environment
Band / Volume 271
ISBN 978-3-95806-067-8

JÜLICH FORSCHUNGSZENTRUM